Fall 2015

Numerical and field data analysis of drill stem vibration

Mohammed Fayez Al Dushaishi

NUMERICAL AND FIELD DATA ANALYSIS OF DRILL STEM VIBRATION

by

MOHAMMED FAYEZ AL DUSHAISHI

A DISSERTATION

Presented to the Faculty of the Graduate School of the

MISSOURI UNIVERSITY OF SCIENCE AND TECHNOLOGY

In Partial Fulfillment of the Requirements for the Degree

DOCTOR OF PHILOSOPHY

in

PETROLEUM ENGINEERING

2015

Approved

Runar Nygaard, Advisor
Baojun Bai
Shari Dunn-Norman
Mingzhen Wei
Daniel S. Stutts

ABSTRACT

Drill stem vibration is a major cause of premature failure of drill stem components and drilling inefficiency. In severe cases, drill stem vibration may lead to wellbore instability that could lead to increased operational cost. Drill stem vibrations are affected by design decisions and the drilling environment. Examples are; bottom hole assembly configurations, selection of operational parameters, and frequent changes in lithology. Vibration modeling, analysis of vibration data, and specialized vibration reduction tools are methods in use to prevent and mitigate severe vibrations.

A drill stem vibration model was created using nonlinear strain formulation which couples the axial, lateral and torsional vibration of the entire drill stem. The model includes the effect of geometric stiffening arising from the applied axial load, two new developed vibration reduction tools used to reduce drill stem vibrations and fluid flow inside and outside the drill stem taking into account two different fluid rheological models. The obtained equation of motion was assembled using the finite element analysis which was solved numerically in Matlab®.

The sensitivity analysis using Euler-Bernoulli and Timoshenko models, showed that the Euler-Bernoulli assumption is satisfactory when modeling drill stem vibrations at typical drilling conditions. Analyzing three adjacent wells in the North Sea with different bottom hole assembly and recorded vibration data, revealed that including drill stem vibration reduction tools reduces drill stem vibration and decreases stick-slip tendency. Including drilling fluid circulation, by imposing dynamic pressures on the inside and outside of the drill stem, affect lateral natural frequencies. High flow rate and wrong selection of total flow area at the drill bit could lead to vibrations.

ACKNOWLEDGMENTS

First, I would like to thank God for his blessings.

Second, I would also like to express my gratitude to my committee members for providing me with the opportunity to present this study.

Dr. Runar Nygaard, my advisor, made it possible for me to work on multiple areas of drilling engineering while focusing in drilling optimization. Dr. Runar Nygaard encouraged me to network with scientific and industrial communities by attending conferences and student competitions, publish papers and participate in industrial projects. I am indebted to Dr. Nygaard for being my mentor and my friend; he taught me so much scientifically, professionally and personally in the last five years.

I would like to personally thank my committee members, Dr. Baojun Bai, Dr. Shari Dunn-Norman, Dr. Mingzhen Wei who played a virtual role in teaching me petroleum engineering and Dr. Daniel Stutts who had a significant role in teaching me the fundamental of mechanical vibrations. I would like to acknowledge further Dr. Stutts for the extra help, support and troubleshooting with the mathematical formulations and explanations. I would like to extend my thanks to Mr. Espen Hoel, Mr. Svein Hellvik, Mr. Mats Andersen, and Dr. Arild Saasen for their technical discussions and providing data.

I would to extend my thanks to Dr. Nygaard's research group, especially Mortadha Alsaba and Reza Rahimi for their help and valuable technical discussions. I would like to acknowledge individuals whom are dear to me, Ms. White, Dr. Aladasani, and Dr. Hilgedick.

Finally, I would like to show my appreciations and thanks to my parents, Fayez and Najah, and my sisters for their support and encouragements.

TABLE OF CONTENTS

LIST OF ILLUSTRATIONS

LIST OF TABLES

NOMENCLATURE

Symbol	Description
${}_{i}T_{j}$	Transformation Matrix
$[\ ]^{T}$	Transpose of a Matrix/Vector
$\dot{}$	Derivative with Respect to Time
$'$	Spatial Derivative with Respect to x
I_{o}	Cross Sectional Polar Moment of Inertia
I_{t}	Cross Sectional Inertia Matrix
N_{i}	Shape Function Corresponding to i Degree of Freedom
Θ_{b}	Angle Due to Pure Bending
θ_{y}	Bending Angle in the y-Direction
θ_{z}	Bending Angle in the z-Direction
A_{i}	Inside Flow Area
A_{n}	Annulus Area
A_{o}	Annulus (Outside) Flow Area
C_{D}	Discharge Coefficient
C^{TS}	Added Damping Matrix of the Torsional Vibration Sub
C_{TVS}	Total Damping of the Torsional Vibration Sub and Drill Stem
C_{f}	Viscous Damping Coefficient
D_{o}	Outside Diameter of the Drill Stem
D_{w}	Wellbore Diameter
F_{A}	Lateral Hydrodynamic Force
F_{L}	Frictional Lateral Force due To External Flow
F_{N}	Frictional Normal Force due to Outside Flow
F_{R}	Rate of Change of Fluid Momentum
F_{en}	Normal Hydrodynamic Force due to External Flow
F_{et}	Tangential Hydrodynamic Force due to External Flow
F_{f0}	Frictional Viscous Force

F_{in}	Normal Force due to Outside Pressure
F_{px}	Axial Force due to Outside Pressure
F_{pz}	Lateral Force due to Outside Pressure
F_{v}	Unbalance Force Applied in the y Direction
F_{w}	Unbalance Force Applied in the z Direction
K_{f_e}	Stiffness Element Matrix on the Fluid
K_{G}	Geometric Stiffness Matrix
K^{TS}	Added Stiffness Matrix of the Torsional Vibration Sub
K_{TVS}	Total Stiffness of the Torsional Vibration Sub and Drill Stem
K_{e}	Stiffness Matrix
L_{dc}	Length of Drill Collar
L_{dp}	Length of Drill Pipe
M_{f_e}	Mass Element Matrix on the Fluid
P_{Dyn}	Dynamic Pressure
P_{i}	Pressure Inside the Drill Stem
P_{o}	Pressure in the Annulus (Outside)
P_{pump}	Pump Pressure
S_{N_L}	Nonlinear Strain Component
S_{o}	Total Area per Unit Length
S_{tw}	Total Wetted Surface Area
T_{min}	Minimum Period
U_{i}	Fluid Velocity Inside the Drill Stem
U_{o}	Fluid Velocity Outside (in the Annulus)
V_{f}	Fluid Velocity Vector
W_{g}	Work Done by Gravity
b_{s}	Experimental Constant
e_{t}	Unit Vector Tangential to the Drill Stem Motion
f_{f_e}	Fluid Axial Force Vector

f_{g_e}	Element Gravitational Force Vector
f_f	System Axial Fluid Force
f_g	Gravitational Force Vector
f_r	Reaction Force at the Bit
$k_{1,2,3}$	Lithological Constants
k_s	Shear Factor
l_e	Element Length
l_{stab}	Stabilizer Location Measured from the Drill Bit
m_f	Mass of the Fluid per Unit Length
q_e	Nodal Displacement Vector
r	Position Vector
u_s	Initial Deformation
u_x	Displacement in the Undeformed x Direction
u_y	Displacement in the Undeformed y Direction
u_z	Displacement in the Undeformed z Direction
v_{im}	Distance from Geometric Center off Mass in the y Direction
w_{im}	Distance from Geometric Center off Mass in the z Direction
α_D	Mass Damping Factor
β_D	Stiffness Damping Factor
γ_m	Geometric Mean Shear Rate
θ_{ii}	Viscometer Readings at Different Rotational Speed
μ_p	Plastic Viscosity
ρ_f	Fluid Density
σ_{ij}	Stress Component
τ_0	Yield Point
τ_m	Shear Stress Corresponding to Geometric Mean Shear Rate
τ_w	Tangential Force Vector
ω_{min}	Minimum Natural Frequency

ϵ_{ij}	Strain Component
A	Cross Sectional Area
I	Cross Sectional Moment of Inertia
S	Strain Energy
T	Kinetic Energy
V	Velocity Vector
W	Work Done by the Non-Conservative Force
δ	Variation
$\Delta t_{critical}$	Critical Stable Time Step
$\Delta RPM_{Downhole}$	Difference in Rotation Speed Measured Downhole
Δt	Time Step
Θ	Torsional Analytical Displacement
ρ	Mass Density
Φ	Eigenvector
Ω	Rotational Velocity Vector
C	Damping Matrix
D	Stress Tensor
E	Young's Modulus
$F(t)$	Time Dependent Force
G	Gyroscopic Matrices
G	Shear Modulus
ID_{dc}	Inside Diameter of the Drill Collar
ID_{dp}	Inside Diameter of the Drill Pipe
M	Mass Matrix
M	Bending Moment
OD_{dc}	Outside Diameter of the Drill Collar
OD_{dp}	Outside Diameter of the Drill Pipe
OD	Largest Outside Diameter of the Drill Stem
Q	Transverse Shear Stress

RMS	Root Mean Square
$\mathrm{RPM_{Surface}}$	Measured Surface Rotational Speed
S	Rock Strength
T	Longitudinal Tension
a	Bit Constant
e	Gap between the Drill Stem and Wellbore Wall
$\mathrm{f\ hyd}$	Hydraulic Parameter
g	Gravitational Acceleration
k	Consistency Index
m	Mass of the Drill Stem
n	Flow Behavior Index
t	Time
u	Displacement in the x-Direction
v	Displacement in the y-Direction
w	Displacement in the z-Direction
$\Delta \mathrm{t_c}$	Compressive Travel Time
γ	Shear Angle
ζ	Dimensionless length
τ	Shear Stress
υ	Poisson's Ratio
χ	Confinement Parameter
ω	Eigenvalue
ϵ	Lagrangian Strain Tensor
$\mathrm{M_m}$	Bending Moment
$\mathrm{Q_f}$	Flow Rate
$\Delta \mathrm{P_b}$	Pressure Drop Across the Drill Bit
$\mathrm{A_t}$	Flow Area at the bit (Total Flow Area of the Nozzles)

1. INTRODUCTION

1.1. OVERVIEW

To drill a well into the subsurface, a drill bit is rotated to crush and shear the rock at the bottom of the well. The drill bit is connected to the surface with steel pipes known as the drill stem. At the surface, a drilling rig is used to raise and lower the drill stem. The rotation of the drill stem is provided by a rotary table connected to the drill stem or by an engine mounted in the mast (top drive). In some situations, a downhole motor powered by the circulating drilling fluid is added to the bottom of the drill stem to provide extra torque to the drill bit. To provide the necessary axial force for drilling, the drill stem consists of heavier weight pipes at the bottom of the drill stem, known as the bottom hole assembly (BHA), while regular drill pipe connects the bottom hole assembly to the surface (Figure 1.1.a).

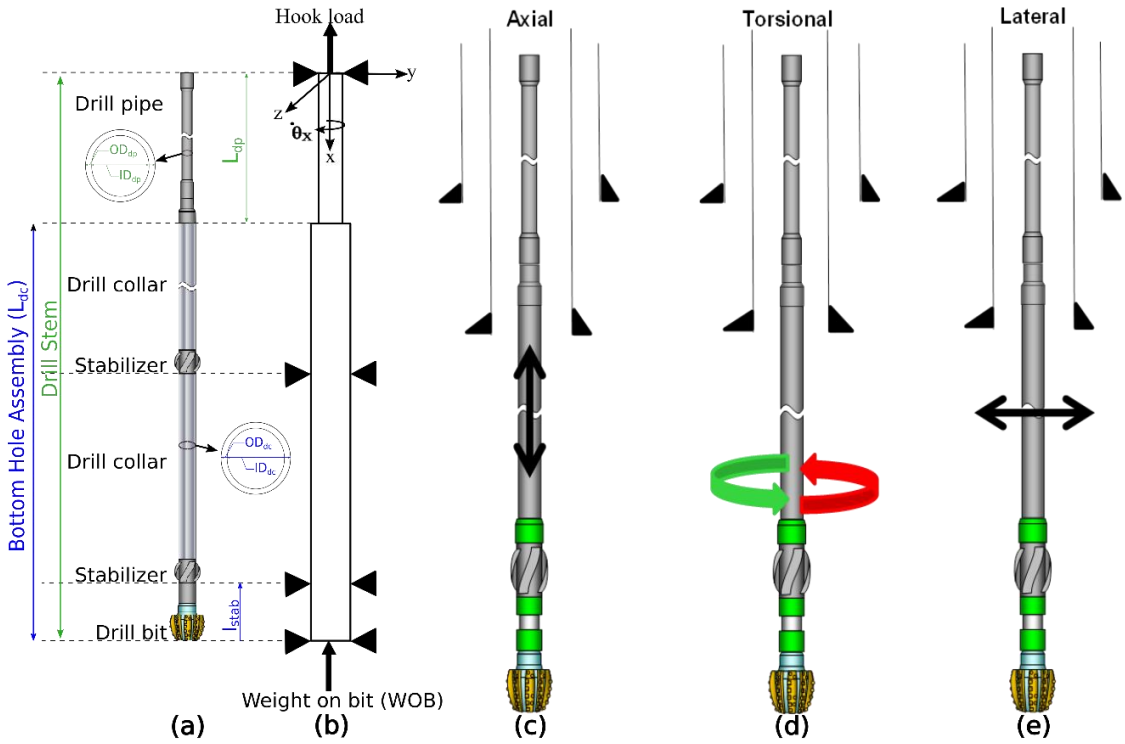

Figure 1.1. Schematic of a Drill and Vibration Modes: (a) Drill Stem Including Bottom Hole Assembly (BHA) and Drill Pipe (b) Model Configuration (c) Axial Vibration Mode (d) Torsional Vibration Mode (e) Lateral Vibration Mode

Due to the drill stem weight and fluid buoyancy forces the upper section of the drill stem is in tension, while the bottom section is in compression. To decrease lateral deflections of the bottom hole assembly stabilizers of larger diameter than the BHA are incorporated at multiple locations within the BHA.

When drilling, a fluid pump is pumping fluids into the drill stem which is circulated though the drill bit and back to the surface through the wellbore annulus (i.e. space between the drill stem and the wellbore wall) in order to lift rock fragments out of the wellbore, and to provide the necessary pressure to keep the wellbore stable while drilling.

The efficiency of the drilling process is evaluated based on the speed of drilling (i.e. rate of penetration in m/h) and the amount of time spent on drilling problems (i.e. non-productive time). Drill stem vibrations have been recognized as one of the main causes of drilling inefficiency. High magnitudes of drill stem vibrations increases dynamic stress per cycle leading to premature failure of the drill stem, interference with measurements while drilling, and damage to the drill bit (Heisig and Neubert, 2000; Cobern et al. 2007). During drilling, the drill stem (Figure 1.1.a) may encounter vibrations due to various reasons such as the cutting action of the drill bit, drill stem contact with the wellbore wall, and operating at critical speeds.

Drill stem vibrations can be categorized into axial (Figure 1.1.c), torsional (Figure 1.1.d), and lateral (Figure 1.1.e) vibration modes. Axial vibration is the up and down movement of the drill stem along its vertical axis. Torsional vibration is defined as the twisting movement of the drill stem components (drill pipe, BHA and bit) during rotation. Lateral vibration is the drill stem movement perpendicular to its neutral axis. While drilling, all three modes of vibration occur at the same time, however one mode will be more dominant (Dunayevsky et al. 1993). Destructive vibration can occur with each vibration mode. These destructive vibration are bit bounce associated with axial vibrations, stick-slip associated with torsional vibrations, and forward/backward whirl associated with lateral vibrations (Ahmadian et al. 2007). Bit bounce can be described as the drill bit repeatedly losing contact with the formation when drilling. Stick-slip occurs when the rotation of the drill string is slowed down or stopped at the bottom and released when the torque overcomes the friction resisting the drill stem rotation, it is the most severe torsional vibration phenomena. Whirl is a special case of lateral vibration defined as an off center

rotation of the drill stem, which could either follow or be opposite to the drill stem rotation (i.e. forward or backward whirl).

The drill stem is a complex structure due to the random nature of different dynamic forces caused by the changes in rock type and operational parameters. Drill stem vibrations are more severe in the bottom hole assembly, since the BHA is in compression (Piovan and Sampaio, 2006). The BHA excitation mechanism depends strongly on the type of drill bit (Spanos et al. 2002).

In an attempt to reduce damaging drilling vibrations, both memory (Schen et al. 2005) and real time (Arevalo and Fernandes, 2012) vibrations measurements are recorded to understand the dynamic behavior of the drill stem. Vibration measurement devices consisting of accelerometers can be installed at multiple locations within the bottom hole assembly to investigate the downhole dynamic environment of the drill stem. Another approach to reduce vibration is to include special tools designed to reduce vibrations in the BHA (McCarthy et al. 2011; Bouziane et al. 2012; Hutchinson et al. 2013; Gaines et al. 2013).

Modeling the drill stem dynamic behaviors are also utilized to avoid severe vibrations. Different drill stem vibration models have been introduced to predict resonance regions and determine contact points with the wellbore, consequently selecting optimum BHA components and operating parameters, such as weight on bit (WOB) and rotational speed (RPM) (Dunayevsky et al. 1993).

1.2. LITERATURE STUDY

In simplified form, the drill stem can be modeled as a stationary beam having a rigidity of (EI), and linear mass density ρ (Figure 1.2.a), where E is the Yong's Modulus and I is the moment of inertia. When a force acts on the beam (F) the amount of deflection $w\ x,t$ is related to the applied force and the beam stiffness; which is a function of Young's modulus, the area moment of inertia of the beam cross-section, length of the beam, and beam boundary conditions Fixed-Free boundary conditions shown in Figure 1.2.a.

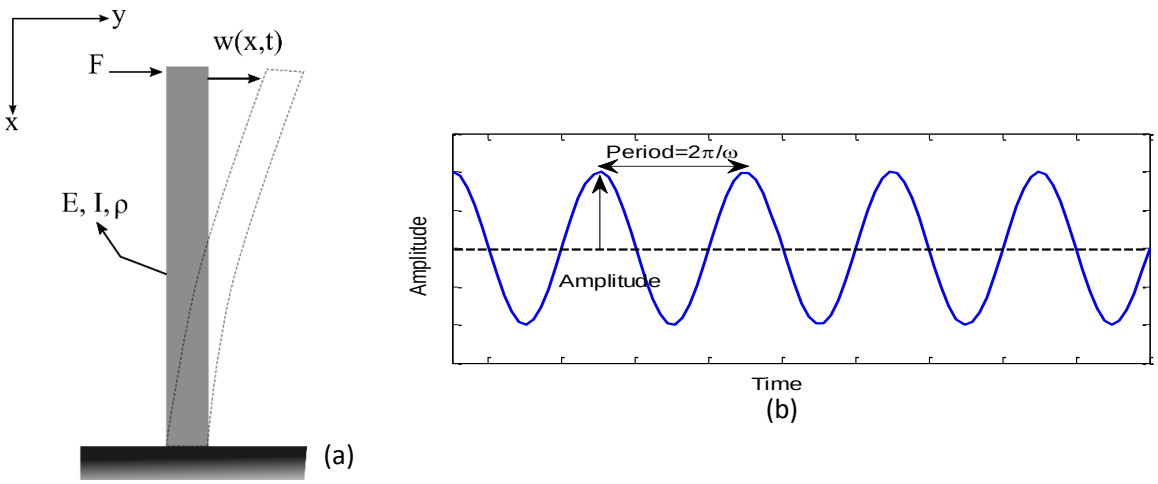

Figure 1.2. Fixed-Free Beam (a) Deflection due to Applied Force (b) Sinusoidal Wave with Constant Frequency

When the beam is under stress, the ratio of the transverse to axial strain (expansion ratio) is defined by the Poisson's ratio. The beam becomes stiffer under axial load due to the axial-transvers coupling, which causes large deformation. This effect is known as the geometric stiffening that is addressed by either simplified coupling of axial force to bending strain or by nonlinear stain displacement relationships. If a beam is under stress, the beam exhibits multiple forces such as the bending moment, rotary inertia, and shear forces. Euler-Bernoulli theories simplifies the beam deflection by assuming negligible rotary inertial effect when the beam is under stress. Rayleigh theory extends the Euler-Bernoulli assumption by including the effect of rotary inertia on the transverse beam deflection. The Timoshenko beam theory is a further development of Euler-Bernoulli and Rayleigh assumptions, where the bending moment, rotary inertia, and shear force have a contribution on the transverse deflection.

A beam is said to vibrate when the system exhibit an oscillating motion about a reference position. The amount of time a complete motion cycle takes place during the period of one second is known as the frequency ω (Figure 1.2.b). Frequency is measured in hertz (Hz), which is the reciprocal of the period, defined as the time of one cycle to complete itself (Figure 1.2.b). A body (beam) oscillating (vibrating) without applied external force, the body oscillation is known as the natural frequency.

In a static condition, the drilling fluid creates a hydrostatic pressure that acts on the drill stem, as the drilling fluid is assumed to be incompressible, the hydrostatic pressure becomes a function of the fluid density and the column depth. Drilling fluid can be categorized into three categories; oil base, water base, and gas/foam base. Additive materials are added to the base fluid to obtain desired density, viscosity, and other desired drilling fluid properties. Including multiple additives causes the drilling fluid to have a complex rheology. While drilling, the drilling fluid is circulated through the drill stem through the drilling bit and outside the drill stem (annulus) back to the surface using high pressure drilling fluid pumps. As the fluid is circulated around the wellbore, the fluid creates an additional dynamic pressure caused by friction (Mitchell and Miska, 2011). To determine the required pump pressure and thus the flow rate required, the determination of fluid flow frictional forces becomes an important task. The total pump pressure is obtained by describing the fluid motion through the drilling system, by assuming a fluid rheological model, in order to determine the frictional viscous forces (Mitchell and Miska, 2011). The viscous forces are characterized by the fluid viscosity is defined as the ratio between fluid shear stress and fluid shear rate (Figure 1.3).

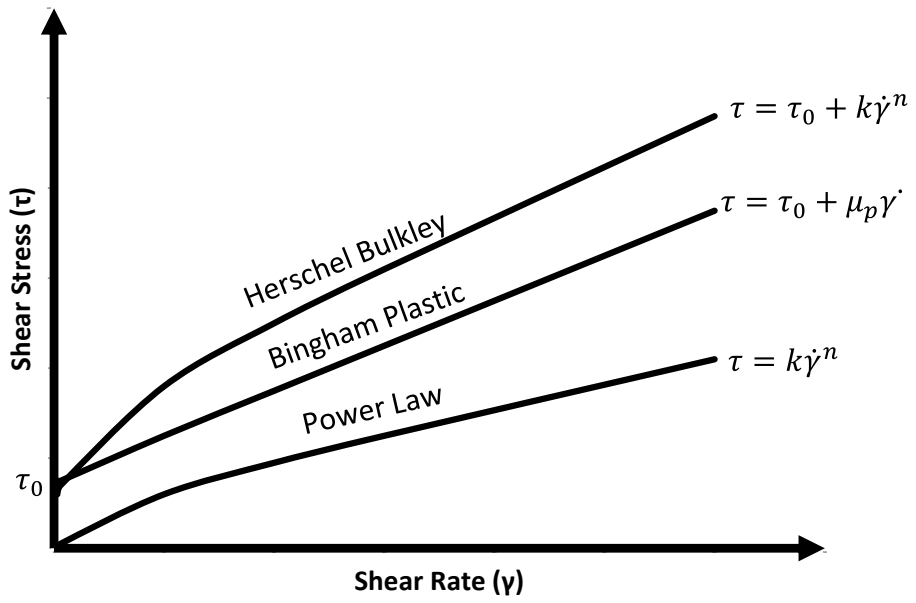

Figure 1.3. Shear Stress Versus Shear Rate for Different Fluid Rheological Models

When shear stress is directly proportional to the shear rate the fluid viscosity is constant, which defines a Newtonian fluid. Drilling fluid usually have a complex fluid rheology that does not have a direct relationship between shear stress and shear rate. To approximate the drilling fluid behavior a nonlinear relationship between fluid and shear stress and shear rate is used. Figure 1.3 shows the shear stress versus shear rate for different fluid rheological models.

For Bingham Plastic fluid model, the fluid will start flowing when the shear stress (τ) exceeds the yield point value (τ_0), and as the shear stress exceeds the yield point, the shear stress is a constant proportion to the shear rate, known as the plastic viscosity (μ_p). For the Power Law and Herschel Bulkley models, the shear rate and shear stress behavior are similar (Figure 1.3). The difference between the two models is the presence of a yield point in the Herschel Bulkley model. Different fluid rheological models such as Bingham plastic, Power Law and Herschel Bulkley models are used to represent the fluid flow behavior of the drilling fluid (Mitchell and Miska, 2011).

The drill stem is submerged in drilling fluid in the wellbore causing buoyant forces acting on it. The Buoyancy force is an upward force applied by the fluid that opposes the weight of the immersed drill stem. Under fluid motion, another force rises due to fluid flowing around or inside the drill stem (hydrodynamic forces), where the forces acts in opposite direction to the body movement similar to a drag force which depends significantly on the fluid rheological model.

Numerous theoretical studies have addressed the behavior of drill stem to avoid severe vibration levels (Burgess et al. 1987; Aslaksen et al. 2006). Two different modeling approaches, discrete and continuous models, of drill stem vibrations have been carried out to avoid harmful vibrations (Yigit and Christoforou, 1998; Heisig and Neubert, 2000; Leine et al. 2002; Ahmadian et al. 2007; Navarro-Lopez and Corts, 2007; Ghasemloonia et al. 2013). The two mechanical systems are shown in Figure 1.4, where E_i is the Young's Modules, I_i is the area moment of inertia, ρ_i is the linear mass density, and $w(x,t)$ is the lateral displacement. The discrete system (Figure 1.4.a) approach simplifies the continuous system (Figure 1.4.b) to an equivalent masses (M_{ieq}) and an equivalent stiffness (K_{ieq}) with the lateral displacement being $w(x,t) = w_1(x,t) + w_2(x,t)$.

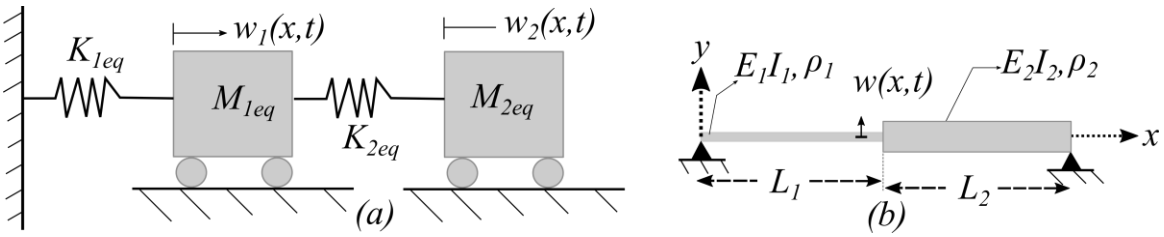

Figure 1.4. Equivalent Discrete System (a) of A Continuous Stepped Beam (b)

The equation of motion of a discreted model is describe by a set of ordinary differential equations (ODE's), which are simpler to deal with, while the continuous system equation of motion is described by partial differential equations (PDE's).

In situations where the differential equation of motion cannot be integrated in a closed form (i.e. analytical solution), numerical approach must be used. Several numerical integration methods are available to obtain the solution to the equation of motion; some of these methods are finite difference, Runge Kutta and Newmark integration method (Rao, 2001). Numerical integrations are not intended to satisfy the equation of motion at all the time but they will satisfy the equation of motion only at a discrete time interval.

1.2.1. Discrete System Approach. A discrete system approach (also known as lumped mass) is a simplified method where the target system (in this case the drill stem) is divided into a number of stages describing its motion by a number of ordinary differential equations. A coupled axial-lateral vibrations of the drill stem, including the contact forces with the wellbore wall, was addressed by Christoforou and Yigit (1997) using the Rayleigh beam theory. The Rayleigh beam theory is an extension of the Euler-Bernoulli beam theory, where the Rayleigh theory includes the effect of rotary inertia which is not considered in the Euler-Bernoulli theory. Their model took into account only the BHA part of the drill stem. The lower portion of the BHA was assumed to be under combined axial and lateral motion while the upper portion of the BHA was assumed to exhibit only axial motion. They showed that parametric resonance and whirling could occur within the range of operating drilling condition due to coupling effect. Yigit and Christoforou (1998) used a discrete model to investigate the effect on the drill stem stability when coupling torsional and bending modes. The coupled equation of motion between the two modes were obtained by applying Newton's law in polar coordinates and the bit rock interaction force was

assumed to be related to the bit motion (coupling term). Their study showed that instability may occur at critical speeds that does not consider to be critical when using an uncoupled linear model.

Navvaro-Lopez and Corts (2007) used a discrete vibration model to quantify torsional vibrations of the whole drill stem to study the stick-slip phenomena and the influence of the weight on bit on torsional vibration stability. The coupling between WOB and torsional vibration was introduced by the forces applied at the bottom of the drill stem (torque on bit) caused by the contact with the formation. However, axial and lateral motions were not considered in their model. They depict that not only applied forces have an effect on drill stem behavior, but also the system equilibrium state have changed the drill stem dynamic behavior.

A coupled stick-slip and whirl model was given in Leine et al. (2002) using a lumped mass model, including fluid forces as an external interaction force (i.e. hydrodynamic force). They concluded that the stick-slip motion is more likely to occur at lower angular velocities while backward whirl is more likely to occur at higher angular velocities. Melakhessou et al. (2003) modeled lateral and torsional vibrations considering only the BHA. For torsional vibrations, the model accounted for the rolling of the BHA with and without slip along the wellbore wall. The contact zones were determined using a discrete four-degree-of-freedom model. They obtained the equation of motion using the Lagrange mechanics and solved the equation of motion numerically using a Runge Kutta algorithm.

Later, Liao et al. (2011) extended the work of Melakhessou et al. (2003) by considering the impact of the induced friction between the drill stem and the wellbore wall with a discrete model formulation with a qualitative comparison with an experimental study. It was concluded that a higher friction coefficient destabilizes the drill stem motion. Stick-slip induced by drag bits was modeled using a discrete model that takes into account axial and torsional vibration modes by Richard et al. (2007). They concluded that the decrease in the rotational speed and applied torque at the bit while drilling was due to the drill stem response to the applied forces, rather than being due to the magnitude of the contact force of the drill bit and the formation. Despite the increase of applied rotational speed caused a decrease in the depth of cut and lower penetration rate.

1.2.2. Continuous System Approach. The continuous system approach is more complex, since the motion of the target system (drill stem in this case) is described by partial differential equations which are more difficult to solve compared to ordinary differential equations. In 1960, Bailey and Finnie introduced the first analytical uncoupled dynamic model to obtain the natural frequency of a drill stem. The model was based on an elastodynamic (elastodynamic refers to the study of elastic wave with time variation in elastic media) non-rotating beam model. Later, additional continuous models were developed to study different parameters effect on drill stem vibration (Chen and Geradin in 1994; Yigit and Christoforou, 1998; Ahmadian et al. 2007; Ghasemloonia et al. 2012). Continuous models can be categorized based on thet hree vibration modes; axial, torsional, and lateral modes. With the improvement of computational power, the coupling effect was addressed later (i.e. axial-lateral, axial-torsional, torsional-lateral).

The effect of torque and spatial varying axial loads were addressed by Ghasemloonia et al. (2012) using a continuous analytical model. The spatial axial force (axial force along the drill stem) was assumed to be in tension for the upper portion of the drill stem while the BHA is in compression. The torque was modeled as a bending moment force due to the bending curvature. Their study concluded that lateral natural frequencies are more sensitive to the change in WOB rather than torque. A coupled axial-torsional-lateral vibrations model was developed by Ahmadian et al. (2007) to investigate the parametric resonance (resonance due to fluctuation of WOB) of the drill stem. The continuous model coupled the axial and lateral vibration modes using nonlinear elastic deflections, while the discrete torsional mode was coupled through the applied torque and rotary speed. Their model showed that parametric resonance could occur occasionally within the safe operating condition of the drill stem due to coupling effects.

Ghasemloonia et al. (2013) took a different approach to analyze vibration by coupling axial and lateral vibrations in the BHA to evaluate if vibrations can improve the rock removal by the bit, and hence improve rate of penetration. The use of the Euler-Bernoulli beam theory was adopted assuming a compressive spatial axial force acting throughout the BHA. It was observed from the study that lateral vibrations are more severe in the upper portion of the BHA, while the most severe axial vibrations were located at the bottom of the BHA. The model was later modified to include the effect of different axial

shock sub designs (Ghasemloonia et al. 2014). The effect of axial load on lateral vibrations using a multiple degrees of freedom Euler-Bernoulli beam theory model was analyzed for the BHA portion of the drill stem only (Payne, 1992). The influence of drilling fluid forces on the drill stem was included as an added mass. The effect of stress stiffening due to the axial forces was included as a constant applied axial force for the entire BHA.

The influence of the axial force and rotary inertia on the BHA lateral vibrations were investigated using Timoshenko beam theory by Chen and Geradin in 1994. The gyroscopic effect was concluded to be negligible due to the low rotation speed. However, the conclusion was not supported by a sensitivity analysis or comparison with data. The effect of pre-stress configuration of a rotating drill stem was investigated by comparing an uncoupled linear and nonlinear-coupled Euler beam theory (Trindade et al. 2005). Fluid forces were not accounted for in their model, while a spatial axial force was applied so the BHA is in compression and the drill pipe is under tension. A relatively large difference in vibration amplitude was noticed when comparing the uncoupled linear with the nonlinear formulation due to the geometric nonlinearity. Ritto et al. (2009) followed the same approach as Trindade et al. (2005) in obtaining the geometric nonlinear stiffness from the axial loading using Timoshenko beam theory, and including drilling fluid forces. Their study showed that the presence of fluid forces changed the dynamic response and amplitude of lateral vibrations by comparing the lateral mode shape and drill stem response of the cases with no fluid and the case with fluid.

1.2.3. Effect of Drilling Fluid. The fluid effect on drill stem vibration has been addressed in multiple studies (Jansen, 1991; Chen and Geradin, 1994; Ahmadian et al. 2007; Ritto et al. 2009; Ghasemloonia et al. 2014). One way of including the influence of drilling fluid is by including an added mass and dampening term to the drill stem equation of motion. The drilling fluid added mass is included by substituting the drill stem density with an effective density based on the fluid mass and a variable volume term defined as the ratio of the wellbore diameter to the drill stem outside diameter (Chen and Geradin, 1994; Yigit and Christoforou, 1998; Sahebkar et al. 2011). The variable volume term is a simplified approach to increase the fluid force acting on the drill stem by reducing or increasing the clearance between the drill stem and the wellbore wall (outside annular space) with a constant added mass term. The influence of fluid forces exerted in two

perpendicular planes (as used in rotor dynamics) was used to account for drilling fluids by Leine et al. (2002).

Paidoussis et al. (2008) included the effect of drilling fluid flowing downward inside the drill stem then flowing back in the annulus assuming constant flow velocity, linear varying pressure with depth, and zero pressure at the outlet surface (Figure 1.5). They concluded that the effect of the internal and annular flow is sensitive to the annular space between the drill stem and the wellbore. Jafari et al. (2012) used Paidoussis et al. (2008) fluid interaction with the drill stem formulation and concluded that the drilling fluid could destabilize the drill stem. Later, Ritto et al. (2009a) adopted Paidoussis et al. (2008) fluid formulation to investigate the fluid effect on drill stem dynamics, including its natural frequencies. They revealed that fluid flow has a small effect on lateral vibrations, while axial and torsional vibrations are not affected.

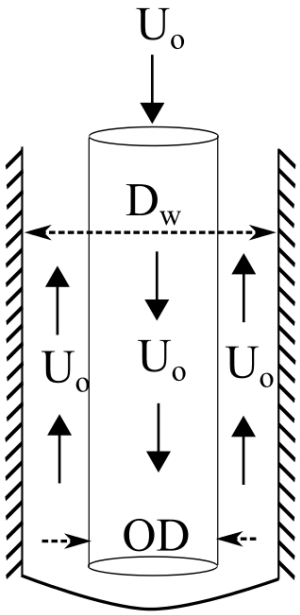

Figure 1.5. Fluid Path Model Developed by Paidoussis et al. (2007)

1.2.4. Vibration Dampening Tools. Lately, the industry has been addressing vibration by including tools in the drill stem to mitigate vibration. Multiple devices have

been developed and used in the BHA to reduce the effect of vibration on the BHA. One of the earliest vibration reduction tool was introduced in the 1960's to reduce axial vibrations known as shock subs (Warren and Oster, 1998).

The Anti-Stall technology (AST), shown in Figure 1.6, is one of the more recent vibration reduction tools used while drilling (Selnes et al. 2009). It consists of a mechanical hydraulic converter placed in the lower part of the drill stem (Figure 1.6).

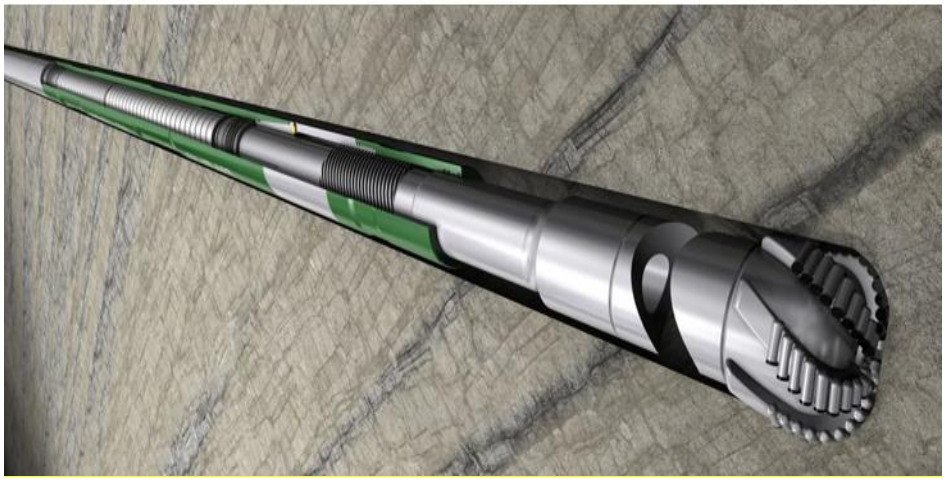

Figure 1.6. Anti-Stall Technology Vibration Reduction Tool used within the Bottom Hole Assembly (www.tomax.no, 2012)

The tool is placed on top of the BHA and balances the surface torque against the reactive torque from the bit (Figure 1.6). Any disturbance in torque, such as a spike caused by the cutter being stuck in the formation, will cause a contraction of the tool. This contraction instantaneously reduces the weight on the cutters and the contraction continues until the weight is reduced enough so that rotation can continue with the available torque. As rotation continues the internal spring in the tool will re-apply the initial weight. If the torque builds back up the tool will repeat the process.

The V-Stab is a dampening tool that minimizes both the magnitude and frequency of drilling vibrations by inducing forward synchronous whirl (McCarthy et al. 2011). V-Stab is an asymmetric tool that has two blades with diameter similar to the wellbore diameter (Figure 1.7).

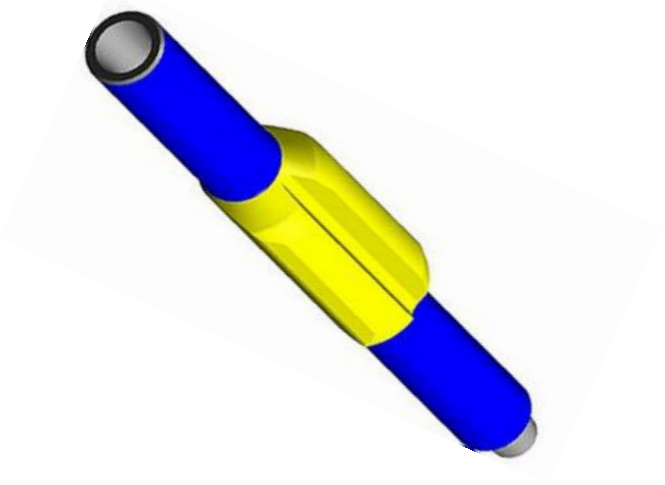

Figure 1.7. V-Stab Vibration Reduction Tool used within the Bottom Hole Assembly (www.nov.com, 2012)

1.2.5. Critical Review. The drill stem vibration models mentioned above have different assumptions, use different modeling approaches, and include various vibration modes. Some of these models considers axial, torsional or lateral vibration modes (Bailey and Finnie, 1960), and others used coupled models such as axial-lateral (Christoforou and Yigit, 1997), torsional-lateral (Melakhessou et al. 2003), axial-torsional (Richard et al. 2007) or fully coupled that includes axial-torsional-lateral (Ritto et al. 2009). Most of the coupled models are coupled using either excitation point of contact, forces acting on the drill bit, or nonlinear strain energy formulation.

The modeling techniques used to model the drill stem vibrations are divided into discrete and continuous models. The use of the discrete system enables modeling of complex system with nonlinear forces in a simplified approach. The use of the discrete system gives the advantages of dealing with simplified set of ordinary differential equations that provides fast computation of the system equation of motion. However, the use of discrete system hinders the ability to include major forcing factors such as the distributed axial load due to the weight of drill stem, which cause geometric softening of the BHA.

Different beam theories have been adopted as the basis of several drill stem vibration studies that uses continuous system approach. The most widely used theory is

Euler-Bernoulli beam theory (Payne, 1992; Ghasemloonia et al. 2012; Spanos et al. 2002). Another beam theory that was adopted is Rayleigh beam theory (Christoforou and Yigit, 1997). In a simple way, Rayleigh beam theory adds the effect of rotational inertia of the cross section, which it is neglected in Euler-Bernoulli beam theory. Timoshenko beam theory was also adopted in multiple studies (Chen and Geradin, 1994; Ritto et al. 2008). The use of Timoshenko beam theory increases the degrees of freedom by including the effect of both transverse shear strain and rotary inertia. Table 1.1 summarizes the differences between the three beam theories.

Table 1.1. Comparison of the Euler-Bernoulli, Timoshenko and Rayleigh Beam Theories

Beam Models	Bending moment	Lateral displacement	Shear deformation	Rotary inertia
Euler-Bernoulli	☑	☑	☒	☒
Timoshenko	☑	☑	☑	☑
Rayleigh	☑	☑	☒	☑

This raises the need to evaluate the difference between the widely used Euler-Bernoulli's and Timoshenko's beam theory under general drill stem forces applied while drilling.

Given that different parts of the drill stem is in compression and tension simultaneously, the effect of distributed axial force needs to be modeled. The distributed axial load can be modeled with two different methods. The first approach assumes the applied WOB to be constant for the whole BHA (Payne, 1992; Chen and Geradin, 1994; Heisig and Neubert, 2000). While the second approach use nonlinear coupling between the axial and lateral modes to simulate the quasi-static behavior of the drill stem for a given applied WOB (Trindade et al. 2005; Ritto et al. 2009). The advantages of using the second method, is that the neutral point, where no stress theoretically excited, can be obtained directly by performing a static analysis, and the exact deformation for each eleemtn can be obtained.

Two methods have been used to simulate the effect of drilling fluid on drill stem vibrations. The first method treats the fluid as an added mass that uses the effective density of the drill stem when submerged in drilling fluid (Payne, 1992; Chen and Geradin, 1994; Yigit and Christoforou, 1998; Sahebkar et al. 2011). The forces exerted by the fluid on the drill stem were studied by Leine et al. 2002, however, the influence of drilling fluid flowing downward inside the drill pipe and upward in the annulus while circulation was not considered. Drilling fluid forces acting inside and outside the drill stem were addressed in Paidoussis et al. (2008) and Ritto et al. (2009) models that included the fluid interaction assumes the fluid flows axially with constant flow velocity, and the fluid inside the drill stem is assumed to be inviscid and the fluid in the annulus is assumed to be viscous. The effect of the actual applied hydrostatic pressure acting on the drill stem was neglected in all previous models.

Incorporating vibration dampening tools in the drill stem BHA has been included in one study, where the effect of different axial shock sub designs was studied in a coupled analytical axial lateral model (Ghasemloonia et al. 2014). However, the modeling effect of torsional damping subs or imbalance vibration subs have not been addressed in any study.

1.3. RESEARCH OBJECTIVES

The main objective of this dissertation is to study the effect of drilling fluid and drill stem design, including vibration reduction tools, on changing the selection of critical drilling operating parameters. The main objective is accomplished by addressing the following tasks:

1. Construct a drill stem vibration model that takes into account the three vibration modes using an applicable approach (theory).
2. Model vibration reduction tools used in the bottom hole assembly to study their overall effect on drill stem vibration.
3. Incorporate the effect of drilling hydraulics and fluid rheology within the drill stem vibration model.
4. Analyze the impact of drill stem vibration on drilling performance.

1.4. ORGANIZATION OF THE DISSERTATION

The dissertation is divided into four chapters, where each chapter addresses the four tasks mentioned in the research objectives.

Chapter 2 addresses one of the main assumptions used to model drill stem vibrations (task 1). A parametric study of drill stem vibrations is introduced using Euler-Bernoulli and Timoshenko beam theories under different drilling conditions.

The second task investigates the effect of including vibration reduction tools in the drill stem. In Chapter 3, analysis of vibration data collected from three wells in the North Sea, that includes two vibration reduction tools, is addressed. Vibration reduction tools used in the field of study are modeled using the finite element formulation to investigate the dynamic behavior of each tool, while the field data are used for the modeling verification.

The third task investigates the effect of drilling hydraulics on the overall drill stem vibrations. The effect of the main components of drilling hydraulics such as pressure drop across the drill stem and fluid rheology on drill stem vibration is discussed in Chapter 4.

The final and fourth task is intended to relate drill stem vibration to drilling performance. Chapter 5 investigates the effect of drill stem vibration on drilling performance through including the drill stem vibrations with drilling efficiency model.

2. PARAMETRIC STUDY OF TWO COMMONLY USED BEAM THEORIES IN DRILL STEM VIBRATION MODELING

To investigate drill stem vibration behavior, continuous drill stem vibration models use either Euler-Bernoulli or Timoshenko beam theories. The difference between the two theories is established for slender beams; however as discussed in Chapter 1.2.5, studies on drill stem vibration use either the Euler-Bernoulli or the Timoshenko theory without addressing the difference. The objective of this chapter is to compare the Euler-Bernoulli and Timoshenko beam theories used for drill stem vibration modeling under different, yet realistic, drilling conditions.

2.1. INTRODUCTION

Continuous drill stem models mentioned previously (Ahmadian et al. 2007; Ghasemloonia et al. 2013; Ghasemloonia et al. 2012; Payne, 1992; Trindade et al. 2005) neglect the shear effect when adopting the Euler-Bernoulli beam theory (EBT) in their formulation. The effect of shear forces and rotary inertia is accounted for with the use of Timoshenko beam theory TBT (Chen and Geradin, 1994; Ritto et al. 2009). The change in vibration behavior using Timoshenko beam theory (TBT) rather than Euler-Bernoulli beam theory to model drill stem vibration was not addressed.

The Euler-Bernoulli's beam theory assumes that under stress, the plane cross section remains plane and normal to the longitudinal axis after deformation (Figure 2.1). For Timoshenko beam theory however, under stress the plane section remain plane but not normal to the longitudinal axis (Figure 2.1), which results in raising the transverse shear strain term accounting for shear deformation.

This chapter investigates the difference in using nonlinear coupled Euler-Bernoulli and Timoshenko beam theories applied to drill stem vibration modeling at typical different operating conditions. The finite element formulation is used to solve the coupled Euler-Bernoulli and Timoshenko models. Uncoupled analytical models of axial, torsional, and lateral vibrational modes of the drill stem are then used to verify the finite element formulation of both models. Both beam theories are analyzed when changing the

magnitude of the main forces applied to the drill stem and for different drill stem configurations.

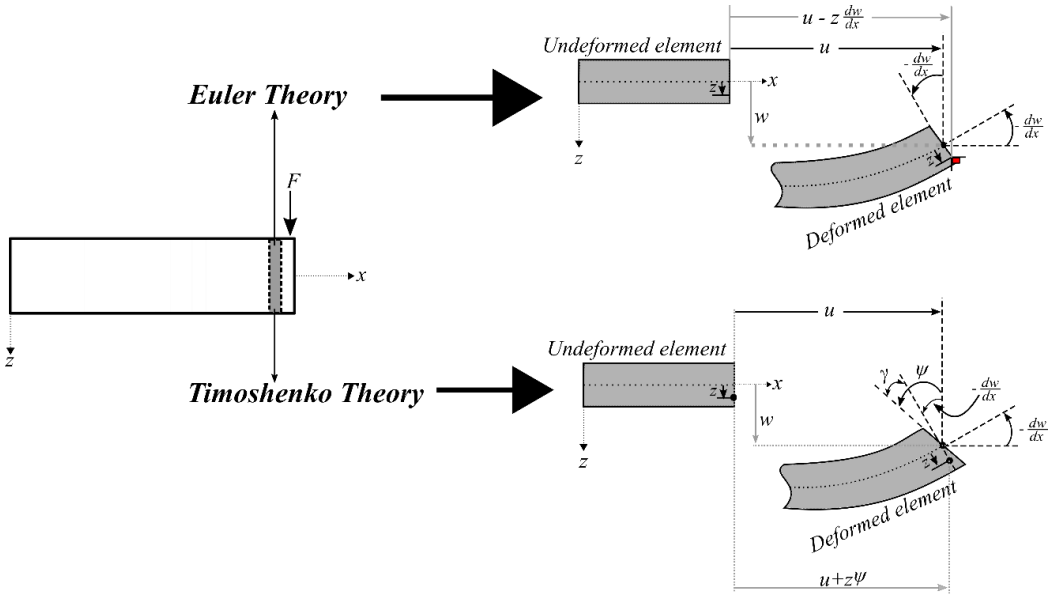

Figure 2.1. Mechanics of Euler-Bernoulli's and Timoshenko Beams Theories

2.2. DRILL STEM MODEL WITH FINITE ELEMENT FORMULATION

The drill stem model follows the formulation given in Trindade et al. (2005) and Ritto et al. (2009b), where the drill stem is modeled as a rotating cylinder. The equation of motion was obtained with the use of the extended Hamilton's principle (Equation 1) which states:

$$\delta \Pi = \int_{t_1}^{t_2} \delta S - \delta T - \delta W \; dt = 0 \tag{1}$$

Where δS is the variation of the system strain energy, δT is the variation of the kinetic energy, and δW is the variation of the work done by the non-conservatives forces.

2.2.1. Kinetic Energy. Considering a beam rotating around its neutral axis with an inertial Cartesian coordinates fixed to its undeformed position. The system translation velocity can be written as:

$$V = \begin{bmatrix} u \\ v \\ w \end{bmatrix} \tag{2}$$

Where u, v, and w are the velocities in x, y, and z directions respectively. The translation velocities and rotation around the x-axis are measured from the fixed inertial coordinates. The inertial frame is first rotated around its neutral axis (x-axis) by θ_x, the resulting frame is than rotated around the y-axis by θ_y, and finally the resulting frame is rotated around the z-axis by θ_z (Figure 2.2).

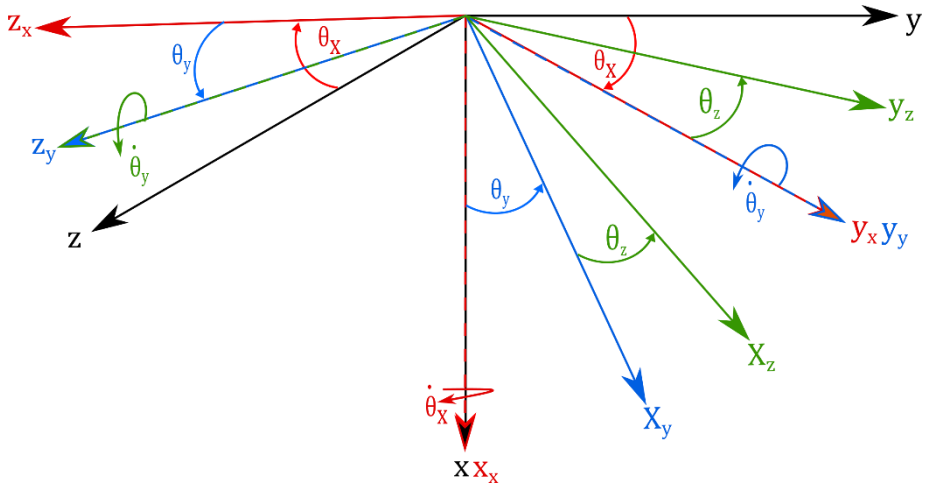

Figure 2.2. Rotation of Orthogonal Strain Axis Coordinate System

Hence, the angular velocity of the system can be obtained as:

$$\Omega = \begin{bmatrix} \theta_x \\ 0 \\ 0 \end{bmatrix} + [\ {}_OT_x] \begin{bmatrix} 0 \\ \theta_y \\ 0 \end{bmatrix} [\ {}_OT_x][\ {}_xT_y] \begin{bmatrix} 0 \\ 0 \\ \theta_z \end{bmatrix} \tag{3}$$

Where, $[\ {}_iT_j]$ is the transformation matrix referring back to the inertial frame. Thus, the kinetic energy is written in the following form:

$$T = \frac{1}{2}\int_0^L \rho[AV^T V + \Omega^T I_t \Omega]dx \tag{4}$$

Where, ρ is the mass density, and I_t is the cross sectional inertia defined as:

$$I_t = \begin{bmatrix} I_0 & 0 & 0 \\ 0 & I & 0 \\ 0 & 0 & I \end{bmatrix} \tag{5}$$

Where I is the moment of inertia, I_0 is the polar moment of inertia.

2.2.1.1 Euler-Bernoulli beam theory. The Euler-Bernoulli beam theory assumes the cross section stays rigid to its own plane resulting in a negligible transverse shear strain within the cross section. As a result, the bending angles θ_z and (θ_y) are defined as:

$$\theta_z = v' \qquad \theta_y = -w' \tag{6}$$

The superscript prime refers to the spatial derivative with respect to x. Substituting Equation 6 into the angular velocity expression in Equation 3 yields:

$$\Omega = \begin{bmatrix} \theta_x + v'w' \\ -w' cos\ \theta_x \ - v' sin\ \theta_x \\ -w' sin\ \theta_x \ + v' cos\ \theta_x \end{bmatrix} \tag{7}$$

With a few algebraic simplifications and assuming constant rotational speed θ_x and neglecting the higher order terms, the kinetic energy can be expressed as:

$$T = \frac{1}{2}\int_0^L \left[\rho A\ u^2 + v^2 + w^2\ + \rho I\left(v'^2 + w'^2\right) + \rho I_0 \theta_x^2 + 2I_0 \theta_x v' w'\right] dx \tag{8}$$

Where the superscript dot refers to derivative with respect to time. The kinetic energy was discretized using the finite element formulation with a linear shape function assigned for both the axial u displacement and the twisting angle θ_x and a cubic polynomial shape function for lateral displacements (v, w) (Piovan and Sampaio, 2006). The displacements can be written in discretized form in term of their shape functions as:

$$\begin{aligned} u_e\ \zeta,t\ &= N_u\ \zeta\ q_e\ t \qquad & v_e\ \zeta,t\ &= N_v\ \zeta\ q_e\ t \\ w_e\ \zeta,t\ &= N_w\ \zeta\ q_e\ t \qquad & \theta_{x_e}\ \zeta,t\ &= N_{\theta_x}\ \zeta\ q_e\ t \end{aligned} \tag{9}$$

Where N_i is the shape function corresponding to each degree of freedom (listed in Appendix A), ζ is the dimensionless length $\frac{x}{l_e}$, and q_e is the vector of nodal displacement of two node element (Figure 2.3) expressed as:

$$q_e = [u_1 \quad v_1 \quad v'_1 \quad w_1 \quad w'_1 \quad \theta_{x1} \quad u_2 \quad v_2 \quad v'_2 \quad w_2 \quad w'_2 \quad \theta_{x2}]^T \tag{10}$$

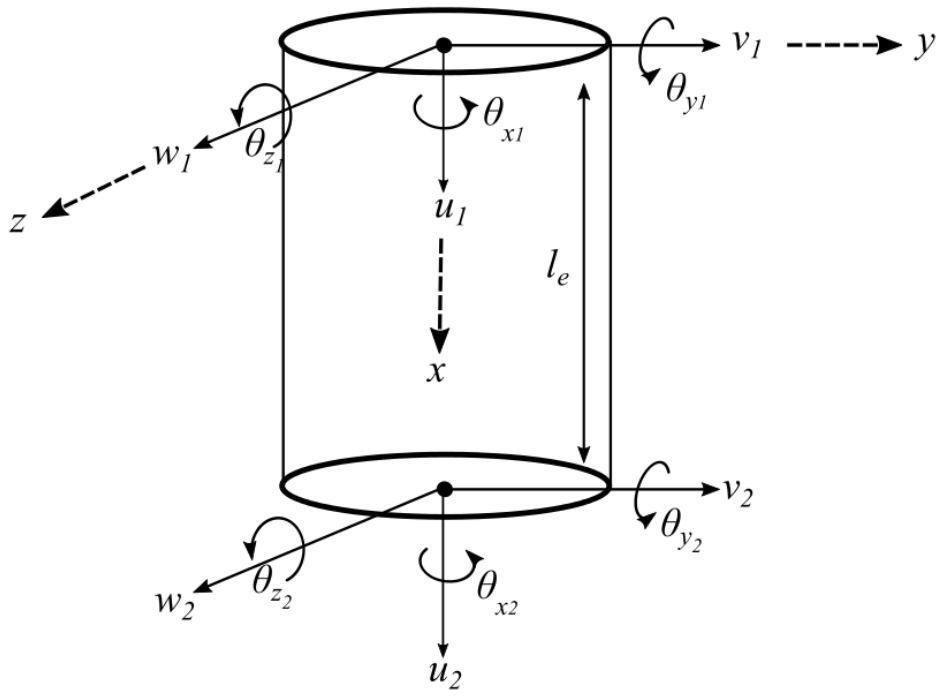

Figure 2.3. Degree of Freedom for One Drill Stem Element

Applying Hamilton's principle in Equation 1, and taking the first variation of the kinetic energy, the mass and gyroscopic matrices, assuming constant rotational velocity, can be expressed as:

$$M = \int_0^1 \Big(\rho A l_e [N_u^T N_u + N_v^T N_v + N_w^T N_w] + \frac{\rho I}{l_e} \left[{N'}_v^T {N'}_v + {N'}_w^T {N'}_w \right] \Big) d\zeta + \int_0^1 \left(\rho I_0 l_e \left[N_{\theta_x}^T N_{\theta_x} \right] \right) d\zeta \tag{11}$$

$$G = \int_0^1 \left(\frac{\rho I_0 \theta_x}{l_e} [{N'}_w^T {N'}_v - {N'}_v^T {N'}_w] \right) d\zeta \tag{12}$$

2.2.1.2 Timoshenko beam theory. The Timoshenko beam theory takes into account the shear force and the shear angle, thus, the drill stem angular velocity is given as:

$$\Omega = \begin{bmatrix} \theta_x + \theta_y \theta_z \\ \theta_y \cos\, \theta_x \; - \theta_z \sin\, \theta_x \\ \theta_y \sin\, \theta_x \; + \theta_z \cos\, \theta_x \end{bmatrix} \tag{13}$$

Following the same procedure as the Euler-Bernoulli model, assuming constant rotational velocity and neglecting the higher order terms, the kinetic energy takes the following form:

$$T = \frac{1}{2} \int_0^L \left[\rho A \; u^2 + v^2 + w^2 \; + \rho I \left(\theta_y^2 + \theta_z^2 \right) + \rho I_0 \theta_x^2 + 2 I_0 \theta_x \theta_y \theta_z \right] dx \tag{14}$$

Again, the kinetic energy was discretized using finite element formulation with a linear shape function assigned for both the axial (u) displacement and the twisting angle θ_x , cubic polynomial shape function for the lateral displacements (v, w) (Ritto et al. 2009). In addition for Timoshenko beam theory, quadratic polynomial was assigned to the

bending angles (θ_y, θ_z). The displacements and rotations are expressed in their discretized form, in term of their shape functions, as:

$$\begin{aligned} u_e\ \zeta,t\ &= N_u\ \zeta\ q_e\ t & v_e\ \zeta,t\ &= N_v\ \zeta\ q_e\ t \\ w_e\ \zeta,t\ &= N_w\ \zeta\ q_e\ t & \theta_{x_e}\ \zeta,t\ &= N_{\theta_x}\ \zeta\ q_e\ t \\ \theta_{y_e}\ \zeta,t\ &= N_{\theta_y}\ \zeta\ q_e\ t & \theta_{z_e}\ \zeta,t\ &= N_{\theta_z}\ \zeta\ q_e\ t \end{aligned} \tag{15}$$

Where N_i is the shape function corresponding to each degree of freedom (listed in Appendix A), ζ is the dimensionless length defined with $\frac{x}{l_e}$, and q_e is the vector of nodal displacement of two node element expressed as:

$$q_e = [u_1 \quad v_1 \quad \theta_{z1} \quad w_1 \quad \theta_{y1} \quad \theta_{x_1} \quad u_2 \quad v_2 \quad \theta_{z2} \quad w_2 \quad \theta_{y2} \quad \theta_{x_2}]^T \tag{16}$$

Taking the first variation of the kinetic energy, one could express the mass and gyroscopic matrices for a constant rotational speed as:

$$\begin{aligned} M = \int_0^1\ \rho A l_e [N_u^T N_u + N_v^T N_v + N_w^T N_w]\ d\zeta \\ + \int_0^1 \left(\rho I\ l_e \left[N_{\theta_y}^T N_{\theta_y} + N_{\theta_z}^T N_{\theta_z}\right] + \rho I_0 l_e \left[N_{\theta_x}^T N_{\theta_x}\right]\right) d\zeta \end{aligned} \tag{17}$$

$$G = \int_0^1 \left(\frac{\rho I_0 \theta_x}{l_e} \left[N_{\theta_y}^T N_{\theta_z} - N_{\theta_z}^T N_{\theta_y}\right]\right) d\zeta \tag{18}$$

2.2.2. Strain Energy. The strain energy is expressed in term of stress and strain as:

$$S = \frac{1}{2} \int_V \varepsilon^T D\ \varepsilon\ \ dV \tag{19}$$

Where, ε is the strain tensor, and D is the stress tensor. Assuming an isotropic material and the deformation gradient in the x-direction is much larger than the y and z directions, the stress and strain components simplifies to:

$$\sigma_{yy} = \sigma_{zz} = \sigma_{yz} = \varepsilon_{yy} = \varepsilon_{zz} = \varepsilon_{yz} \cong 0$$

As a result, the Lagrangian strain tensor simplifies to:

$$\varepsilon = \begin{bmatrix} \varepsilon_{xx} \\ 2\varepsilon_{xy} \\ 2\varepsilon_{xz} \end{bmatrix} \tag{20}$$

Where the axial strain and shear strain are defined in term of displacements as:

$$\begin{aligned} \varepsilon_{xx} &= \frac{\partial u_x}{\partial x} + \frac{1}{2}\left[\frac{\partial u_x}{\partial x}\frac{\partial u_x}{\partial x} + \frac{\partial u_y}{\partial x}\frac{\partial u_y}{\partial x} + \frac{\partial u_z}{\partial x}\frac{\partial u_z}{\partial x}\right] \\ \varepsilon_{xy} &= \frac{1}{2}\left[\frac{\partial u_x}{\partial y} + \frac{\partial u_y}{\partial x} + \frac{\partial u_x}{\partial x}\frac{\partial u_x}{\partial y} + \frac{\partial u_y}{\partial x}\frac{\partial u_y}{\partial y} + \frac{\partial u_z}{\partial x}\frac{\partial u_z}{\partial y}\right] \\ \varepsilon_{xz} &= \frac{1}{2}\left[\frac{\partial u_x}{\partial z} + \frac{\partial u_z}{\partial x} + \frac{\partial u_x}{\partial x}\frac{\partial u_x}{\partial z} + \frac{\partial u_y}{\partial x}\frac{\partial u_y}{\partial z} + \frac{\partial u_z}{\partial x}\frac{\partial u_z}{\partial z}\right] \end{aligned} \tag{21}$$

2.2.2.1 Euler-Bernoulli beam theory. Assumption the deformation gradient in the x-direction is much larger than the deformation in the y and z directions, the Euler-Bernoulli's stress tensor reduces to:

$$D = \begin{bmatrix} E & 0 & 0 \\ 0 & G & 0 \\ 0 & 0 & G \end{bmatrix} \tag{22}$$

Where, E and G are the Young's modulus and shear modulus respectively. Substituting Equation 20 and Equation 22 in the strain energy expression Equation 19 yields:

$$S = \frac{1}{2}\int_V \left[E\ \varepsilon_{xx}^2 + 4G(\varepsilon_{xy}^2 + \varepsilon_{xz}^2)\right]\ dV \tag{23}$$

The displacement in the undeformed configuration is defined as (Piovan and Sampaio, 2006):

$$u_x = u - y\ \ v' + z\ \ w' \qquad u_y = v - z\ \ \theta_x \qquad u_z = w + y\ \ \theta_x \tag{24}$$

Upon substituting Equation 21 and Equation 24 into Equation 23 and integrating over the area, the strain energy will consist of linear and nonlinear terms. The linear part of the strain energy (S_L) in term of displacement is:

$$S_L = \frac{1}{2}\int_0^L [EA\ u'^2 + EI\ v''^2 + w''^2\ \ + GI_0\ \theta_x'^2]dx \tag{25}$$

Considering up to the third order products, the simplified nonlinear term of the strain energy (S_{N_L}) is expressed in term of displacement as:

$$\begin{aligned} S_{N_L} &= \frac{1}{2}\int_0^L [EA\ u'^3 + u'v'^2 + u'w'^2\ \ + EI_0\theta_{x'}\ u'\theta_{x'} + v'w'' - w'v''\ ]dx \\ &+\frac{1}{2}\int_0^L [3EI\ \ u'\ \ \ w''^2 + v''^2\ \ + GI_0\ \ \theta_{x'}\ v''w' - w''v'\ ]dx \end{aligned} \tag{26}$$

Using the finite element to discretize the strain energy, the linear portion of the strain energy yields the standard Euler-Bernoulli stiffness matrix (K_e), while the nonlinear part, when only axial load initially exist, gives the geometric stiffness matrix (K_G):

$$\begin{aligned} K_e &= \int_0^1 \left[\frac{EA}{l_e}\ N'^T_u N'_u\ \ + \frac{EI}{l_e^3}\ N''^T_v N''_v + N''^T_w N''_w \right. \\ &\left. + \frac{GI_0}{l_e}\left(N'^T_{\theta_x} N'_{\theta_x}\right)\right] d\zeta \end{aligned} \tag{27}$$

$$\begin{aligned} K_G &= u' \int_0^1 \left[\frac{EA}{l_e}\left(\frac{3}{2}N'^T_u N'_u + N'^T_v N'_v + N'^T_w N'_w\right)\right] d\zeta \\ &+u' \int_0^1 \left[\frac{3EA}{l_e^3}\ N''^T_v N''_v + N''^T_w N''_w\ \ + \frac{EI_0}{l_e}\left(N'^T_{\theta_x} N'_{\theta_x}\right)\right] d\zeta \end{aligned} \tag{28}$$

Where, $u' = \frac{1}{l_e} N'_u \; q_e$ in Equation 28 depends on the initial deflection (initial static equilibrium configuration).

2.2.2.2 Timoshenko beam theory. Following the same assumption made for the Euler-Bernoulli formulation, the stress tensor for the Timoshenko beam theory is:

$$D = \begin{bmatrix} E & 0 & 0 \\ 0 & k_s G & 0 \\ 0 & 0 & k_s G \end{bmatrix} \tag{29}$$

Where, E, G, and k_s are the Young's modulus, shear modulus, and the shear factor respectively. Substituting Equation 20 and Equation 29 in the strain energy expression (Equation 19) yields:

$$S = \frac{1}{2} \int_V [E\varepsilon_{xx}^2 + 4Gk_s(\varepsilon_{xy}^2 + \varepsilon_{xz}^2)] dV \tag{30}$$

The displacement in the undreformed configuration is defined as (Ritto et al. 2009):

$$u_x = u - y\theta_z + z\theta_y \qquad u_y = v - z\theta_x \qquad u_z = w + y\theta_x \tag{31}$$

Upon substituting Equation 31 into Equation 21 then into Equation 30 and integrating over the area, the strain energy yields both linear and nonlinear terms. The linear part of the strain energy (S_L):

$$\begin{aligned} S_L = & \frac{1}{2} \int_0^L [EAu'^2 + EI(\theta'^2_z + \theta'^2_y) + k_s G I_0 \theta'^2_x] dx \\ & + \frac{1}{2} \int_0^L [k_s GA(v'^2 + w'^2 + \theta_z^2 + \theta_y^2 + 2\theta_y w' + 2\theta_z v')] \; dx \end{aligned} \tag{32}$$

Considering up to the third order products, the simplified nonlinear term of the strain energy (S_{N_L}) is:

$$
\begin{aligned}
S_{N_L} &= \frac{1}{2}\int_0^L \left[EA\ u'^3 + u'v'^2 + u'w'^2\ + 3EIu'(\theta'^2_z + \theta'^2_y)\right]dx \\
&+\frac{1}{2}\int_0^L \left[EI_0\theta'_x(u'\theta'_x - v'\theta'_y + w'\theta'_z) + 2k_sGA(\theta_z^2u' + \theta_y^2u' - \theta_z\theta_xw')\right]dx \\
&+\frac{1}{2}\int_0^L \left[2k_sGA(\theta_y\theta_xv' - \theta_zv'u' + \theta_yw'u') + k_sGI_0\theta'_x(\theta'_y\theta_z + \theta'_z\theta_y)\right]dx
\end{aligned}
\tag{33}
$$

Using the finite element method to discretize the strain energy, the linear portion of the strain energy yields the stiffness matrix K_e , while the nonlinear part yields geometric stiffness matrix K_G that couples the axial, lateral, and torsional modes:

$$
\begin{aligned}
K_e &= \int_0^1 \left[\frac{EA}{l_e}\ N'^T_u N'_u\ + \frac{EI}{l_e}\left(N'^T_{\theta_z}N'_{\theta_z} + N'^T_{\theta_y}N'_{\theta_y}\right)\right]d\zeta \\
&+\int_0^1 \left[\frac{k_sGI_0}{l_e}\left(N'^T_{\theta_x}N'_{\theta_x}\right) + \frac{k_sGA}{l_e}\ N'^T_v N'_v + N'^T_w N'_w\ \right]d\zeta \\
&+\int_0^1 \left[k_sGAl_e\left(N^T_{\theta_z}N_{\theta_z} + N^T_{\theta_y}N_{\theta_y}\right)\right]d\zeta \\
&+\int_0^1 \left[k_sGA\left(N'^T_wN_{\theta_y} + N^T_{\theta_y}N'_w + N^T_{\theta_z}N'_v + N'^T_vN_{\theta_z}\right)\right]\ d\zeta
\end{aligned}
\tag{34}
$$

$$
\begin{aligned}
K_{G_e} &= u'\int_0^1 \left[\frac{EA}{l_e}\ 3N'^T_u N'_u + N'^T_v N'_v + N'^T_w N'_w\ \right]d\zeta \\
&+u'\int_0^1 \left[k_sGA\left(N^T_{\theta_z}N'_v + N^T_{\theta_y}N'_w + N'^T_vN_{\theta_z} + N'^T_wN_{\theta_y}\right)\right]d\zeta \\
&+u'\int_0^1 \left[k_sGA\left(2l_eN^T_{\theta_z}N_{\theta_z} + 2l_e\ \ N^T_{\theta_y}N_{\theta_y}\right)\right]d\zeta \\
&+u'\int_0^1 \left[k_sGA\left(\frac{3EI}{l_e}\left(N'^T_{\theta_z}N'_{\theta_z} + N'^T_{\theta_y}N'_{\theta_y}\right) + \frac{EI_0}{l_e}N'^T_{\theta_x}N'_{\theta_x}\right)\right]d\zeta
\end{aligned}
\tag{35}
$$

2.2.3. Forces on the Drill Stem. The main forces applied to the drill stem considered in this chapter are the rotational speed applied by the rotary table on top, gravity force, and fluid force. The work done by the gravity force is written as:

$$W_g = \int_0^L [\rho g A u] \; dx \tag{36}$$

Taking the first variation of Equation 36 followed by discretizing the variation of the gravity force equation, the gravity force vector is obtained as:

$$f_{g_e} = \int_0^1 [\rho g A l_e N_u^T] d\zeta \tag{37}$$

The fluid interaction forces included in this chapter follows Ritto et al. (2009). The simplified fluid model assumes the fluid flow inside the drill stem to be inviscid, while the fluid outside the drill stem to be viscous and the pressure varies linearly with depth. The fluid flow is assumed to be linear with no axial rotation. The discretization of the fluid forces yields the added mass matrix (M_{f_e}), and fluid stiffness (K_{f_e}) expressed as:

$$M_{f_e} = \int_0^1 [(m_f + \chi \rho_f A_0) \; N_w^T N_w + N_v^T N_v \; l_e] d\zeta \tag{38}$$

$$\begin{aligned} K_{f_e} = & \int_0^1 \left[(-m_f U_i^2 - A_i P_i + A_o P_o - \chi \rho_f A_o U_o^2) \; N'^T_w N'_w + N'^T_v N'_v \; \frac{1}{l_e} \right] d\zeta \\ & + \int_0^1 \left[\left(-A_i \frac{\partial P_i}{\partial x} + A_o \frac{\partial P_o}{\partial x} \right) \left(N_{\theta_y}^T N_{\theta_y} + N_{\theta_z}^T N_{\theta_z} \right) l_e \right] d\zeta \end{aligned} \tag{39}$$

Where, m_f is the fluid mass per unit length, ρ_f is the fluid density per unit length, A_o is the outside flow area, A_i is the inside flow area, U_i and U_o are the fluid velocity inside and outside the drill stem respectively, χ is a confinement parameter that's always equal or less than 1 and it's defined as:

$$\chi = \frac{\left(\frac{D_w}{D_o}\right)^2 + 1}{\left(\frac{D_w}{D_o}\right)^2 - 1}$$

P_i And P_o are the pressures inside and outside the drill stem defined as:

$$P_i = \rho_f g x, \qquad P_o = \left(\rho_f g + \frac{F_{f0}}{A_o}\right) x \tag{40}$$

The frictional viscous force (F_{f0}) is defined in term of fluid density, viscous damping coefficient (C_f), outside velocity, and the flow diameter D_o as:

$$F_{f0} = \frac{1}{2} C_f \rho_f D_o U_o^2$$

The axial force caused by the fluid flow is written as:

$$f_{f_e} = \int_0^L \left[\left(m_f g - A_i\right) \frac{\partial P_i}{\partial x} - \frac{1}{2} C_f \rho_f D_o U_o^2\right) N_u^T l_e \Big] d\zeta \tag{41}$$

2.2.4. Equation of Motion. Applying the extended Hamilton's principle and assembling the element matrices, the equation of motion can be expressed as:

$$[M + M_f]x + [C + G]x + [K + K_G + K_F]x = f_g + f_f + f_r \tag{42}$$

Where, f_r is the reaction force at the bit, f_g is the system gravitational force, f_f is the system axial fluid force, and C is proportional damping matrix. The proportional damping matrix is defined as:

$$C = \alpha(M + M_f) + \beta(K + K_G + K_f) \tag{43}$$

To obtain the geometric stiffness matrix, the initial deformation is first solved for in static configuration. The time invariant forces in the equation of motion are f_g, f_f, and the static reaction force f_r. The drill stem is assumed to be initially at rest with fixed axial

and lateral motion on top and at the stabilizer locations, thus the initial deformation (u_s) is obtained as:

$$u_s = [K + K_f]^{-1}(f_g + f_f + f_r) \tag{44}$$

For the boundary conditions, the drill stem is assumed to be fixed in the axial and lateral motion on top (rotary table) and a constant axial rotational speed is imposed. On the bottom (bit), lateral and axial displacements are constrained. To account for added stabilizers, the lateral displacements are locked at each stabilizer location. To obtain the natural frequencies and mode shape, the generalized Eigenvalue problem is formulated as:

$$[K + K_f + K_g\ u_s\ ]\Phi = \omega^2[M + M_f]\Phi \tag{45}$$

Where, ω is the eigenvalue and Φ is the eigenvector. Computational details are found in Appendix F.

2.3. FINITE ELEMENT MODEL VERIFICATION

2.3.1. Presentation of Uncoupled Non-Stressed Analytical Models. Uncoupled analytical axial, torsional, and lateral models were used to verify the finite element models. Both the Euler-Bernoulli and Timoshenko models were used for the lateral model verification. The free axial natural frequencies were obtained by solving the equation of motion (Equation 46) obtained using Hamilton's principle (Appendix B):

$$\rho A \frac{\partial^2 u}{\partial t^2} = EA \frac{\partial^2 u}{\partial x^2} \tag{46}$$

Where, u is the axial displacement. Up on separating the spatial domain and assuming fixed boundary conditions at the top and bottom with enforcing continuity boundary conditions, at the interface between drill pipe and drill collar, the axial natural

frequencies are obtained. Solution to the equation of motion is located in Appendix F, where the equation of motion was solved in MapleSoft™.

For the uncoupled analytical torsional model, the free natural frequencies were obtained by solving the torsional equation of motion (Equation 47) obtained by Hamilton's principle (Appendix C):

$$\rho I_o \frac{\partial^2 \Theta}{\partial t^2} = G I_0 \frac{\partial^2 \Theta}{\partial x^2} \tag{47}$$

Where, Θ is the torsional displacement. The boundary conditions used to solve for the free vibrations natural frequencies were fixed on top and free on bottom with enforcing continuity boundary conditions at the drill pipe and drill collar interface, similar to the axial mode.

Using the Euler-Bernoulli theory, the uncoupled transverse equation of motion Equation 48 was obtained using Hamilton's principle as (Appendix D):

$$\frac{\partial^2}{\partial x^2}\left(EI\frac{\partial^2 w}{\partial x^2}\right) + \rho A \frac{\partial^2 w}{\partial t^2} = 0 \tag{48}$$

Where, w is the transverse (lateral) displacement. Fixed boundary conditions were assumed at both ends of the drill stem with enforcing continuity boundary conditions at the interface between drill pipe and drill collar. Lateral displacement was restricted at the stabilizer location, as another boundary condition.

The formulation presented by Majkut, (2009) was adopted to acquire the uncoupled free lateral frequencies of the Timoshenko model. The unforced equation of motion of Timoshenko beam theory is written as:

$$\begin{aligned} &-\frac{\partial}{\partial x}\left(k_s G A\ \gamma\ x,t\ \right) + \rho A \frac{\partial^2 y\ x,t}{\partial t^2} = 0 \\ &-\frac{\partial}{\partial x}\left(EI\frac{\partial \Theta_{\mathrm{b}}\ x,t}{\partial x}\right) + k_s G A\ \gamma\ x,t\ - \rho I \frac{\partial^2 \Theta_{\mathrm{b}}\ x,t}{\partial t^2} = 0 \end{aligned} \tag{49}$$

Where, γ is the shear angle, Θ_b is the angle due to pure bending, and y is the transverse lateral displacement. The equation of motion for the transverse vibration is presented in terms of a single equation as:

$$
\begin{aligned}
Y\ x\ &= -\frac{1}{b}\left[\frac{\partial^4 X}{\partial x^4} + \ a + c\ + \frac{\partial X}{\partial x}\right] \\
a &= \frac{\omega^2 \rho}{k_s G} \\
b &= \frac{\rho \omega^2}{E} + c \\
c &= \frac{G k_s A}{EI}
\end{aligned}
\tag{50}
$$

The same boundary conditions used for the Euler-Bernoulli model was also applied to the Timoshenko model.

2.3.2. Verification with Analytical Models. A simplified drill stem configuration consisting of 1600 m drill pipe, 200 m drill collar, and a stabilizer located at 1600 m was chosen to compare natural frequencies of Euler-Bernoulli and Timoshenko finite elements formulations. Table 2.1 gives a detailed specification of the simplified drill stem geometry and materials.

Table 2.1. Drill Stem Configuration used for Analytical Comparison

Component	Length (m)	OD (m)	ID (m)
Drill pipe	1600	0.127	0.095
Drill collar	200	0.2286	0.0762
Stabilizer Location	1600		
	Properties		
ρ	7850	kg/m^3	
E	2×10^{11}	Pa	
k_s	6/7	(-)	
ν	0.29	(-)	

For the finite element models, the drill pipe was discretized to 83 elements, with the element length being 20 m, while the drill collar was discretized to 108 elements, with the element length being 2 m. Figure 2.4 shows the unforced natural frequencies (i.e., harmonics) obtained from the finite element models, using Euler-Bernoulli and Timoshenko models, compared with the analytical free natural frequencies.

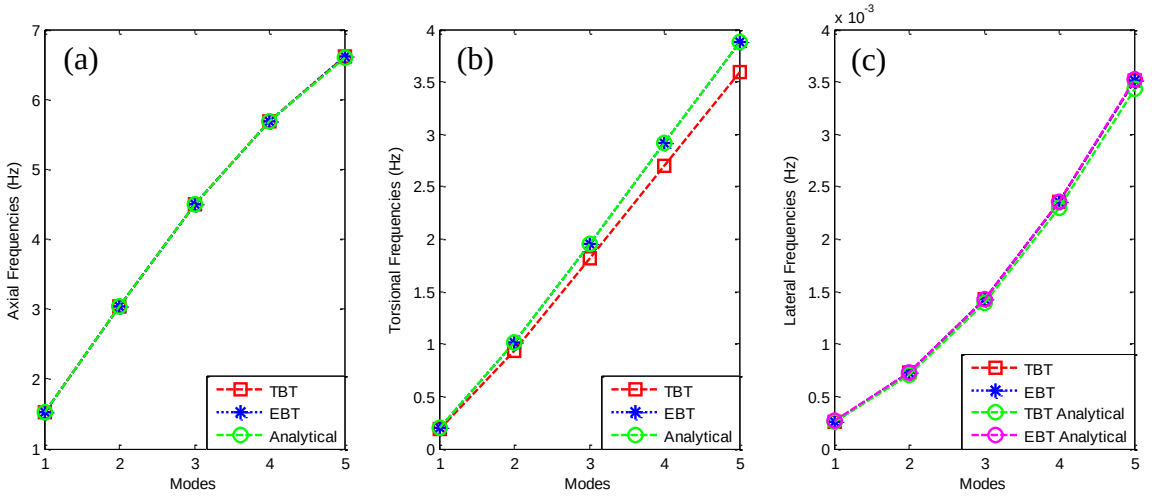

Figure 2.4. Free Vibration Frequencies Obtained From Finite Element and Analytical Models (a) Axial (b) Torsional (c) Lateral

Unforced axial natural frequencies obtained with the finite element and analytical models are in good agreement (Figure 2.4). Torsional natural frequencies obtained with the Euler-Bernoulli model matches the analytical model, while a slight deviation is noticed with the frequencies obtained using the Timoshenko model. The Euler-Bernoulli frequencies are higher (Figure 2.4.b). For lateral natural frequencies, the finite element and the analytical models are well correlated (Figure 2.4.c).

2.3.3. Verification With Axial Load. Payne, (1992) used finite element formulation to model the drill stem BHA lateral vibration under axial load using the Euler-Bernoulli beam theory. The effect of axial load on lateral vibration was considered through a coupled simplified model in the Payne, (1992) formulation. Both Euler-Bernoulli and Timoshenko models were used to calculate the BHA's lateral natural frequencies to verify

the models with axial loads. The BHA configuration used by Payne, (1992) is listed in Table 2.2.

Table 2.2. BHA Configuration used by Payne (1992)

Component	Length (m)	OD (m)	ID (m)
Heavy weight Drill pipe	34.3	0.171	0.071
Drill collar	16.9	0.203	0.071
Stabilizer 1 Location	3.8	Pinned Boundary	
Stabilizer 2 Location	23.6	Pinned Boundary	
Stabilizer 3 Location	34.3	Pinned Boundary	
Stabilizer 4 Location	44.9	Pinned Boundary	
Stabilizer 5 Location	49.5	Pinned Boundary	
Properties			
ρ	7833	kg/m^3	
E	2×10^{11}	pa	
k_s	6/7	(-)	
ν	0.29	(-)	
Axial load (WOB)	100	KN	

The boundary conditions for lateral direction were fixed boundary condition at surface and free boundary condition at the bit (Payne, 1992). To account of the stabilizers, the lateral displacement was restricted at the stabilizer location. The first three lateral frequencies are presented in Table 2.3.

The first lateral natural frequency mode given in Table 2.3 shows that the Euler and Timoshenko based FEA results are comparable and 3% lower than reported by Payne, (1992). For the 2nd and 3rd lateral natural frequencies all three results are within 1.4 %.

Figure 2.5 shows the normalized first three mode shapes along the drill stem length. The resulting first three modes obtained from both Euler-Bernoulli and Timoshenko models are an exact match.

Table 2.3. Calculated Lateral Natural Frequencies using Euler-Bernoulli, Timoshenko Models and FEA Results Reported by Payne, (1992)

Mode No.	(Payne, 1992) (Hz)	Euler (Hz)	Timoshenko (Hz)
1	1.700	1.649	1.648
2	4.200	4.203	4.200
3	5.200	5.273	5.268

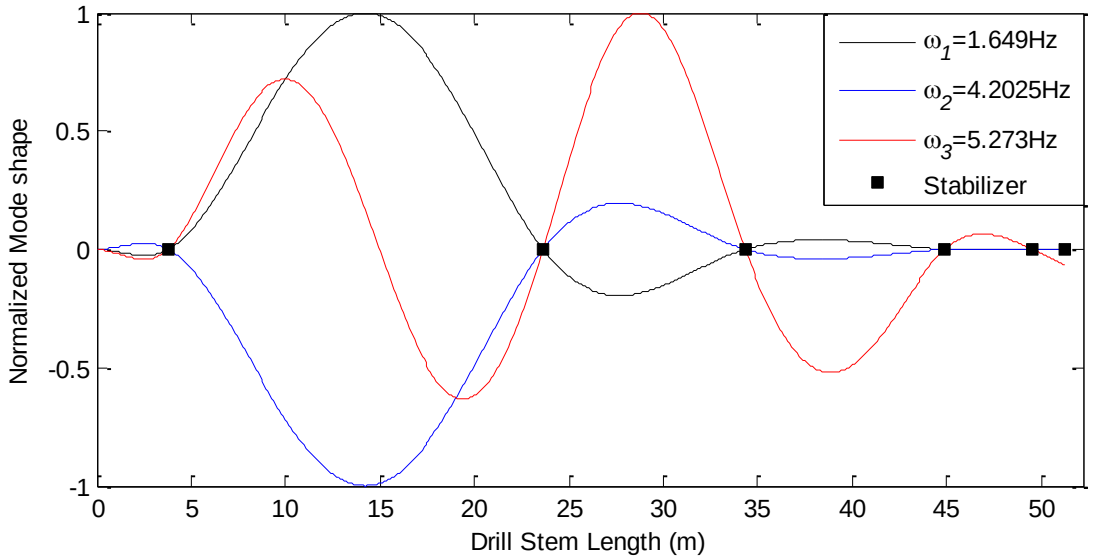

Figure 2.5. Normalized First Three Lateral Mode Shapes

2.4. PARAMETRIC STUDY OF EULER AND TIMOSHENKO MODELS

A drill stem with a total length of 1800 m was chosen to perform sensitivity analysis on the Euler-Bernoulli and Timoshenko models to analyze lateral, torsional, and axial

natural frequencies. The drill stem consist of 1600 m drill pipe, 200 m drill collar, and two stabilizers. A detailed specification of the drill stem is listed in Table 2.4.

Table 2.4. Drill Stem Configuration used for the Parametric Study

Component	Length (m)	OD (m)	ID (m)
Drill pipe	1600	0.095	0.127
Drill pipe element length	20	-	-
Drill collar	200	0.076	0.229
Drill collar element length	2	-	-
Borehole	1800	0.3	-
Stabilizer 1 Location	1780	Pinned Boundary	
Stabilizer 2 Location	1798	Pinned Boundary	
Properties			
ρ	7833	kg/m^3	
ρ_f	1200	kg/m^3	
C_f	0.0125	(-)	
U_i	1.5	m/s	
E	2×10^{11}	Pa	
k_s	6/7	(-)	
ν	0.29	(-)	
g	9.81	m/s^2	
Ω_x	10	rad/s	
Axial load (WOB)	100	KN	

In this analysis, the first ten modes reported for both the Euler-Bernoulli and Timoshenko Finite element models. Figure 2.6 shows the first ten modes (axial, torsional, and lateral vibration modes) obtained for the 1800 m base case drill stem geometry (Table 2.4).

The same trend obtained from the analytical model (Table 2.1) can also be noticed in Figure 2.6 for the axial (Figure 2.6.a) and lateral (Figure 2.6.c) modes. The only noticeable difference between the two models is the torsional natural frequencies (Figure 2.6.b).

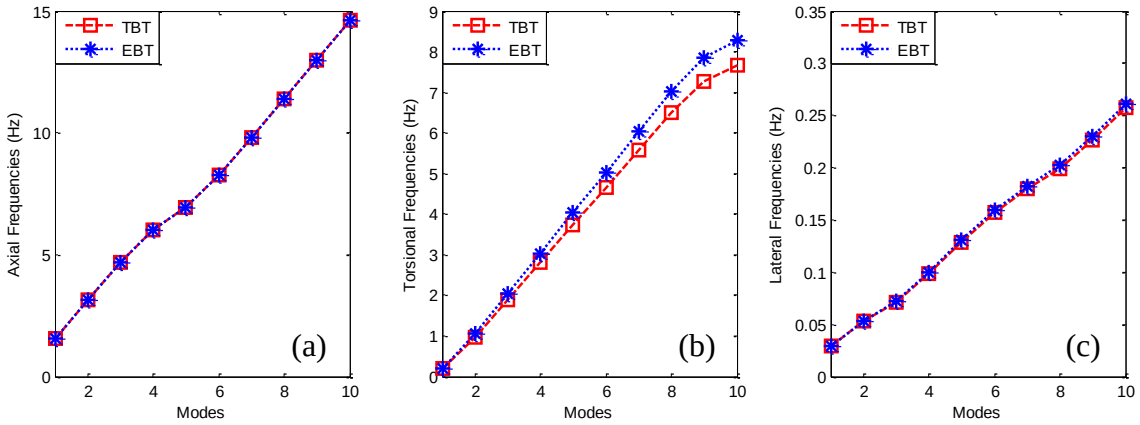

Figure 2.6. First Ten Natural Frequencies Obtained using Euler-Bernoulli (EBT) and Timoshenko (TBT) Finite Element Models (a) Axial (b) Torsional (c) Lateral

Using both models, the first and 10th natural frequencies were calculated for the same drill stem configuration under varying axial loads. Figure 2.7 shows the effect of axial load on the first and 10th axial, torsional, and lateral natural frequencies, where the left axis shows the first natural frequencies scale and the right axis shows the 10th natural frequency scale in Hertz.

As the applied axial load increases, the drill stem natural frequency decrease for both models (Figure 2.7). For the axial natural frequencies, the first and 10th modes obtained, from both models, are equal when varying the axial load. The difference in torsional natural frequencies did not change with changing the axial loads for either the first or 10th natural frequencies.

Analyzing the lateral frequencies as weight on bit increases, the percentage difference between Euler-Bernoulli and Timoshenko models is increased by only 1%. Increasing the axial load up to 400 KN caused a decrease in lateral natural frequency by 23.5% and 24% at the first mode and 24.25% and 25.2% at the 10th mode for Euler-Bernoulli and Timoshenko models respectively. On the other hand, axial and torsional natural frequencies were not affected (less than 0.05% change).

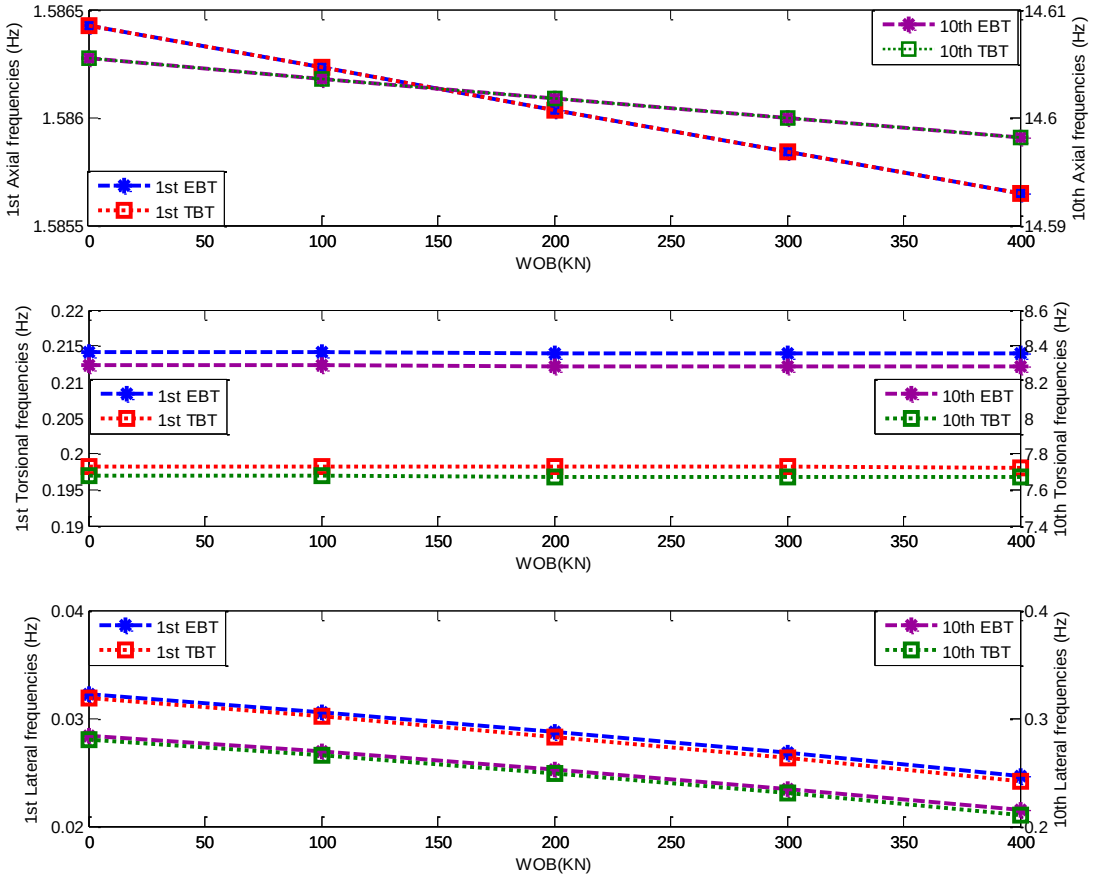

Figure 2.7. First and 10th Natural Frequencies with Varying Axial Load for Euler-Bernoulli (EBT) and Timoshenko (TBT) Models

Figure 2.8 shows the effect on the first and 10th modes when increasing the length of the drill pipe while maintaining the same drill stem configuration. The left and right axes in Figure 2.8 follows the same conventions as Figure 2.7.

The increase in the length of drill pipe causes the drill stem first natural frequency to decrease (Figure 2.8). At 500 m, the lateral frequency of the Euler-Bernoulli model is higher than for the Timoshenko model by 0.8% and 0.95% for the first and 10th mode respectively. While at 2700m, the Timoshenko model frequencies are less than those predicted by the Euler-Bernoulli model by 1.2% for the first and 10th mode. At higher torsional modes, the difference between the two model results increases. For the 10th mode at 540 m, the difference between Euler-Bernoulli and Timoshenko model result is 4.135 Hz, while at 2700 m; the difference is only 0.4 Hz. The change in length of the drill pipe

from 500 m to 2700 m have a higher impact on the drill stem frequencies than changing the axial load from 0 KN to 400 KN, this is due to the wavelengths are longer compared to the thickness of the drill stem. The change in the drill pipe length causes a decrease in lateral, torsional, and axial frequencies by 46.5%, 60%, and 78% respectively, for the first mode, while for the 10th mode the change in frequencies was 56.5% for the lateral, 77% for torsional, and almost 75% for axial.

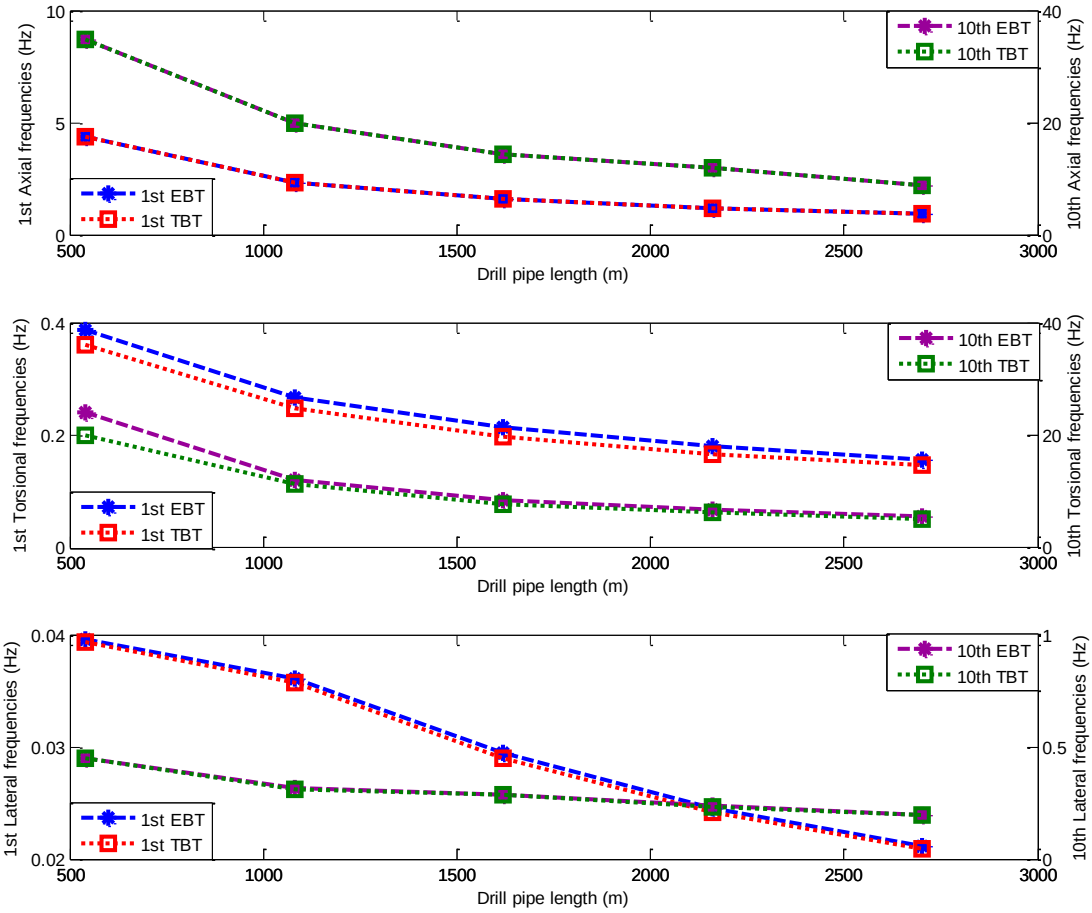

Figure 2.8. Length of Drill Pipe Effect on Drill Stem First and 10th Natural Frequencies using Euler-Bernoulli and Timoshenko Models

Maintaining the same drill stem configuration and the applied load, the effect of changing the length of drill collar on the drill stem natural frequencies is shown in Figure 2.9, where the left and right axes follow the same conventions as Figure 2.7 and Figure 2.8.

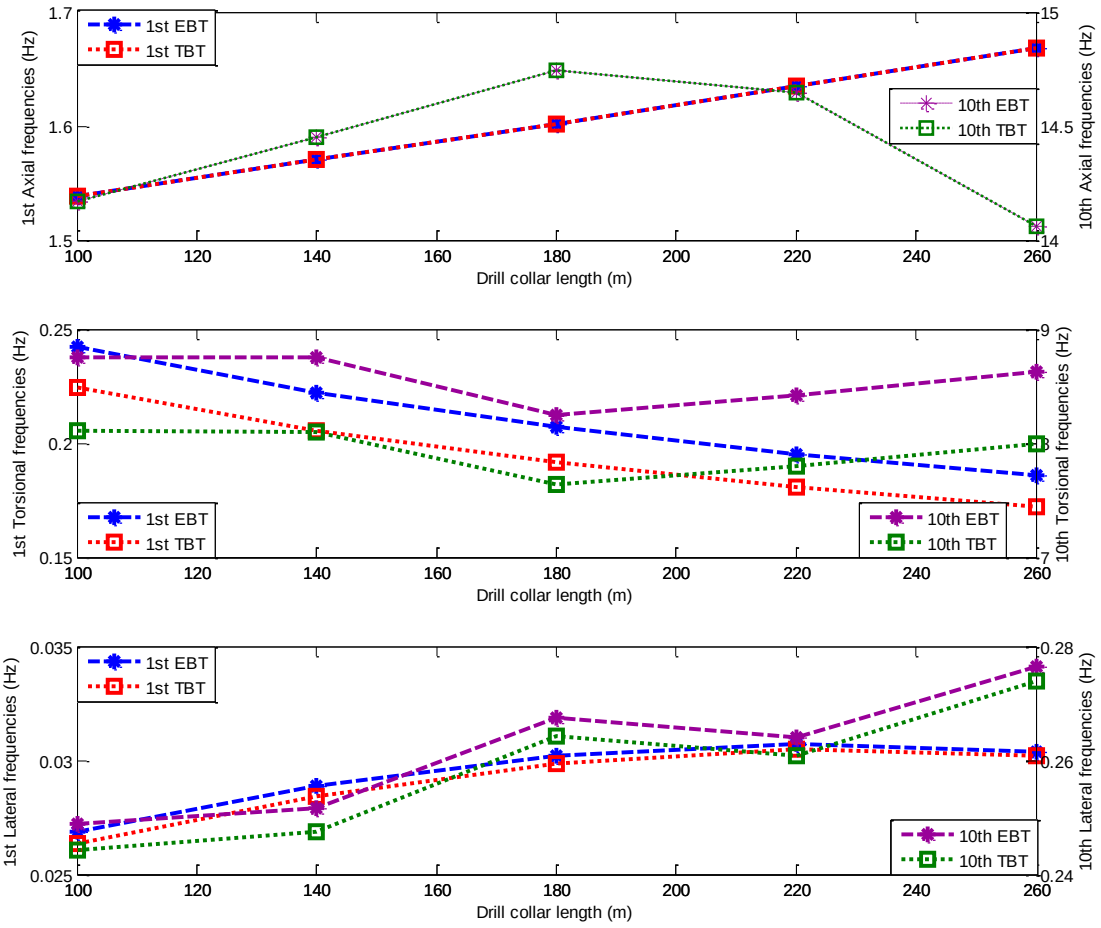

Figure 2.9. Effect of Drill Collar Length on the Drill Stem's First and 10th Natural Frequencies

Increasing the length of drill collar section causes the axial and lateral natural frequencies to increase, while torsional natural frequency decreases for the first mode. For the 10th mode however, nonlinear relationship between the drill collar length and natural frequencies is noticed in Figure 2.9. With 100 m long drill collar, the percentage difference between Euler-Bernoulli and Timoshenko models is 2.6%, while with 260 m long drill collar, the difference is 0.8% for lateral modes. For torsional modes, the difference between the two models at the first and 10th modes is 7.4%. The change in drill collar length from 100 m to 260 m caused a 20% increase in lateral frequency, a 7.5% increase in axial natural frequency, and a 38.5% decrease in torsional frequency. While for the 10th mode, the

effects were 9% increase in lateral frequency, 1.7% decrease for both Euler-Bernoulli and Timoshenko torsional frequency, and 3.5% decrease in axial natural frequency.

The same drill stem configuration given in Table 2.4 (base case) is used to investigate the influence of fluid density on the drill stem lateral natural frequencies. At first, 850 kg/m^3 density is used representing oil based drilling fluid, then the density was increased up to 1700 kg/m^3 representing weighted water based drilling fluid. (Figure 2.10)

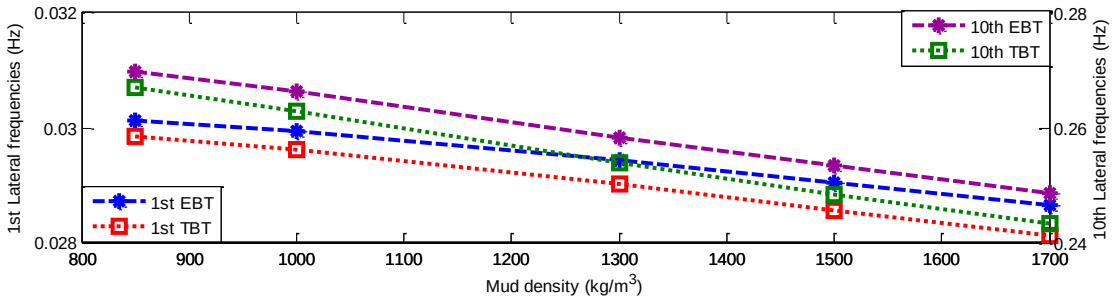

Figure 2.10. Effect of Fluid Density on the Drill Stem First and 10th Lateral Natural Frequencies

A 4% decrease of lateral natural frequency is caused by increasing the fluid density for the first mode, while 7% decrease for the 10th mode. The difference in lateral frequency obtained using Euler-Bernoulli and Timoshenko models is 0.8%, as density increase, the difference also increases by 1.8% at 1700 kg/m^3 for the first mode and for the 10th mode the difference was 1% and 2% respectively for each model.

The sensitivity study of Euler-Bernoulli and Timoshenko models under varying weight on bit, length of drill pipe, length of drill collar and fluid density shows an average difference of less than 1 RPM for the first mode. For the 10th mode, the difference between the two models under varying weight on bit, length of drill collar and fluid density is approximately 6 RPM. At a short length of drill pipe the difference between the two models was 39.5 RPM difference, which is a nonrealistic situation for drilling operation, however, when excluding the short length of drill pipe (540 m drill pipe length), the average difference between the under increasing length of drill pipe is approximately 4%.

2.5. SUMMARY

In this chapter, a parametric study was performed using nonlinear six degree of freedom node using Euler-Bernoulli and Timoshenko theories for modeling of the drill stem vibration. The nonlinear finite element models, including three vibration modes derived here, were verified with simplified uncoupled analytical models and one existing finite element model. The main conclusions drawn from this chapter are:

- The average difference of the lateral natural frequencies of the first ten modes using both models is 1.35% which translates to difference of 1 RPM, due to the wavelengths are long compared to the thickness of the drill stem.
- The parametric study showed that torsional natural frequencies for the Euler model are higher than Timoshenko model by an average difference of 7.4% for the first ten modes.
- For axial frequencies no significant change was observed between the two models.
- The maximum difference between the two models for all vibration modes at normal drilling conditions translates to 6 RPM when considering the first ten modes, thus at normal operating conditions the use of the nonlinear Euler-Bernoulli's assumptions can be justified.
- Based on the models formulation and data used in the chapter, the increase in axial load reduces the lateral natural frequencies for both models with a small effect on axial and torsional natural frequencies.
- Increasing the axial load and decreasing the length of the drill collar causes the difference of the first lateral natural frequencies between the two models to increase.
- Drill stem lateral, axial, and torsional natural frequencies are more sensitive to the change of drill pipe length, where the natural frequencies changes dramatically under varying length of drill pipe.
- Increasing the length of drill collar increases both lateral and axial natural frequencies and decrease torsional frequencies.

- The percentage difference in the first lateral natural frequency increases under higher axial load and shorter drill collar length. However, the percentage difference in the first torsional natural frequency does not change with the change of any parameter.
- Including fluid forces influences lateral frequencies with a maximum change of 5.8% at the first mode and 8% at the 10^{th} mode.

3. DRILL STEM VIBRATION MODELING AND FIELD DATA ANALYSIS OF INCLUDING VIBRATION DAMPENING TOOLS

To avoid severe vibrations, drill stem vibration models are used to predict and avoid resonance regions. In addition to avoiding critical speeds for a given BHA, specialized tools, such as shock subs and vibration dampening tools, are used to reduce generated drill stem vibrations which can occur while drilling. The axial shock sub uses an axial spring that is adjusted to the harmonics produced by the weight on bit fluctuations due to drill bit contact with the formation while drilling. The objective of this chapter is to investigate the causes of these vibrations as well as the effect of including drill stem vibration mitigation tools in the BHA design by analyzing field data and modeling vibrations.

3.1. INTRODUCTION

Based on the conducted literature review in Chapter 1, torsional vibration subs (Selnes et al. 2009) and imbalance vibration subs (Gaines et al 2013) are commonly deployed in modern BHA design to mitigate drill stem vibration. However limited studies on the performance of BHA with vibration reduction tools have been reported.

Ghasemloonia et al. (2014) studied the effect of different axial shock sub designs with a coupled axial-lateral analytical and finite element vibration model. Their model included the effect torque, damping due to drilling fluid, spatially varying axial force, downhole vibration generator, and drill stem contact with the wellbore wall. The effect of axial shock sub was included by considered a discrete spring and dashpot damping component. However, they did not address torsional damping subs or imbalance vibration subs.

The main objective of this chapter is to investigate the drill stem vibration, including analysis of vibration reduction tools in the BHA design and operating parameters selection in order to avoid drill stem vibrations and increase drilling performance. The first vibration reduction tool considered in this study is a torsional vibration sub (TVS) and the second tool is an imbalance vibration sub (IVS) presented in Chapter 1.2.4.

The investigation was carried out in two steps. The first step involved analyzing drill stem vibrations collected from three wells. The second step consisted of modeling the vibration reduction tools used in two wells.

3.2. DRILLING AND VIBRATION FIELD OBSERVATIONS

Drill stem vibrations were collected from three wells in the North Sea using a memory dynamic downhole recorder (Schen et al. 2005). The device measures lateral acceleration, root mean square (RMS) of lateral vibration, centripetal acceleration and downhole RPM. The lateral vibration measures the peak shocks in unit force g, while lateral RMS acceleration is used as a lateral vibration intensity indicator. The interpretations of both lateral and lateral RMS vibrations are tabulated in Table 3.1. The reservoir section consist of unconsolidated conglomerate and granitic basement.

Table 3.1. Classification of Vibration Measurements

Lateral Acceleration		**Lateral RMS Acceleration**		**Stick-Slip**	
(g's)	**Severity Level**	**(g's)**	**Severity Level**	**(-)**	**Severity Level**
0-15	Normal	0-2.5	Normal	0-0.5	Low
15-35	Moderate			0.5-1	Moderate
35+	Severe	2.5+	Severe	1+	Severe

The centripetal acceleration was used to evaluate torsional vibrations. Stick-slip severity was calculated based on the measured downhole RPM according to McCarthy et al. (2011):

$$Stick-slip(\%) = \frac{\Delta RPM_{Downhole}}{RPM_{Surface}} \times 100 \tag{51}$$

Where, $\Delta RPM_{Downhole}$ refers to the difference between maximum and minimum downhole RPM measured in one period, which is determined by the data sampling rate, and $RPM_{Surface}$ is the measured surface RPM. The interpretations of stick-slip severity are tabulated in Table 3.1. The three wells are located in the same area with similar geology. The formations' depth and their respective thickness of Well A and Well B are listed in Table 3.2.

Table 3.2. Well A and Well B Formations'

Formations	Start Depth (m)		End Depth (m)		Thickness	
	Well A	Well B	Well A	Well B	Well A	Well B
Utsira	773.5	800	869	877	96	77
Skade	994	940	1188	1007	194	67
Grid	1499	1276	1552	1350	53	74
Balder	1767	1350	1778	1387	11	37.5
Sele	1778	1387	1800	1395	21	8
Lista	1800	1395	1881	1465	81	69
Vale	1881	1465	1895	1485	14	20

Vibration measurement subs were located at multiple locations in the drill stem. For Well A and Well B, vibrations were measured at three locations, while for Well C, vibration data was collected at two locations. A torsional vibration sub was used in Well A's BHA, while an imbalance vibration sub was included in Well B's BHA. Well C was a short section, 303 m section, drilled in the reservoir section without any vibration reduction tools. To reach the target depth, three bit runs were used in all three wells (Table 3.3). The collected drilling and vibration data used in the study were collected based on depth and are presented in Appendix E. The vibration measurements sub records minimum, maximum and average, vibrations (Schen et al. 2005). The collected data were measured

in non-uniform sampling rate, where the measurement subs recorders the vibrations over a certain period of time.

Table 3.3. Summary of Bit Runs

Well	Bit size (in)	Length (m)	Damping Tool	Bit Type	MW (Sg)	WOB (tons)	Rotary RPM
A	12.25	585-1880	TS	PDC	1.3	1-12	120-152
	8.5	1976-2150	TS	PDC	1.34	6-13	120-150
B	12.25	763-1803	AVD	PDC	1.3	2-6	138
	8.5	1803-1913	N/A	PDC	1.2	5-9	150
	8.5	1961-2020	N/A	PDC	1.2	10-12	130
C	8.5	2000-2200	N/A	Roller Cone	1.31	12-15	128
	8.5	2200-2270	N/A	PDC	1.33	5-12	50-81
	8.5	2270-2303	N/A	PDC	1.33	4-12	40-120

Well A was drilled with a torsional vibration sub vibration reduction tool, Figure E.1 (Appendix E) shows the depth based data consisting of weight on bit (WOB), torque, surface and downhole RPM, gamma ray (GR), sonic log, lateral acceleration, lateral RMS acceleration, centripetal acceleration, and stick-slip indication. The first section of Well A with BHA 1 shows small downhole RPM fluctuations (+/- 10 RPM) at the start of the section (585-758 m) with normal lateral vibration and no lateral shocks (Figure E.1). In the Utsira formation (774- 900 m) an increase in stick-slip severity to moderate levels with the increase of downhole RPM fluctuations and centripetal accelerations, indicate an increase of drill stem torsional oscillations. The increase in stick-slip severity caused small lateral shocks to occur when entering the sand rich Utsira formation, as noticed by a decreased of GR reading. Lateral intensity (RMS) vibrations reached to the severe levels when drilling through this sand. This same behavior was noticed in the Grid sandstone formation as well. When reaming out the core section, low lateral and torsional vibration levels were observed when drilling with low surface RPM (around 80 RPM). After reaming down to 1975 m and

drilling commenced, downhole RPM fluctuations increased with moderate levels of stick-slip severities for the entire section. The erratic downhole RPM caused an increase in torsional oscillations with a severe lateral RMS vibration for the rest of the section.

For Well B, the first section (800-1800 m) was drilled with the imbalance vibration sub (IVS). Figure E.2 (Appendix E) shows the operating drilling parameters and vibration log data for the well. While drilling through the sandy formation from depth 800 m to 850 m and from 950 to 1000 m, downhole RPM fluctuations increased as gamma ray readings decreased. At 980 m, the surface RPM was increased to 150 RPM in the sandy formation (lower gamma ray readings) without increasing weight on bit, which resulted in an erratic downhole RPM and increase in lateral vibration severity.

The first section of Well C (2000-2200 m) was drilled with a roller cone bit. Low stick-slip severity and moderate level of lateral vibrations was achieved due to the bit type (Figure E.3 Appendix E). Lateral vibrations intensity (RMS) did not exceed the moderate level for the whole section. For the second and third sections of Well C, PDC bits were used resulting in a noticeable increase in torsional vibration and stick-slip severity. High frequency of erratic downhole RPM suggests torsional vibrations are dominating. Both sections had severe stick-slip and lateral vibrations close to the end. The stick-slip severity was high at the start of the section and at the end of the section. This increase in stick-slip caused lateral vibration to increase to the severe level.

The influence of geological formation on vibrations were analyzed using box plots. Figure 3.1 shows the distribution of lateral RMS accelerations for each geological formation of the three wells, while Figure 3.2 shows the distribution of delta RPM (difference in downhole and surface RPM) for each formation.

Figure 3.1 shows that lateral RMS vibrations were lower in every formation when using the imbalance vibration sub, while the maximum lateral RMS was encountered in the reservoir section with Well A using the torsional vibration sub. The difference in surface and downhole RPM (stick-slip indication) in the first formation (Utsira) using the torsional vibration sub was lower than the imbalance vibration sub (Figure 3.2). The maximum difference between surface and downhole RPM (delta RPM) was encountered at the reservoir section without vibration reduction tools in Well C.

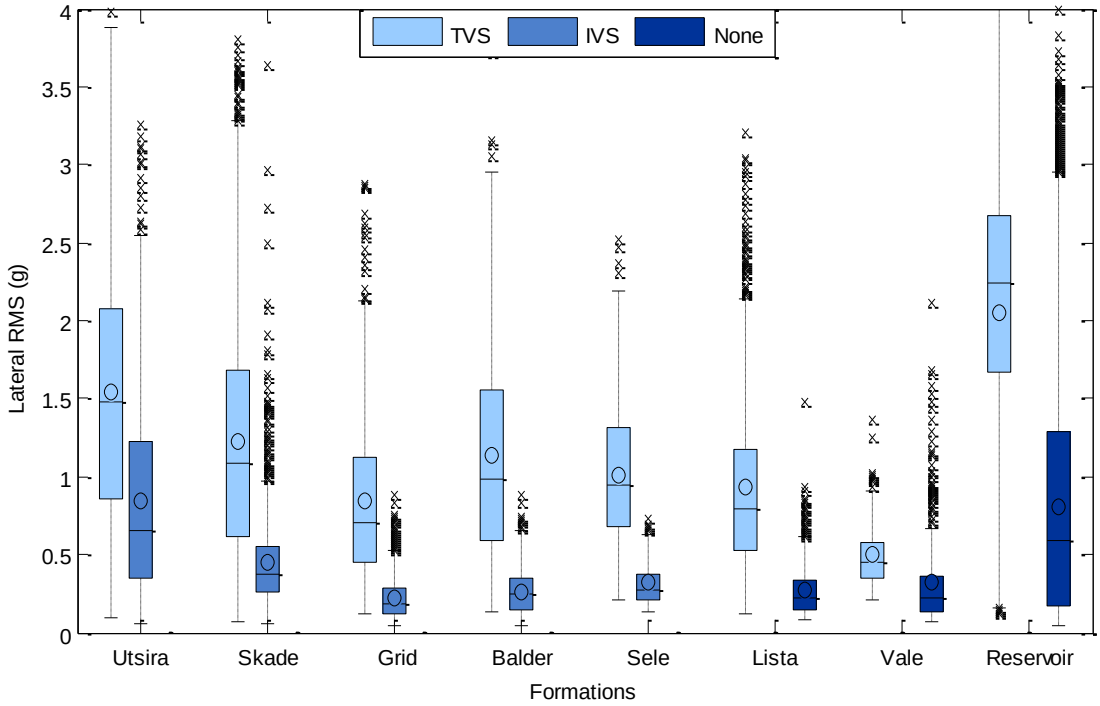

Figure 3.1. Lateral RMS Vibrations per Formation using the Torsional Vibration Sub (TVS), Imbalance Vibration Sub (IVS) and No Vibration Dampening Sub (None)

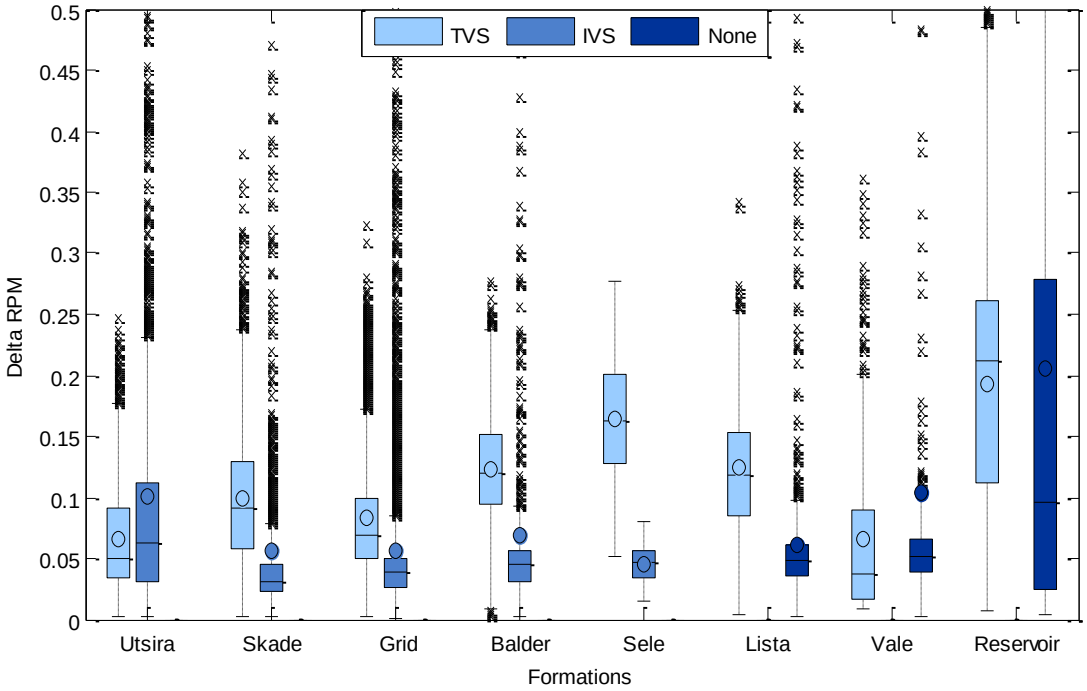

Figure 3.2. Difference Between Surface RPM and Downhole RPM (Delta RPM) per Formation using the Torsional Vibration Sub (TVS), Imbalance Vibration Sub (IVS) and No Vibration Dampening Sub (None)

Torsional vibration intensity increased at every sandy formation (below GR reading of 65 API), causing an increase in lateral accelerations. Two zones with low and high GR readings were chosen in the Grid formation to test whether there is a statistical difference in lateral vibrations at both zones using the t-test (Minitab 17, 2010). A high t-value (t=17.63) was obtained with low probability (P-value < 0.0001), which resulted in the rejecting the null hypotheses and the conclusion that the two samples are different. Statistically, the sample with low GR reading (sandy formation) had higher lateral vibrations than the sample with higher GR readings.

The overall vibration data (including lateral and centripetal RMS acceleration), rate of penetration (ROP), and rock strength are analyzed in Figure 3.3.

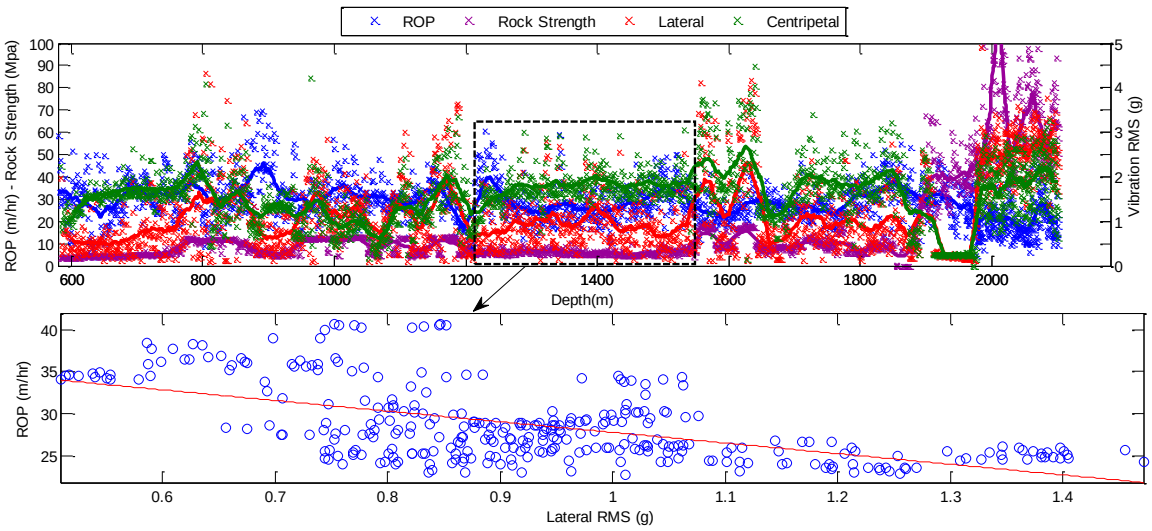

Figure 3.3. Well A (a) Overall Vibration, ROP, and Rock Strength (b) Isolated Region with Constant Rock Strength

The rock strength was calculated based on sonic travel time correlations from to Hareland and Nygaard, (2007a). A section with constant rock strength was selected to normalize the influence of lithology (Figure 3.3a). A scatter plot of ROP and lateral RMS acceleration with constant rock strength (Figure 3.3b) shows the influence of lateral vibrations on drilling performance. The linear regression line shows a noticeable overall

trend, indicating that ROP tends to decrease as lateral vibration increases. Higher ROP (above 30 m/hr) was not seen when lateral vibrations were above 1.1 g (Figure 3.3b).

The torsional vibration of the drill stem near the torsional vibration sub is evaluated by analyzing the maximum and minimum downhole RPM with respect to the surface RPM and measured centripetal accelerations. Figure 3.4a, b shows the applied surface RPM with measured downhole RPM above and below the torsional vibration sub respectively.

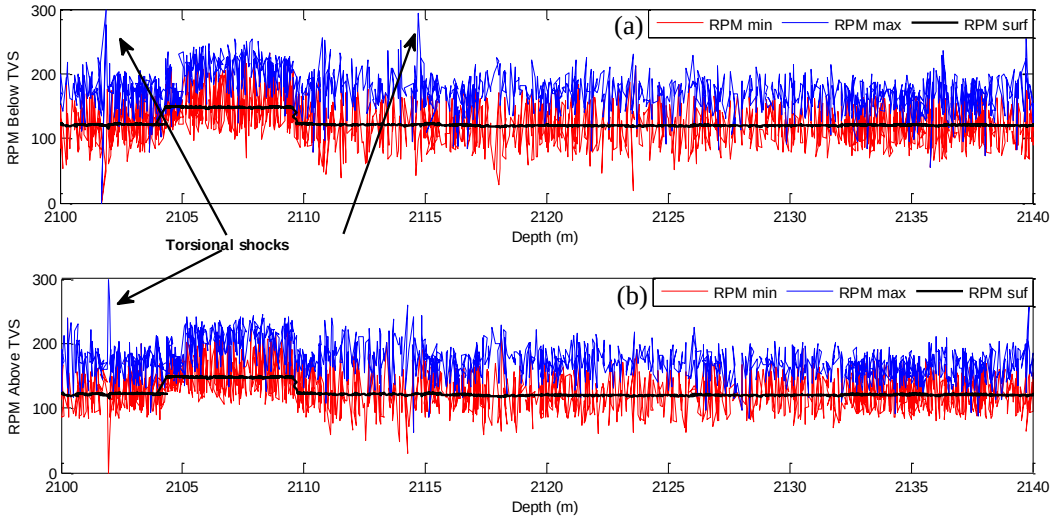

Figure 3.4. Maximum and Minimum Downhole RPM at (a) Below the Torsional Vibration Sub (TVS) (b) Above the Torsional Vibration Sub (TVS)

Two distinguished shocks (spikes) were identified below the torsional vibration sub. Above the TVS sub, only one shock was seen, indicating that the shock was dampened due to the TVS sub, and noting that stick-slip severity was in the moderate range (Figure 3.4). At 2115 m after the second shock, surface RPM was decreased causing stick-slip severity to decrease.

Lateral RMS vibration severity measured near the bit, below and above the torsional vibration sub versus weight on bit (WOB) and applied rotary speed is shown in Figure 3.5(a, b, c) respectively for Well A.

The behavior of the lateral RMS vibrations (Figure 3.5 a, b, c) can be divided into two parts; low and high lateral vibrations. The low lateral RMS levels were encountered

during drilling the cored section. When drilling started, lateral RMS vibrations near the bit increased to the severe level. Comparing lateral RMS acceleration levels at different locations, the highest accelerations were recorded near the bit (Figure 3.5a), while lateral vibrations decreased going up the drill stem (Figure 3.5 b and c).

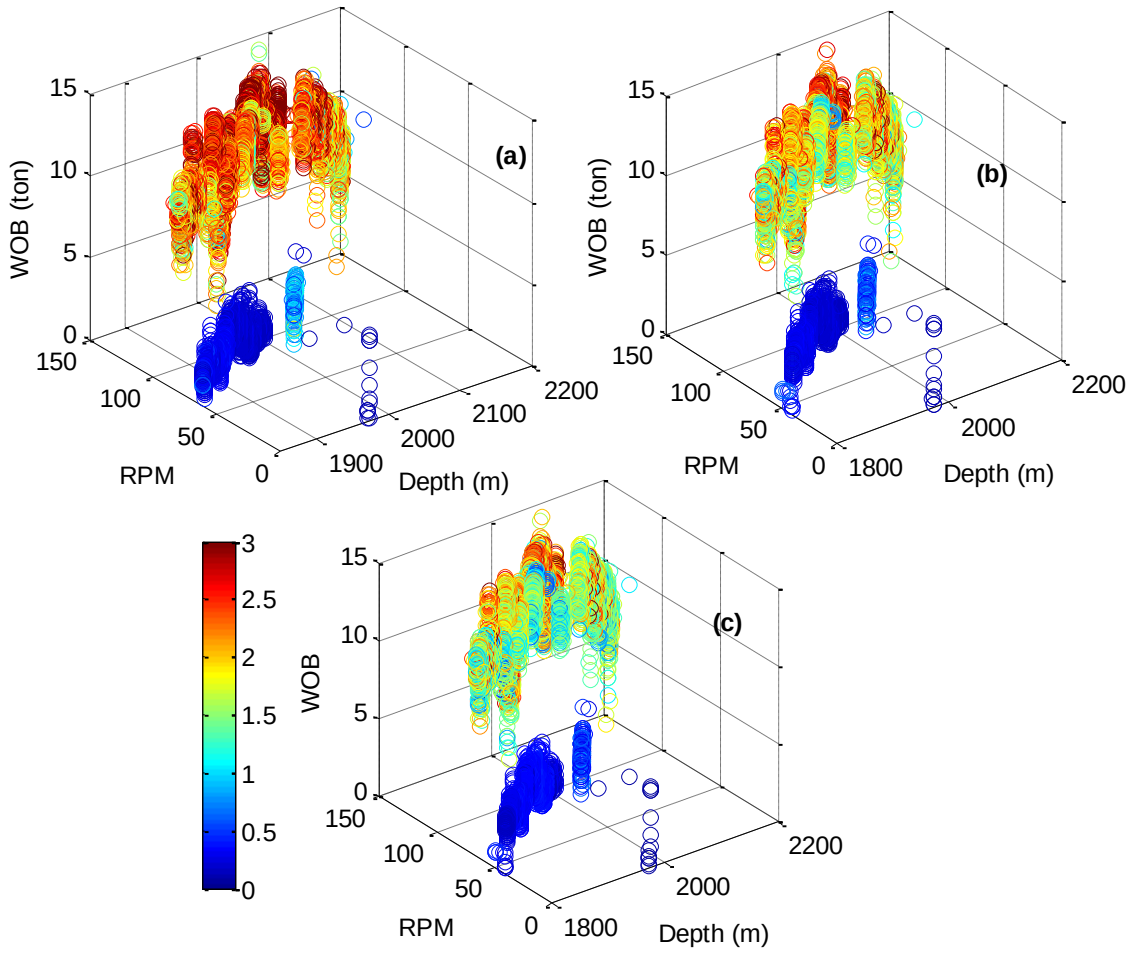

Figure 3.5. Lateral RMS Vibrations at (a) Near Bit (b) Below TVS Tool (c) Above TVS Tool

Applied surface RPM with the measured downhole RPM and the corresponding measured lateral vibrations using the imbalance vibration sub for Well B are shown in Figure 3.6.

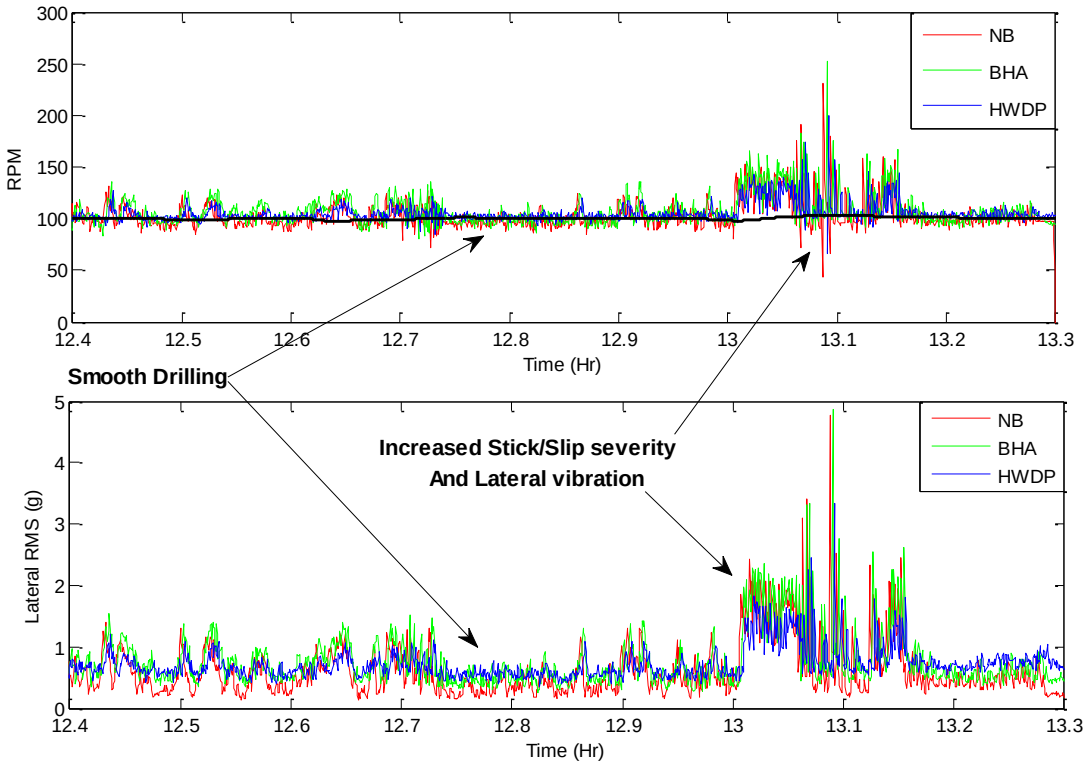

Figure 3.6. Downhole, Surface RPM and Lateral RMS Vibrations using the IVS Sub Measured at 781-808 m

Figure 3.6 shows the applied surface RPM with the measured downhole RPM and the corresponding measured lateral vibrations using the imbalance sub for Well B. Smooth drilling was achieved with 100 RPM at surface, however, when the RPM was increased by 5 RPM, the downhole RPM increased to almost twice the applied surface RPM, causing an increase in lateral vibration. With this increase in downhole RPM for Well B, stick-slip severity was still at moderate levels. Using the imbalance vibration sub seems to reduce lateral shocks as only a few lateral shocks were observed in the first run.

3.3. MODEL FORMULATION AND NUMERICAL SOLUTION

The drill stem was modeled as a rotating cylinder (Figure 1.1) following the approach of Heisig and Neubert, (2000); Ahmadian et al. (2007); Ghasemloonia et al. (2013); and Ghasemloonia et al. (2014). The final equation of motion of the drill stem is:

$$([M]+[M_f])x+\ [C]+[G]\ x+\ [K]+[K_G]+[K_F]\ x = f_g+f_f+f_f+\mathrm{F}\ \mathrm{t} \tag{52}$$

Where $[M]$ is the drill stem mass matrix, $[M_f]$ is the fluid mass matrix, $[C]$ is the damping matrix, $[G]$ is the gyroscopic matrix, $[K]$ is the drill stem stiffness matrix, $[K_G]$ is the geometric stiffness matrix, $[K_F]$ fluid stiffness matrix, f_g is the gravity force vector, f_f is the fluid force, f_r is the reaction force at the bit, and $F\ t$ is the time dependent forces. Detailed derivation of the equation of motion using the Euler-Bernoulli's assumption is discussed in Chapter 2 starting from page 18.

3.3.1. Torsional Vibration Sub (TVS). The torsional vibration sub is treated as a torsional spring with dash-pot damping (Figure 3.7). The axial and lateral element properties of the torsional sub are similar to the drill stem properties, while the torsional vibration sub stiffness is added to the torsional degree of freedom (θ_x) with a dash-pot damping component added to the element damping matrix.

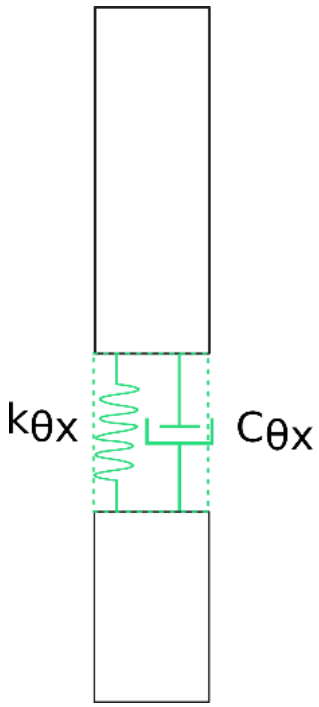

Figure 3.7. Simplified Torsional Sub Model

The tool stiffness and damping matrix take the form of:

$$K_{TVS} = K_{12\times12} + K^{TS}_{12\times12} \tag{53}$$

$$C_{TVS} = C_{12\times12} + C^{TS}_{12\times12} \tag{54}$$

Where, K is the drill stem element stiffness matrix and K^{TS} is the added stiffness matrix of the torsional vibration sub. The nonzero entries of K^{TS} in Equation 53 are:

$$K^{TS}\ 1{,}6\ = K^{TS}\ 12{,}12\ = -K^{TS}\ 1{,}12\ = -K^{TS}\ 12{,}6\ = K_{\theta_{TS}} \tag{55}$$

And the nonzero entries of C^{TS} in Equation 54 are:

$$C^{TS}\ 1{,}6\ = C^{TS}\ 12{,}12\ = -C^{TS}\ 1{,}12\ = -C^{TS}\ 12{,}6\ = C_{\theta_{TS}} \tag{56}$$

3.3.2. Imbalanced Vibration Sub (IVS). The imbalanced vibration sub has an off center mass that was modeled as an unbalanced force, assuming that the off balance mass does not contribute to the element's flexibility. The unbalance mass is also assumed to be a purely concentrated mass, where the moment of inertia and polar moment of inertia are both zeros. The stiffness and mass matrices of the imbalance vibration sub were modeled as one of the drill stem elements and unbalanced forces are applied at the lateral direction of the drill stem (Figure 3.8), where the applied force is located at the center of the unbalance mass location within the tool.

The applied unbalance force at the lateral directions v and w are for the imbalance vibration sub:

$$F_v = M_b\ \Omega\ v_{im}\ cos\ \Omega \times t \tag{57}$$

$$F_w = -M_b\ \Omega\ w_{im}\ sin\ \Omega \times t \tag{58}$$

Where, M_b is the weight of the unbalanced mass, Ω is the rotational velocity, v_{im} and w_{im} are the distance from the geometric center off mass to the center of the unbalanced mass, and t is the time.

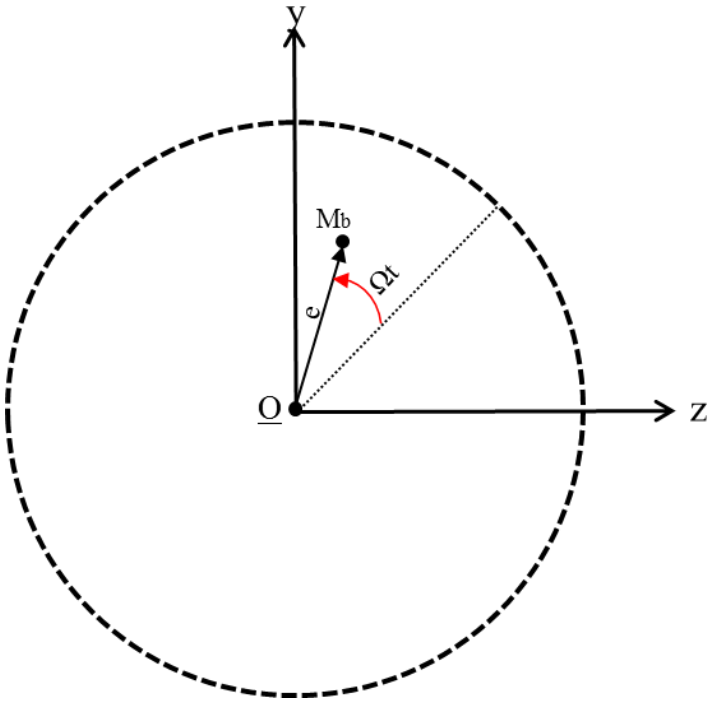

Figure 3.8. Unbalance Mass Force

3.3.3. Numerical Integration. To obtain the critical speeds (natural frequencies) and vibration patterns of the drill stem, the generalized Eigenvalue problem is formulated according to Equation (45. The model calculates the natural frequencies of each BHA for several lengths of drill pipe using the QR algorithm defined in the Matlab® (Appendix F). The critical speeds were calculated in 270 m length increments for the three wells.

The central difference method was used to solve the equation of motion (Equation 52) of the drill stem. The following algorithm was used to compute the solution of the equation of motion (Kwon and Bang, 2000);

1. Compute the system mass, stiffness, gyroscopic, and stiffness matrices
2. For each time step (t_i)

a. Compute the acceleration as:

$$\{x\}^t = [M]^{-1}\ \{F\}^t - \ [C] - [G]\ \{x\}^t - [C] - [K]\{x\}^t \tag{59}$$

b. Compute the velocity from the computed acceleration as:

$$\{x\}^{t+\frac{\Delta t}{2}} = \{x^{t-\frac{\Delta t}{2}}\} + \Delta t\{x\}^t \tag{60}$$

c. Compute the displacement from the computed velocity as:

$$\{x\}^{t+\Delta t} = \{x\}^t + \Delta t\{x\}^{t+\frac{\Delta t}{2}} \tag{61}$$

The used central difference method is conditionally stable, where the critical stable time step ($\Delta t_{critical}$) is defined as:

$$\Delta t_{critical} <= \frac{T_{min}}{\pi} \tag{62}$$

Where, T_{min} is the minimum period. The minimum period is obtained from a free vibration analysis, where the period is defined as:

$$T_{min} = \frac{1}{\omega_{min}} \tag{63}$$

The input data for each BHA was based on the applied operating parameters for each well (Appendix E). Table 3.4 shows the input parameters used for the three wells to determine the natural frequencies. l_{stab} In Table 3.4 refers to the stabilizer location measured from the drill bit (Figure 1.1a). For Well A, the torsional vibration sub is located 45 m above the bit, with a torsional spring stiffness of 7100 KN.m/rad. For Well B, the Imbalance vibration sub is located 115 m above the drill bit. The unbalanced mass used for the forcing function is 1500 Kg with an off center location of 0.03 and 0.01 m in the lateral

directions. The drill pipe and drill collar were discretized with 45 m and 5 m long elements for the three wells based on the analytical verification in Chapter 2.3.2 Page 32.

Table 3.4. Model Input Parameters

Common	Well A	Well B	Well C
$\rho = 7850\ Kg.m^{-3}$	$L_{dp} = 1080$ m	$L_{dp} = 1350\ m$	$L_{dp} = 1890\ m$
$E = 210\ GPa$	$L_{dc} = 215\ m$	$L_{dc} = 285\ m$	$L_{dc} = 145\ m$
$\upsilon = 0.29$	$ID_{dc} = 0.054\ m$	$ID_{dc} = 0.0605\ m$	$ID_{dc} = 0.058\ m$
$\rho_f = 1298\ Kg.m^{-3}$	$OD_{dc} = 0.216\ m$	$OD_{dc} = 0.203\ m$	$OD_{dc} = 0.171\ m$
$C_D = 0.0125$	$WOB = 39.5\ KN$	$WOB = 44\ KN$	$WOB = 117.5\ KN$
$U_i = 5$ m/s	$RPM = 150$	$RPM = 150$	$RPM = 127$
$D_w = 0.31\ m$	$l_{stab} = 35\ m$	$l_{stab} = 10\ m$	$l_{stab} = 5\ m$
$ID_{dp} = 0.108\ m$		$l_{stab} = 35\ m$	$l_{stab} = 20\ m$
$OD_{dp} = 0.127\ m$			

Where, ρ is the drill stem mass density, E is the Young Modulus, υ is the Poisson's ratio, ρ_f is the fluid mass density, C_D is the fluid discharge coefficient, U_i is the fluid flow velocity, D_w is the wellbore diameter, ID_{dp} is the drill pipe inside diameter, OD_{dp} is the drill pipe outside diameter, L_{dp} is the drill pipe length, L_{dc} is the drill collar length, ID_{dc} is the drill collar inside diameter and OD_{dc} is the drill collar outside diameter.

3.4. SIMULATION RESULTS

The simulations were divided into two parts to understand how each tool affects the drill stem vibrations. The first part (Section 3.4.1) evaluates drill stem vibrations' response with and without vibration dampening subs for the same BHA design and applied external forces. For the second set of simulations (Section 3.4.2), the actual BHA and operating parameters used for Well A, Well B, and Well C were used to validate the model with the behaviors seen in the vibration measurements.

3.4.1. Evaluation of Vibration Dampening Tools. The drill stem geometry for all the simulations in this section is the same, and consisted of a drill pipe with length of 1080 m, drill collar of 200 m long and one stabilizer located 100 m above the drill bit. All other dimensions and properties are obtained from Table 3.4. For the first scenario, a torsional vibration sub was included 30 m above the bit. For the second scenario, the torsional vibration sub was replaced with imbalance vibration sub at the same location. The third scenario was conducted without a vibration dampening sub in the BHA. The applied weight on bit and surface RPM were 150 KN and 100 RPM respectively.

Figure 3.9 and Figure 3.10 show the lateral and torsional displacements and their corresponding accelerations at the middle of drill pipe (540 m) and drill collar (1180 m) of the three scenarios respectively. In Figure 3.9 and Figure 3.10, the red solid line represents torsional vibration sub (TVS), the dashed blue line is imbalance vibration sub (IVS), and black dotted line is for the third scenario with no vibration dampening tool (None).

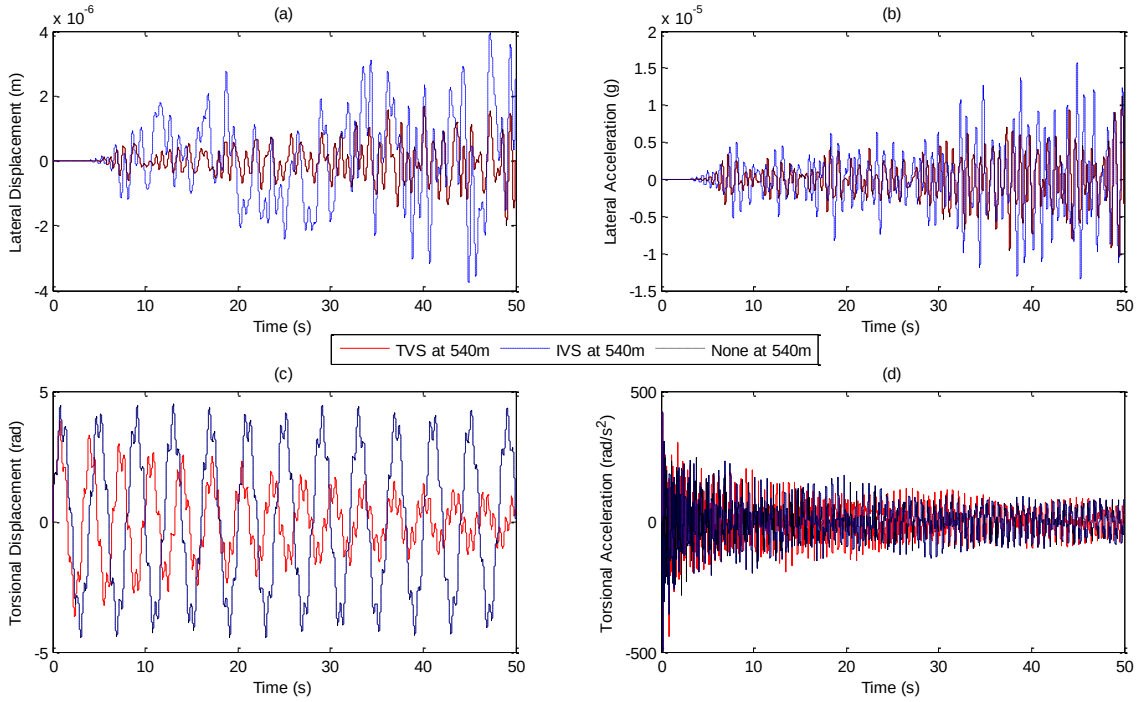

Figure 3.9. Drill Stem Response at the Middle of the Drill Pipe. (a) Lateral Displacement (b) Lateral Acceleration (c) Torsional Displacement (d) Torsional Acceleration

Lateral displacement and acceleration at the middle of drill pipe for the imbalance vibration sub scenario was higher than the other two scenarios (Figure 3.9.a, b). At the middle of the drill collar (Figure 3.10.a, b), the lateral displacement and acceleration of the first and third scenarios are similar and have higher peaks than the second scenario with imbalance vibration sub.

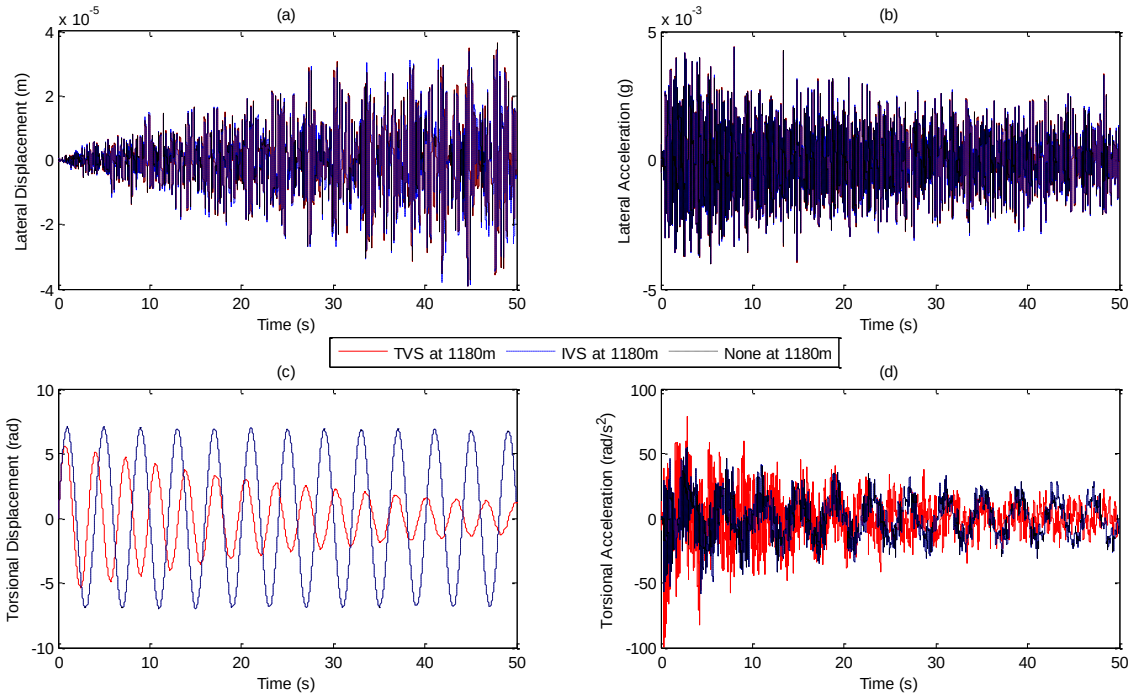

Figure 3.10. Drill Stem Response at the Middle of the Drill Collar. (a) Lateral Displacement (b) Lateral Acceleration (c) Torsional Displacement (d) Torsional Acceleration

Figure 3.9.c, d and Figure 3.10.c, d show the torsional displacement and acceleration at the middle of drill pipe and drill collar for the three scenarios. The torsional displacement of the imbalance vibration sub and no dampening scenario are identical and higher than the torsional displacement of the torsional vibration sub at both locations within the drill stem. Torsional acceleration of the torsional vibration sub scenario is comparable to the imbalance vibration sub and no dampening sub, with a phase shift and similar magnitude (Figure 3.9.c, d). The phase shift of the torsional acceleration at the middle of

the drill collar is more noticeable; however, the torsional acceleration of the imbalance vibration sub and no dampening sub is less than the torsional vibration sub scenario (Figure 3.10.c, d).

3.4.2. Model Validation with Field Data. Figure 3.11 shows the calculated critical RPM (using Table 3.4 input data) for Well A, B, and C. The calculated critical speeds are the solid lines and the actual applied surface RPM are the dashed lines for each well in Figure 3.11.

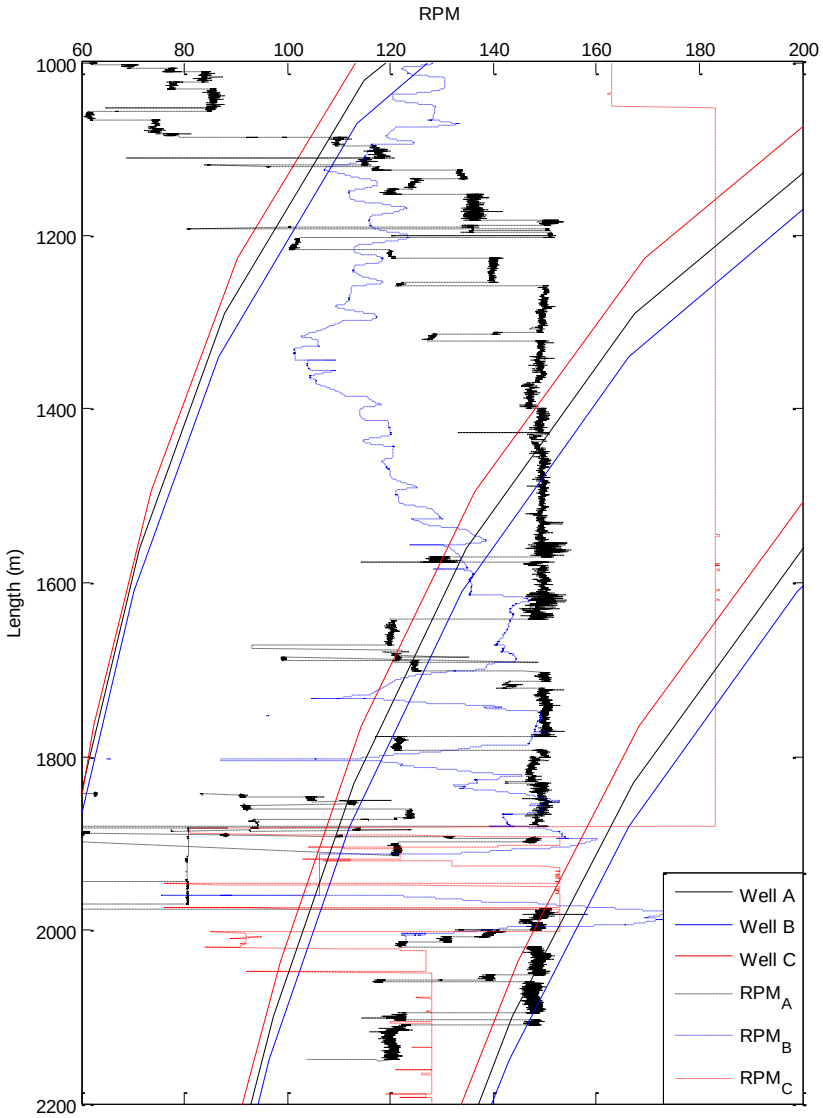

Figure 3.11. Well A (Black), B (Blue) and C (Red) Critical RPM (Solid Lines) and Applied Surface RPM (Dashed Lines)

The applied surface RPM in Well A was operated away from critical RPM for most of the section. For Well B, the applied surface RPM was 150 RPM at 1550 m, which was within the resonance regions of torsional vibration.

At 1609-1615 m the operating speed for Well B was 135 RPM, which is at one of the critical speeds for Well B; this explains the increase in vibrations to the severe level seen in the field (Figure E.2). Also at 2020-2100 m, the rotational speed was operated at the critical speed, resulting in increased torsional vibration at the section (Figure E.2).

The input parameters in Table 3.4 were used in the following simulations to compare the measured vibrations data with the modeling of the three wells. Figure 3.12 and Figure 3.13 show the lateral and torsional vibrations at the middle of drill pipe and near the bit (5 m above the bit) of the three wells respectively. The same line conventions in Figure 3.10 and Figure 3.11 were used in these simulations, where the red solid line represents Well A, the dashed blue line is Well B and the black dotted line is Well C.

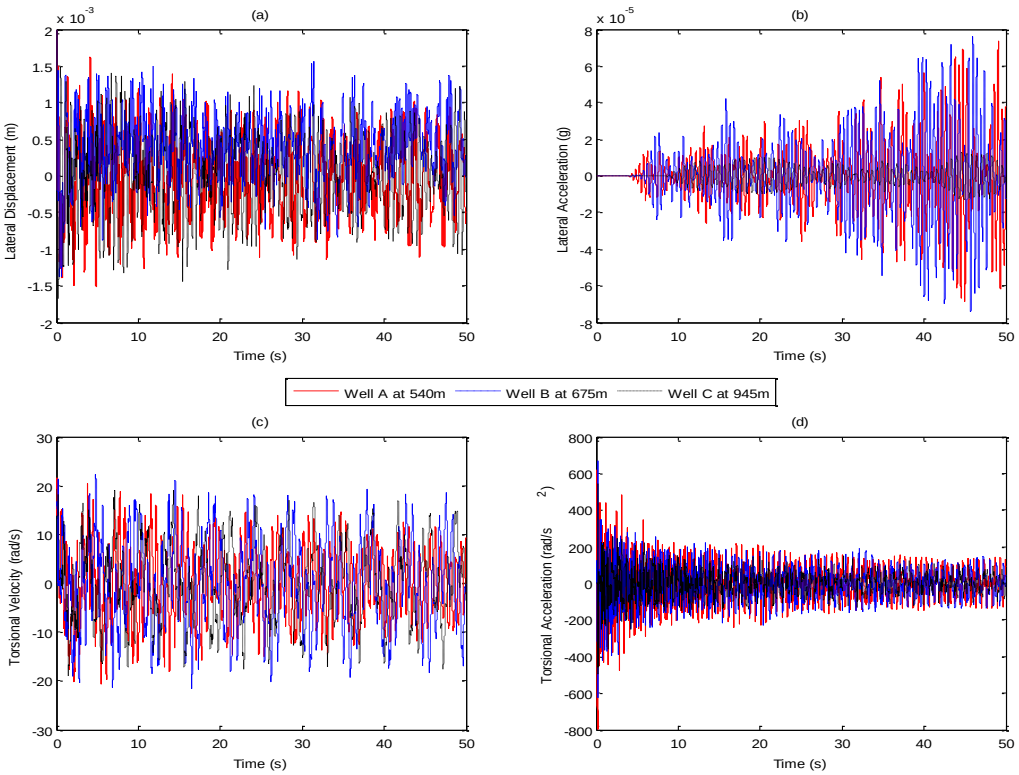

Figure 3.12. Drill Stem Response of the Three Wells at the Middle of the Drill Pipe. (a) Lateral Displacement (b) Lateral Acceleration (c) Torsional Velocity (d) Torsional Acceleration

Lateral displacement and acceleration of Well C were the lowest at the middle of drill pipe (Figure 3.12.a, b). Near the bit however, the lowest lateral vibrations were with Well B using IVS model (Figure 3.13.a, b). Well A and Well C have approximately the same lateral vibration magnitude, with Well C being slightly higher.

Figure 3.12.c, d and Figure 3.12.c, d show the torsional velocity and acceleration of the three wells at the middle of the drill pipe and near the bit respectively. The torsional velocity at the middle of drill pipe (Figure 3.12.c) is similar for the three wells with a small phase shift in the vibration amplitude, while the highest torsional acceleration (Figure 3.12.d) was at Well A including the TVS.

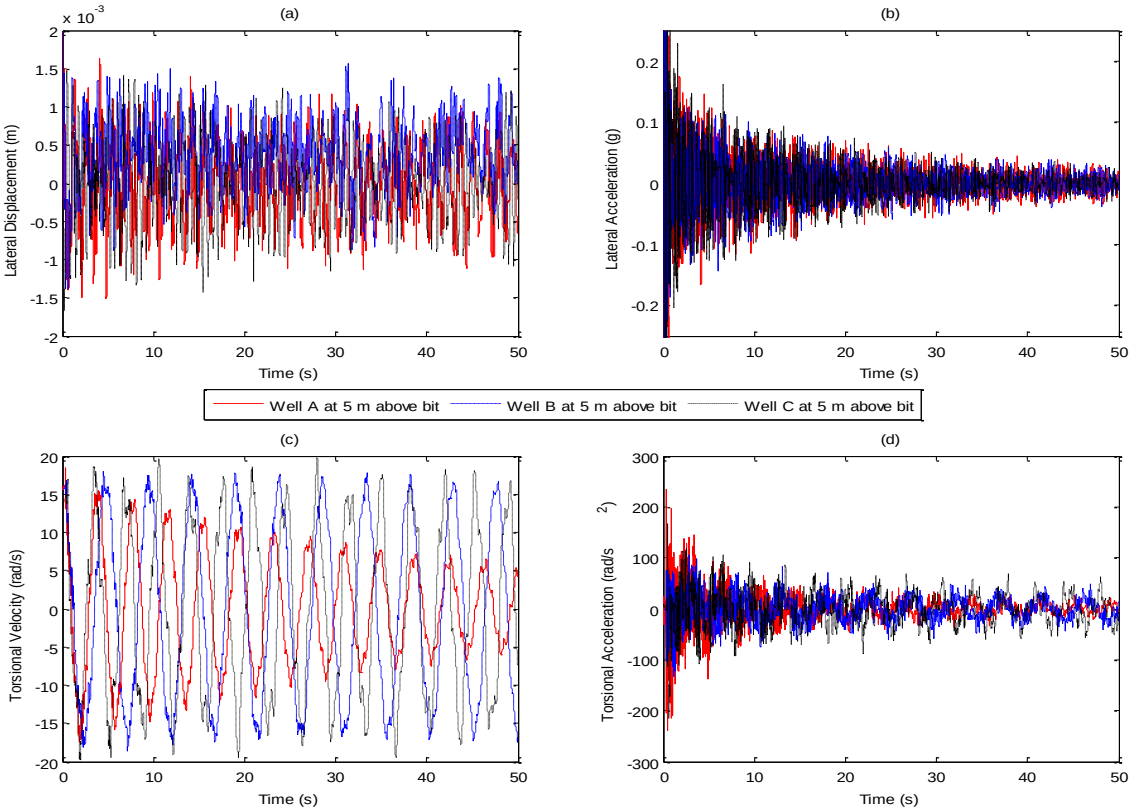

Figure 3.13. Drill Stem Response of the Three Wells Near the Bit. (a) Lateral Displacement (b) Lateral Acceleration (c) Torsional Velocity (d) Torsional Acceleration

Well C was forced with 127 RPM (13.3 rad/s) while Well A and B was forced with 150 RPM (15.7 rad/s). Even with this difference in applied rotational speed, Well C has

the highest torsional velocity and acceleration near the bit. Well A still has the lowest torsional velocity when using the torsional vibration sub, while the lowest torsional acceleration was noticed with Well B using the imbalance vibration sub (Figure 3.13.d), which follows the field observations.

3.5. DISCUSSION

From the measured drilling and vibration data, a correlation between drill stem vibration and lithological formations was identified. Torsional vibration tends to increase at every sandy formation. As gamma ray readings decreased below 65 API, lateral vibration and downhole RPM fluctuations increases, and the lateral-torsional coupling effect is more noticeable at these formations. Drill stem vibration and lithological formation also affect drilling performance. In similar rock strength, the rate of penetration decreases above a thrust hold value of 1.1 g lateral vibrations. Well B (using the imbalance vibration sub) showed the lowest lateral vibrations in every matching formation when compared with Well A (using the torsional vibration sub). Well C (no dampening sub) had lower lateral vibrations than Well A. Stick-slip severity using the torsional vibration sub (TVS) was lower in one formation (Utsira) compared to the imbalance vibration sub (IVS). For the rest of formations, the IVC was lower than the TVS. Stick-slip severity was lower using the TVS than the BHA without the dampening sub.

Modeling the top section of the drill stem, lateral vibrations were lower with no vibration dampening sub (Well C), however, at the BHA lateral vibrations were highest with no vibration dampening sub (Well C). The highest torsional vibration was encountered in Well C, which was also predicted by the models (Figure 3.13.d).

Lateral vibrations at the bottom of the drill stem are higher than the top of the drill stem. This behavior can be seen from both the vibration measurements (Appendix E) and model simulation (Figure 3.12 Figure 3.13). Even though vibration measurements were only recorded within the BHA, the lateral vibrations were decreasing while traveling up the drill stem. This was used as an indicator of low lateral vibration within the top part of the drill stem; however more accurate reading at the top section of the drill stem is needed for confirmation.

The use of the torsional vibration sub shows lower torsional vibration at the top of the drill stem, while the imbalance vibration sub shows lower lateral vibrations at the bottom of the drill stem. High torsional velocities were predicted by the model (Figure 3.13c) in Well C at 2035 m with 127 RPM and 117.5 KN weight on bit. The measured data at this location shows elevated torsional and lateral vibrations.

Vibration results (Figure 3.11) from the field and the modelling are shown to be correlated. As the operating surface RPM crosses the calculated critical RPM, drill stem vibration increases. The vibration measurements collects statistical data (average, maximum, minimum) over a non-uniform period of time which limits the extraction of the drill stem natural frequencies, the actual forcing behavior of the bit rock interaction and the forcing frequencies, which limits a direct numerical comparison between the field data and the numerical simulations.

As seen in the results and simulation above drill stem vibration dampening subs reduces torsional and lateral vibrations; however, even with vibration dampening subs, operating the drill stem at critical speeds causes an increase in drill stem vibrations. Predicting the critical operating parameters for a given BHA, with or without vibration dampening subs, is therefore an essential task that needs to be performed during the design phase.

3.6. SUMMARY

The effect of the two drill stem vibration damping subs was addressed in this chapter with the use of mathematical modeling and drill stem vibration measurements collected from three wells. The following conclusions are drawn:

- The drill stem vibration model was capable of predicting the behavior seen in the vibration measurements of the three wells.
- Lateral vibrations are higher in the bottom hole assembly which is under compressional force compared to the drill pipe in tension in contrast to torsional vibrations which are higher in the top of the drill stem compared to the bottom of the drill stem.

- Torsional vibration increases at every sandy formation, causing lateral vibration to elevate as gamma ray readings decreases below 65 API; lateral vibration and downhole RPM fluctuations increases as well.
- The rate of penetration (ROP) decreased when lateral vibrations exceed a threshold of 1.1 g.
- Drill stem vibrations increases regardless if vibration dampening tools is included when operating at critical speeds, yet including drill stem vibration dampening tools reduces drill stem vibration and decreases stick-slip tendency.
- In this study, the imbalanced vibration sub had the lowest lateral vibration compared to the other two cases, no vibration reduction sub and torsional vibration sub, respectively.

4. EFFECT OF DRILLING HYDRAULICS ON DRILL STEM VIBRATIONS

Drilling fluids have a complex rheology that needs to meet specific standards to maintain a stable wellbore, efficient cutting removal, and lubricate and cool equipment, while drilling. Drilling fluid is a complex fluid mixture with a base fluid (water or oil base) with different materials and chemical added to the drilling fluid to meet specific properties (Bourgoyne et al. 2003). The drilling fluid density have to be higher than the pore pressure, to avoid wellbore collapse, and lower than the fracture gradient, to avoid fracturing the wellbore and prevent oil and gas from entering the wellbore. pH is another important property of the drilling fluid, which needs to be considered to prevent corrosion of drilling equipment and prevent chemical instability of shales causes by the drilling fluid. Furthermore, the hydraulic system plays a significant role in drilling operation, where dynamic pressure becomes very crucial for a narrow operating drilling fluid window. With the drilling fluid exhibiting non Newtonian fluid behavior, the viscosity of the drilling fluid is influenced by temperature, pressure, and fluid velocity. Thus, the hydraulic system of the drilling fluid is modeled with different models such as Bingham Plastic, Power Law, and Herschel Bulkley fluid models. This chapter investigates the effect of drilling hydraulics and dynamic pressure on drill stem vibrations.

In this chapter, the drill stem was modeled as Euler-Bernoulli beam and discretized using the finite element formulation. The effect of dynamic pressure was included by considering the fluid structure interaction with the drill stem. Two fluid models, Herschel Bulkley and Power Law, were used to determine the uncoupled dynamic pressure drop across the drill stem in the model formulation.

4.1. INTRODUCTION

As the energy demand keeps increasing by 1%, the oil and gas fuel still remains the number one energy contributor, with oil being number one followed by natural gas as of 2014 (Budley, 2015). To extract oil and gas out of the ground, a well is drilled into the subsurface with a rotating drill bit crushing the rock into fragments (cuttings). The drill bit is connected to the surface with steel pipes known as the drill stem (Figure 4.1), where the

drill stem transmit torque to the drill bit. The drilling fluid is pumped down through the drill stem traveling through the drill pipe and the bottom hole assembly (Figure 4.1), the drilling fluid leaves the drill stem through the nozzles located at the drill bit traveling through the annulus lifting rock fragments out of the wellbore.

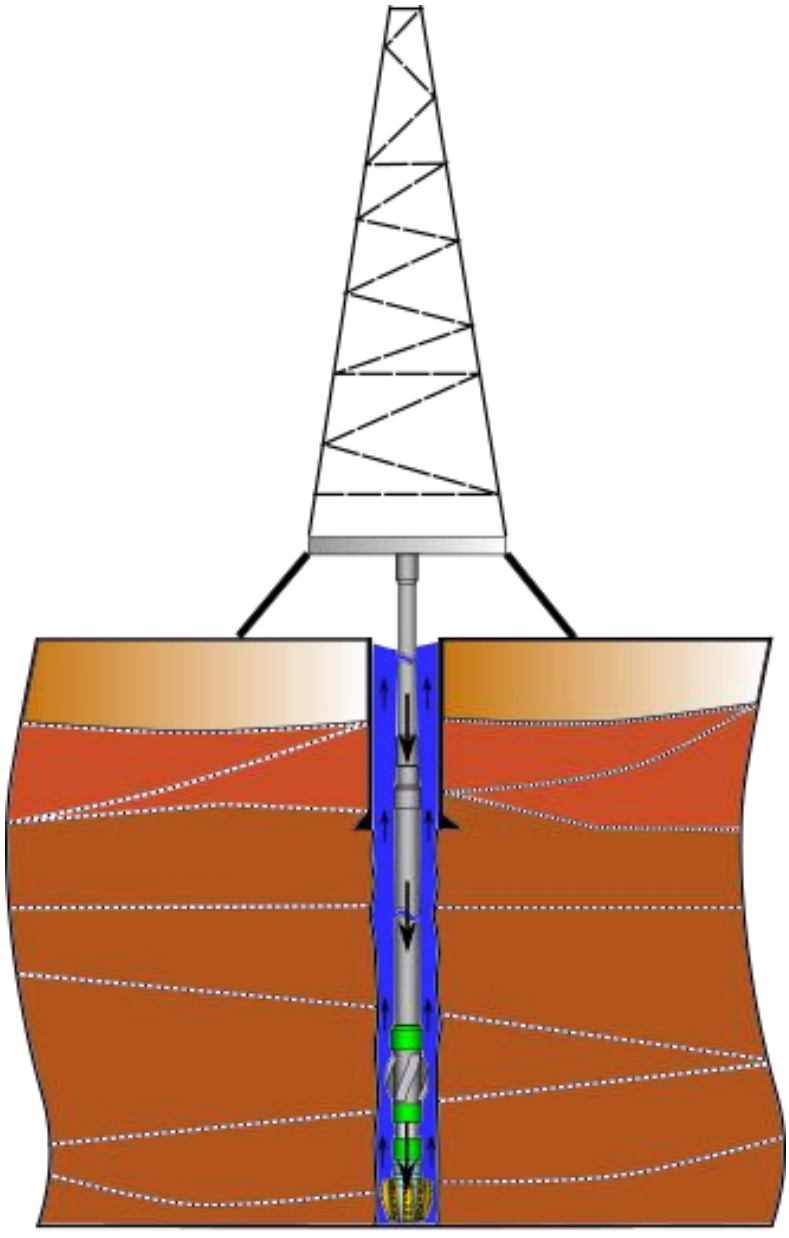

Figure 4.1. Drilling Assembly and Drilling Fluid Circulation System As the Drilling Fluid Travels Through the Drill Stem and Back to the Surface Through the Annulus

Two methods have been used to simulate the effect of drilling fluid on drill stem vibrations. The first method treats the fluid as an added mass that uses the net effective density of the drill stem when submerged in drilling fluid (Payne, 1992; Chen and Geradin, 1994; Yigit and Christoforou, 1998; Sahebkar et al. 2011). In other words the drilling fluid density is subtracted from the steel density of the drill stem to give a net effective density equal to the buoyant weight. The forces exerted by the fluid on the drill stem were studied by Leine et al. 2002, however, the influence of the drilling fluid flowing downward inside the drill pipe and upward in the annulus while circulation was not considered.

The drilling fluid forces acting inside and outside the drill stem were addressed in Paidoussis et al. (2007) and Ritto et al. (2009a). The models that included the fluid interaction assumes the fluid flows axially with constant flow velocity, the fluid inside the drill stem to be inviscid and the fluid in the annulus to be viscous. However, the effect of dynamic pressures including the fluid frictional forces on the drill stem was not address.

The objective of this chapter is to address the effect of dynamic pressure on drill stem vibrations, taking into account the frictional fluid force using two fluid rheological models.

4.2. MODEL FORMULATION

The fluid model presented by Paidoussis et al. (2008) and modified by Ritto et al. (2009a) is extended to include the dynamic and frictional pressure using two fluid models. The main assumptions made in the fluid formulation are as follows:

- The drill stem is concentric
- The drill stem rotation effect on drilling fluid is neglected
- The drilling fluid is incompressible, steady and isothermal with constant axial velocity across each drill stem element
- The flow in the annulus is approximated as a flow through a narrow slot, where the slot width is $\pi\ D_w + OD$ and a gap of $e = D_w - OD$

4.2.1. Fluid Interaction with the Drill Stem. The forces acting on an element of the drill stem due to external and internal axially flowing fluid are shown in Figure 4.2.

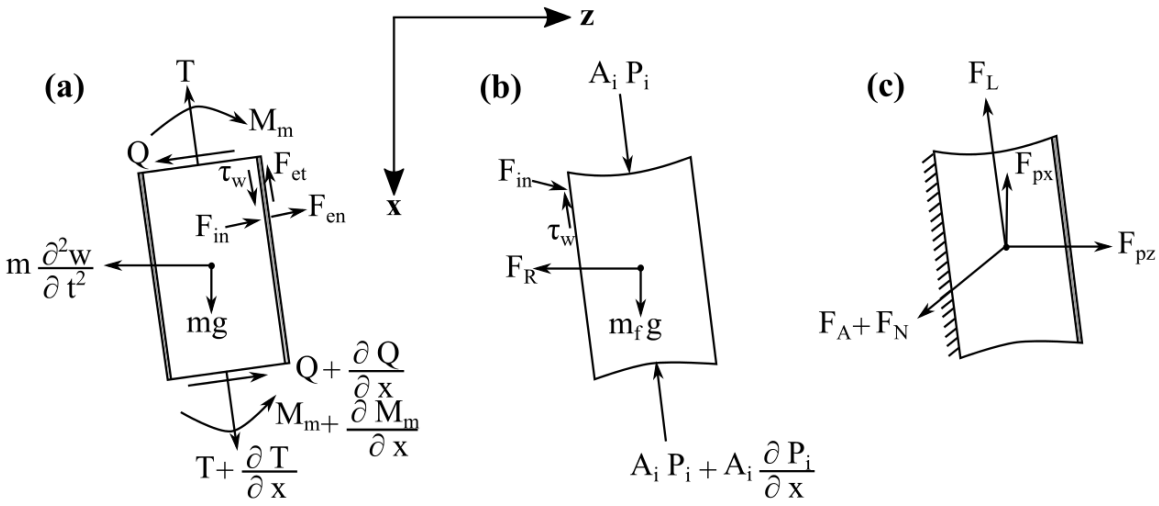

Figure 4.2. Forces Acting on Drill Pipe Element, Inside and Outside Fluid Element Forces

Where T is longitudinal tension, Q is the transverse shear stress, M_m is the bending moment, m is the mass of the drill stem, m_f is the mass per unit length of the fluid, τ_w is the tangential force due to inlet flow (shear stress), F_{in} is the normal force due to inlet flow, F_R is the rate of change of fluid momentum, F_{pz} is the lateral force due to outside pressure, F_{px} is the axial force due to outside pressure, F_A is the lateral hydrodynamic force, F_N, F_L are the frictional force due to the outside flow, and F_{et}, F_{en} are the normal and tangential hydrodynamic force due to external flow.

By summing the forces acting on the pipe element in the x-direction, the drill pipe axial motion can be written as:

$$\frac{\partial T}{\partial x} - \frac{\partial}{\partial x}\left(Q\frac{\partial w}{\partial x}\right) + m\ g + \tau_w + F_{in}\frac{\partial w}{\partial x} - F_{et} - F_{en}\frac{\partial w}{\partial x} = 0 \tag{64}$$

Where the transverse shear is defined using Euler assumptions as:

$$Q = -\frac{\partial}{\partial x}\left(EI\frac{\partial^2 w}{\partial x^2}\right) \tag{65}$$

Where, E is the Young Modulus and I is the moment of inertial. The sum of forces acting on the inside and the outside of the fluid element in the x-direction are respectively:

$$\tau_w - F_{in}\frac{\partial w}{\partial x} = m_f - A_i\frac{\partial P_i}{\partial x} \tag{66}$$

$$-F_{et} - F_{en}\frac{\partial w}{\partial x} = -F_L + F_{px} \tag{67}$$

Where;

$$F_{px} = -\frac{\partial\ A_o P_o}{\partial x} + A_o\frac{\partial P_o}{\partial x} \tag{68}$$

Where A_i and A_o represent the inside and outside area, respectively. Substituting Equation 68 in Equation 67 then into Equation 64, followed by substituting Equation 66 and Equation 65 into Equation 64, produces the coupled axial fluid interaction motion of the drill stem written as:

$$\frac{\partial T}{\partial x} - \frac{\partial^2}{\partial x^2}\left(EI\frac{\partial^2 w}{\partial x^2}\right) + m\ g + m_f g - A_i\frac{\partial P_i}{\partial x} - F_L - \frac{\partial\ A_o P_o}{\partial x} + A_o\frac{\partial P_o}{\partial x} = 0 \tag{69}$$

Thus, the equation of the axial fluid motion is:

$$F_{fx} = m_f\ g - A_i\frac{\partial P_i}{\partial x} - F_L \tag{70}$$

Summing the forces acting on the drill stem element in the z-direction yields:

$$\frac{\partial Q}{\partial x} - m\frac{\partial^2 w}{\partial t^2} + \frac{\partial}{\partial x}\left(T\frac{\partial w}{\partial x}\right) + F_{in} + F_{en} + \tau_w\frac{\partial w}{\partial x} - F_{et}\frac{\partial w}{\partial x} = 0 \tag{71}$$

And summing the forces in the z-direction acting on the inside of the fluid element gives:

$$-F_{in} - \tau_w \frac{\partial w}{\partial x} = F_R + A_i \frac{\partial}{\partial x}\left(P_i \frac{\partial w}{\partial x}\right) \tag{72}$$

To find the rate of change of fluid momentum F_R, the fluid velocity is assumed to be a plug flow with constant axial velocity, where the flow is incompressible. The velocity of the fluid is expressed as:

$$V_f = \frac{D\ r}{D\ t} \tag{73}$$

Where the position vector r is expressed in Cartesian coordinates in term of displacement as:

$$r = u\ \imath + v\ \jmath + w\ k \tag{74}$$

The material derivation in Equation 73 has two components (Modarres-Sadeghi et al. 2006), where the first component is due to the drill stem motion as it vibrates, and the second component is due to fluid flow velocity. Thus, the material derivative can be rewritten as:

$$\frac{D\ r}{D\ t} = \frac{\partial r}{\partial t} + U_i e_t \tag{75}$$

Where, U_i is the mean inlet axial velocity, and e_t is the unit vector tangential to the drill stem motion expressed as:

$$e_t = \frac{\partial r}{\partial x} \tag{76}$$

Thus, the fluid velocity is written as:

$$V_f = U\ \imath + \left(\frac{\partial v}{\partial t} + U_i \frac{\partial v}{\partial x}\right) \jmath + \left(\frac{\partial w}{\partial t} + U_i \frac{\partial w}{\partial x}\right) k \tag{77}$$

Using the velocity in the z -direction from Equation 77 , the rate of change of fluid moment F_R is obtained as:

$$F_R = m_f\ a_{fz} = m_f \left[\frac{\partial w}{\partial t} + U_i \frac{\partial w}{\partial x}\right]^2 \tag{78}$$

Substituting Equation 78 into Equation 72, the sum of forces in the z-direction of the inside fluid element becomes:

$$-F_{in} - \tau_w \frac{\partial w}{\partial x} = m_f \left[\frac{\partial w}{\partial t} + U_i \frac{\partial w}{\partial x}\right]^2 + A_i \frac{\partial}{\partial x}\left(P_i \frac{\partial w}{\partial x}\right) \tag{79}$$

The sum of forces in the z-direction of the outside fluid element yields:

$$-F_{en} + F_{et} \frac{\partial w}{\partial x} = F_A - F_{pz} + F_N + F_L \frac{\partial w}{\partial x} \tag{80}$$

The hydrodynamic force per unit length F_A is equal and opposite to the rate of change of fluid moment (Paidoussis and Besancon, 1981) and it's expressed as:

$$F_A = \chi \left(\frac{\partial}{\partial t} - U_o \frac{\partial}{\partial x}\right) \left[\rho_f A_o \left(\frac{\partial w}{\partial t} - U_o \frac{\partial w}{\partial x}\right)\right] \tag{81}$$

Where, U_o is the outside flow velocity, ρ_f is the fluid density, and χ is a confinement parameter that's always equal or less than 1 and it's defined as:

$$\chi = \frac{D_w^2 + OD^2}{D_w^2 - OD^2} \tag{82}$$

The total fluid force due to the outside pressure F_{pz} is equal to (Paidoussis and Besancon, 1981):

$$F_{pz} = A_o \frac{\partial}{\partial x}\left(P_o \frac{\partial w}{\partial x}\right) \tag{83}$$

By substituting Equations 79-83 and Equation 65 into Equation 71 , the equation of the coupled drill stem motion in the transverse direction is obtained as:

$$\begin{aligned} &\frac{\partial^2}{\partial x^2}\left(EI\frac{\partial^2 w}{\partial x^2}\right) + m\frac{\partial^2 w}{\partial t^2} - \frac{\partial}{\partial x}\left(T\frac{\partial w}{\partial x}\right) + m_f\left[\frac{\partial w}{\partial t} + U_i\frac{\partial w}{\partial x}\right]^2 \\ &+ A_i\frac{\partial}{\partial x}\left(P_i\frac{\partial w}{\partial x}\right) + \chi\left(\frac{\partial}{\partial t} - U_o\frac{\partial}{\partial x}\right)\left[\rho_f A_o\left(\frac{\partial w}{\partial t} - U_o\frac{\partial w}{\partial x}\right)\right] \\ &- A_o\frac{\partial}{\partial x}\left(P_o\frac{\partial w}{\partial x}\right) + F_N + F_L\frac{\partial w}{\partial x} = 0 \end{aligned} \tag{84}$$

Thus, the transverse equation of fluid motion in the z-direction is:

$$\begin{aligned} F_{zf} = {} & m_f\left[\frac{\partial w}{\partial t} + U_i\frac{\partial w}{\partial x}\right]^2 + \chi\left(\frac{\partial}{\partial t} - U_o\frac{\partial}{\partial x}\right)\left[\rho_f A_o\left(\frac{\partial w}{\partial t} - U_o\frac{\partial w}{\partial x}\right)\right] \\ &+ A_i\frac{\partial}{\partial x}\left(P_i\frac{\partial w}{\partial x}\right) - A_o\frac{\partial}{\partial x}\left(P_o\frac{\partial w}{\partial x}\right) + F_N + F_L\frac{\partial w}{\partial x} \end{aligned} \tag{85}$$

The pressure inside the drill stem is assumed to be the hydrostatic pressure, which is linearly varying with depth, plus the applied pump pressure P_{pump} written as:

$$P_i = \rho_f g x + P_{pump} \tag{86}$$

The outside pressure is obtained by balancing the forces of the system shown in Figure 4.3.

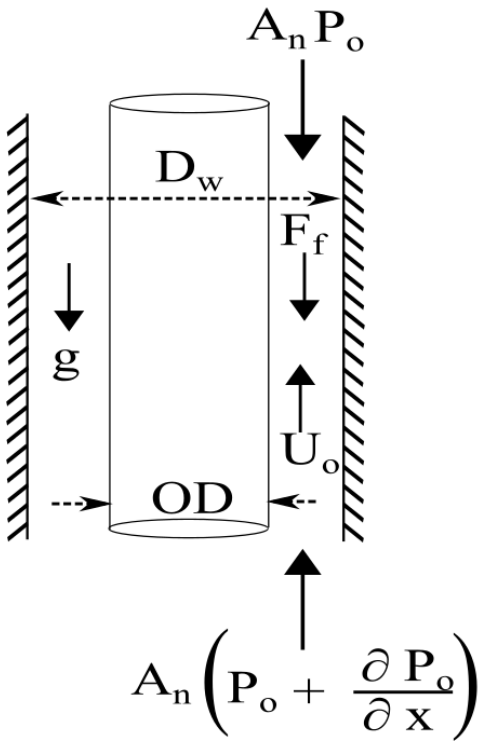

Figure 4.3 Fluid Forces in the Annulus

Where, A_n is the outside flow area (annulus area), which is defined as:

$$A_n = \frac{\pi}{4} \; D_w^2 - OD^2 \tag{87}$$

The force balance of the system shown in Figure 4.3 yields:

$$F_f + \rho_f \; g \; A_n - A_n \frac{\partial P_o}{\partial x} = 0 \tag{88}$$

The frictional force F_f is defined according to Rinaldi and Paidoussis, (2012) as:

$$F_f + \rho_f \; g \; A_n - A_n \frac{\partial P_o}{\partial x} = 0 \tag{89}$$

Where, S_{tw} is the total wetted surface area per unit length defined as $S_{tw} = \pi D_w + \pi OD$, and S_o is the total area per unit length of the drill stem written as $S_o = \pi OD$. Substituting Equation 89 into Equation 88 and integrating over the area gives the outside pressure expression as:

$$P_o A_n = \left[F_L \left(\frac{S_{tw}}{S_o} \right) + \rho_f \; g \; A_n \right] x \tag{90}$$

Following Paidoussis, (1975), the frictional viscous forces per unit length are defined as:

$$F_L = A_o P_{Dyn} \tag{91}$$

$$F_N = P_{Dyn} \frac{A_o}{U_o} \left(\frac{\partial w}{\partial t} + U_o \frac{\partial w}{\partial x} \right) \tag{92}$$

Where, P_{Dyn} is the dynamic pressure including the pressure losses over each element. The dynamic pressure is obtained from hydraulic pressure drop analysis, which is discussed in the next section.

The fluid forces in the y-direction are obtained using the same approach as for the z-direction.

4.2.2. Fluid Rheology Models. Power Law and Herschel Bulkley are widely used to characterize the rheology of the drilling fluid (Ahmed and Miska, 2008; Kelessidis et al. 2006). The shear rate and shear stress behavior of both models are similar (Figure 4.4), where the difference between the two models is the yield point in Herschel Bulkley model.

To determine the fluid characteristic of power law fluid model, only two parameters are need (n, k) while for the Herschel Bulkley model three parameters are needed (n, k, τ_y).

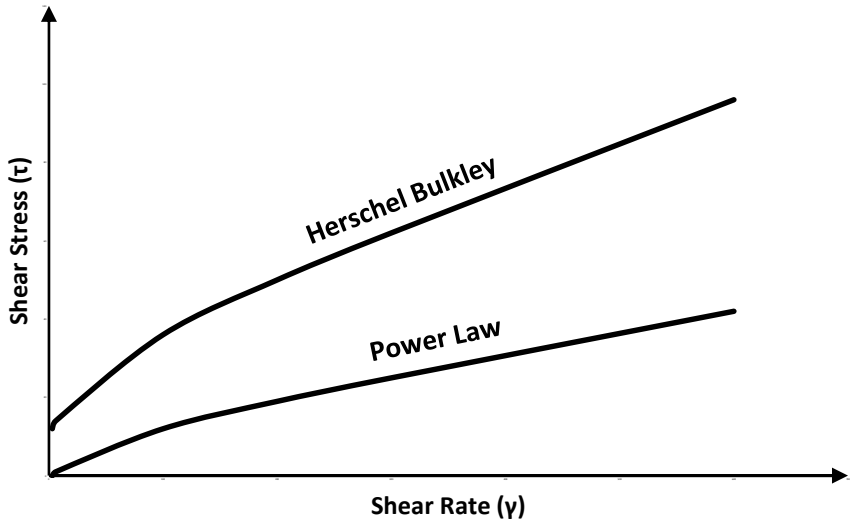

Figure 4.4 Behavior of Herschel Bulkley and Power Law Fluid Models

The Power Law model defines the fluid rheology as:

$$\tau = k\gamma^n \tag{93}$$

Where, τ is the shear stress, k is consistency index, and n is the flow behavior index. The fluid consistency index (k) and the flow behavior index (n) are found graphically using the viscometer readings.

The Herschel Bulkley model defines the fluid characteristic as:

$$\tau = \tau_0 + k\gamma^n \tag{94}$$

Where τ_0 is the yield point. To obtain the yield point τ_0, the procedure introduced by Verson and Togla (2005) and used by Ochoa (2006) is followed, where the yield point is calculated as:

$$\tau_0 = \frac{\tau_m^2 - \tau_{min}\,\tau_{max}}{2\tau_m - \tau_{min} - \tau_{max}} \tag{95}$$

Where, τ_m is the shear stress corresponding to the geometric mean shear rate (γ_m), where γ_m is defined as:

$$\gamma_m = \sqrt{\gamma_{min}\gamma_{max}} \tag{96}$$

With the use of the mean shear rate (γ_m), the mean shear stress (τ_m) is interpolated to obtain the yield point (τ_0). The parameters n and k are obtained graphically by plotting $log\ \tau - \tau_0$ versus the shear rate γ of the viscometer reading.

The equations presented by Merlo et al. (1995), was used to obtain the pressure drop across the drill pipe, drill collar, drill bit, drill collar annulus, and drill pipe annulus for the Herschel Bulkley model. The pressure drop was calculated for the Power Law model flowing Ochoa, (2006). The total pump pressure is then obtained (using both models) as the total pressure drop across the system as:

$$P_{pump} = \left(\frac{dP_D}{dL}\right)_{inside} + \left(\frac{dP_D}{dL}\right)_{outside} + \left(\frac{dP_D}{dL}\right)_{bit} \tag{97}$$

The P_{pump} in Equation 86 is obtained using the total pump pressure obtained in Equation 97 plus the hydrostatic pressure subtracted the pressure drop across each element:

$$P_{pump}\ i\ = Pump - \left(\frac{dP_D\ i}{dL}\right) \tag{98}$$

And the P_{Dyn} (in Equation 91 and Equation 92) is obtained the same way where P_{Dyn} is the pressure drop in the annulus.

The pressure drop across the bit (ΔP_b) is calculated bases on the flow area the bit across the nozzles as: (Bourgoyne et al. 2003)

$$\Delta P_b = \frac{\rho_f\ Q_f^2}{2\ C_d^2 A_t^2} \tag{99}$$

Where, Q_f is the fluid flow rate, C_d is fluid discharged coefficient, and A_t is the total flow area (total flow area of the nozzles). Matlab® scripts used for both fluid models are located in Appendix F.

Using the finite element formulation, the fluid equations and force are discretized and written in term of displacements. The displacements in discretized form are expressed as:

$$\begin{aligned} u_e\ \zeta,t\ &= N_u\ \zeta\ q_e\ t \qquad & v_e\ \zeta,t\ &= N_v\ \zeta\ q_e\ t \\ w_e\ \zeta,t\ &= N_w\ \zeta\ q_e\ t \qquad & \theta_e\ \zeta,t\ &= N_\theta\ \zeta\ q_e\ t \end{aligned} \tag{100}$$

Where N_i is the shape function corresponding to each degree of freedom, ζ is the dimensionless length $\frac{x}{l_e}$, and q_e is the vector of nodal displacement of two node element expressed as:

$$q_e = [u_1 \quad v_1 \quad v'_1 \quad w_1 \quad w'_1 \quad \theta_1 \quad u_2 \quad v_2 \quad v'_2 \quad w_2 \quad w'_2 \quad \theta_2]^T \tag{101}$$

Discretizing the fluid forces in the x-direction yields, the fluid axial force written in discretized form as:

$$f_{f_e} = \int_0^L \left[\left(m_f g - A_i \right) \frac{\partial P_i}{\partial x} - \frac{1}{2} C_f \rho_f D_o U_o^2 \right) N_u^T l_e \Big] d\zeta \tag{102}$$

The fluid equation of motion in the z and y direction after discretization yields the mass, stiffness and damping matrix written as:

$$M_{f_e} = \int_0^1 \left[(m_f + \chi \rho_f A_0)\ N_w^T N_w + N_v^T N_v\ l_e \right] d\zeta \tag{103}$$

$$K_{f_e} = \int_0^1 (-m_f U_i^2 - A_i P_i + A_o P_o - \chi \rho_f A_o U_o^2)[N'^T_w N'_w + N'^T_v N'_v] \frac{1}{l_e} d\zeta + \int_0^1 \left(-A_i \frac{\partial P_i}{\partial x} + A_o \frac{\partial P_o}{\partial x}\right) \left[N^T_{\theta_y} N_{\theta_y} + N^T_{\theta_z} N_{\theta_z}\right] l_e d\zeta \tag{104}$$

$$C_{f_e} = \int_0^1 (-2U_o \chi \rho_f A_o - 2m_f U_i) l_e [N'^T_w N'_w + N'^T_v N'_v] d\zeta - \int_0^1 2A_o P_{Dyn} l_e [N^T_w N_w + N^T_v N_v] d\zeta \tag{105}$$

4.2.3. Drill Stem Model and the Equation of Motion. The drill stem was modeled as rotating cylinder with two node element where each node has six degree of freedom. Detailed derivation of equation of motion is given in [Chapter 2 starting from page 18]. The final equation of motion including the fluid forces effect is:

$$([M] + [M_f])x + ([C_f] + [C] + [G])x + [K] + [K_G] + [K_F]\ x = f_g + f_f + f_r \tag{106}$$

Where $[M]$ is the drill stem mass matrix, $[M_f]$ is the fluid mass matrix, $[C]$ is the structural damping matrix, $[C_f]$ is the fluid damping matrix, $[G]$ is the gyroscopic matrix, $[K]$ is the drill stem stiffness matrix, $[K_G]$ is the geometric stiffness matrix, $[K_f]$ fluid stiffness matrix, f_g is the gravity force vector, F_f is the fluid force, and f_r is the reaction force at the bit.

4.3. RESULTS

The natural frequency and mode shape of the drill stem was obtained for the case with no fluid, the approach used by Ritto et al. (2009a) (named as the Reference Model

herein), dynamic pressure using Herschel Bulkley (HB) and dynamic pressure using Power Law (PL) model. Table 4.1 shows the drill stem configuration and properties used to compute the natural frequencies and mode shapes for the four different scenarios.

Table 4.1. Model Input Parameters

Component	Length (m)	OD (m)	ID (m)
Drill pipe	1500	0.127	0.109
Drill pipe element length	50	-	-
Drill collar	200	0.216	0.054
Drill collar element length	10	-	-
Borehole	1700	0.3	-
Casing	900	-	0.445
Stabilizer Location	1650	Fixed Boundary	
Properties			
ρ	7850	$Kg.\,m^{-3}$	
ρ_f	1298	$Kg.\,m^{-3}$	
C_f	0.0125	(-)	
Q_f	0.04	$m^3.\,s^{-1}$	
E	2.1X10^11	Pa	
Drill bit nozzle sizes	3X18	1/32 inches	
υ	0.29	(-)	
Ω_x	10	$rad.\,s^{-1}$	
Axial load	100	KN	
Viscometer Readings			
3 RPM	8	°	
6 RPM	10	°	
100 RPM	32	°	
200 RPM	46	°	
300 RPM	58	°	
600 RPM	92	°	

The first ten lateral natural frequencies of the four scenarios are shown in Figure 4.5. Where, HB in Figure 4.5 stands for Herschel Bulkley fluid model, PL stands for the Power Law model and Ref. Model stands the reference model from Ritto et al. (2009a).

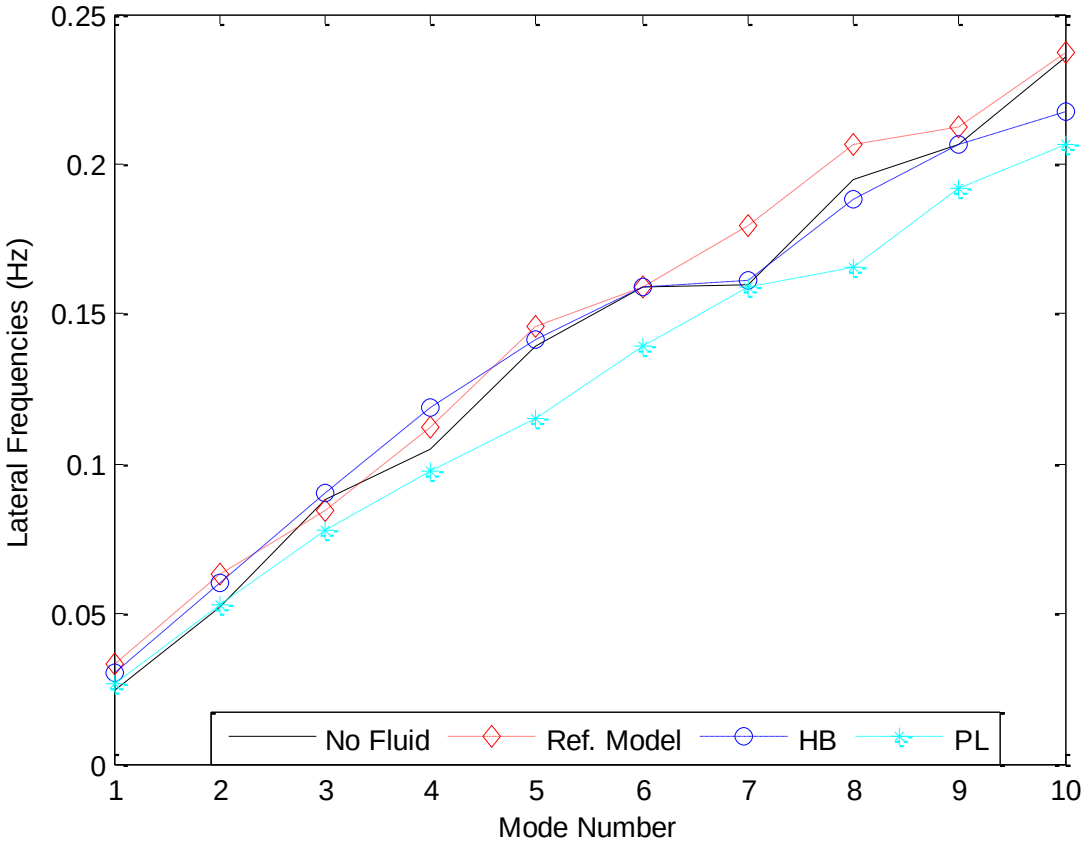

Figure 4.5. First Ten Natural Frequencies for the Four Scenarios, No Fluid, Reference Model (Ref. Model), Herschel Bulkley (HB), and Power Law Models (PL)

The first ten axial and torsional natural frequencies of the four cases are similar, however, lateral frequencies differ. The difference in natural frequencies with and without fluid can be seen in Figure 4.5, the average difference, considering the first ten modes, ranges from 8 to 11% for the three cases including fluid. When including the dynamic pressure, the average difference with the reference model is 6% using Herschel Bulkley and 18% using the Power Law model.

If the pressure drop at the bit using the dynamic pressure for both fluid models is neglected, the first ten natural frequencies obtained with the use of Herschel Bulkley and Power Law models will follow the reference model results, with an average difference of less than 1% for the first ten modes.

Figure 4.6 shows the first three normalized mode shapes of the four cases for the lateral direction.

Including the fluid structure interaction has a big impact on lateral mode shapes (Figure 4.6). The mode shape including the fluid forces for the three cases are similar with small change in amplitude especially at higher mode (mode three in Figure 4.6).

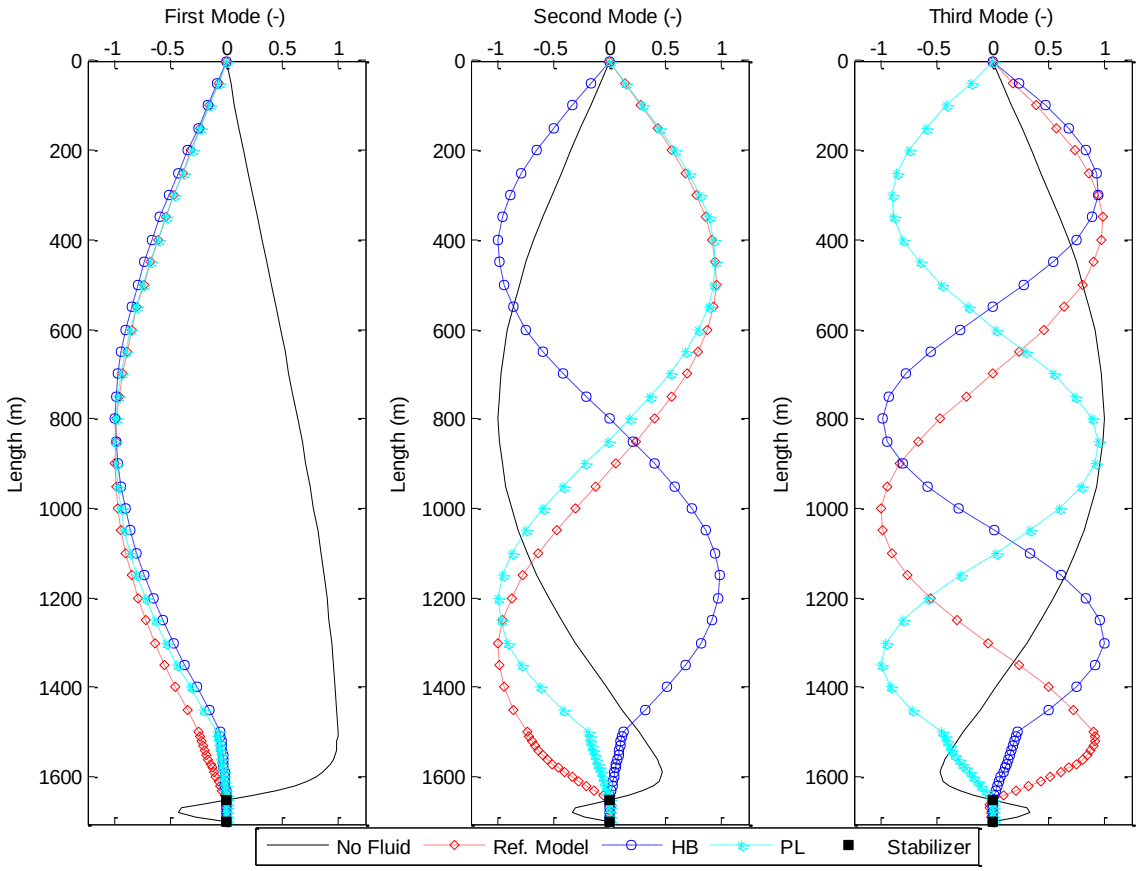

Figure 4.6. First Three Lateral Mode Shape for the Four Scenarios No Fluid, Reference Model (Ref. Model), Herschel Bulkley (HB), and Power Law Models (PL)

The effect of drilling fluid density on the drill stem natural frequencies is addressed in Figure 4.7, using the reference model, Herschel Bulkley and Power Law models.

Using the reference model, the change in lateral frequencies was less than 9%, however, when using the dynamic pressure, the reduction in lateral frequencies is higher (24% and 28% for Herschel Bulkley and Power Law models respectively). Lateral

frequencies of the three cases have the same behavior (Figure 4.7), as fluid density increases lateral frequencies decreases.

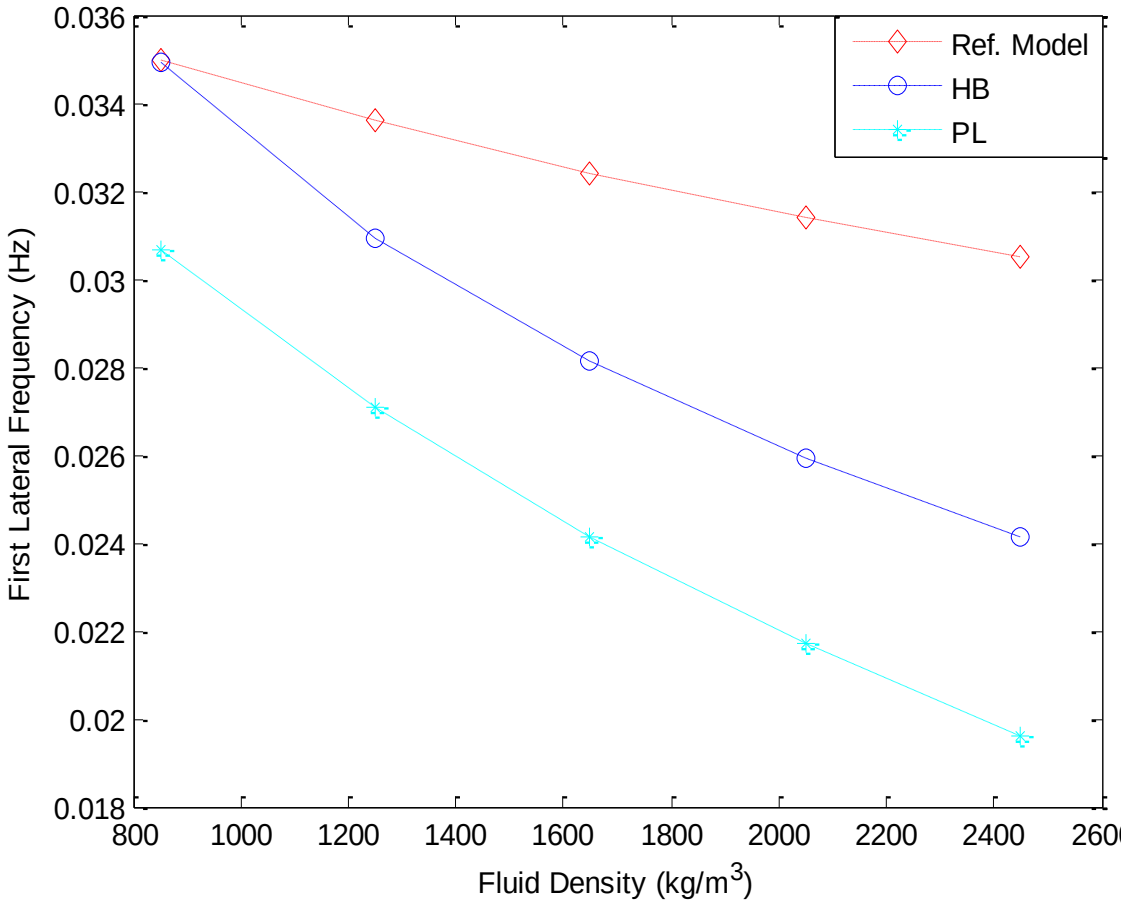

Figure 4.7. Effect of Drilling Fluid Density on Lateral Frequencies for the Three Scenarios

The mode shape of the three scenarios have the same behaves under different fluid densities. Figure 4.8 shows the first three mode shape obtained from the reference model as fluid density increases.

In Figure 4.8, slit change in mode shape amplitude as density increases can be seen for the first mode shape. However, at higher modes, mode shapes amplitude changes as density increases.

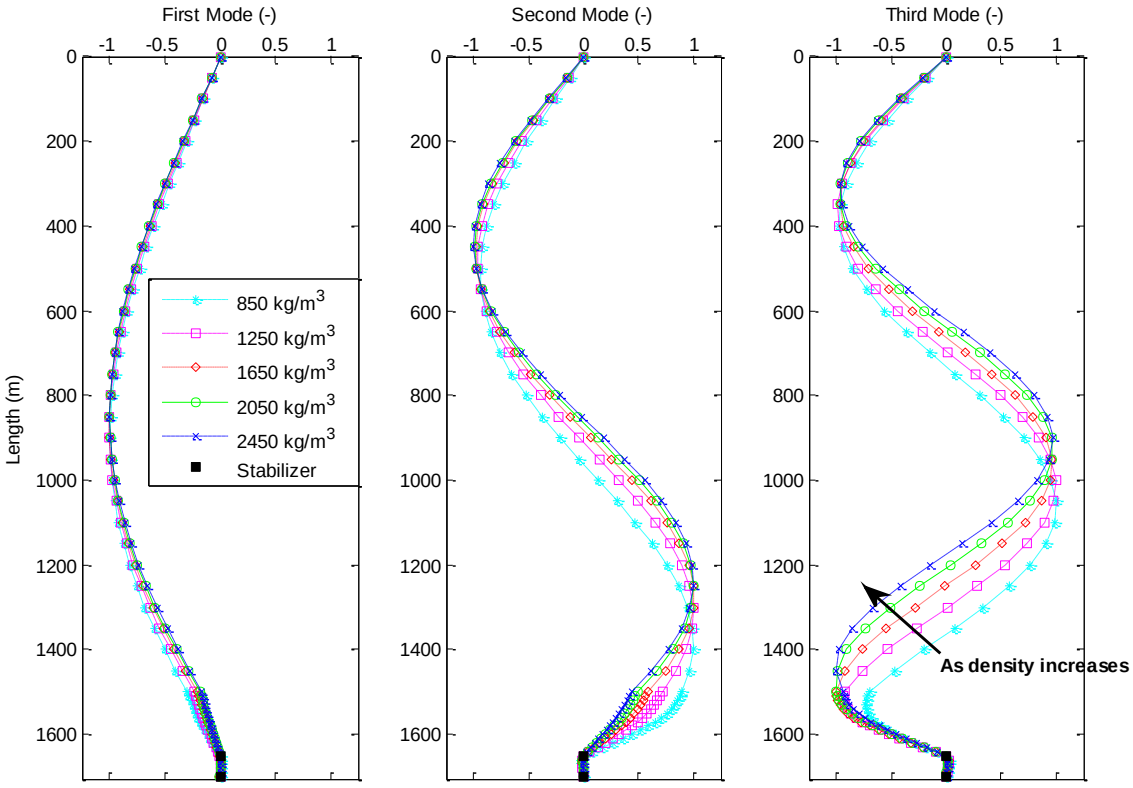

Figure 4.8. First Three Mode Shapes for Different Fluid Densities for the Reference Model

The effects of increasing the flow rate on lateral frequency using the three cases are shown in Figure 4.9. Axial and torsional frequencies had an unnoticeable change (less than 1%) under the chosen flow rates.

As the flow rate increases, no significant change (less than 1%) in lateral frequencies for the reference model scenario is observed. Lateral frequency decreases as the flow rate increase with the use of Herschel Bulkley and Power Law models. The average different in lateral frequency for the first ten modes using the Herschel Bulkley model is 65% decreases. For the Power Law model, the natural frequency becomes unstable, with complex frequencies, at a flow rate of 0.057 $m^3.s^{-1}$ (900 $gal.min^{-1}$). The average decrease in lateral frequency for the first ten modes for the Power Law is 25%.

As only small change (less than 1%) in lateral frequencies using the reference model, lateral mode shape does not change as the flow rate increases. However, the lateral mode shapes changes using the dynamic pressure (Figure 4.10).

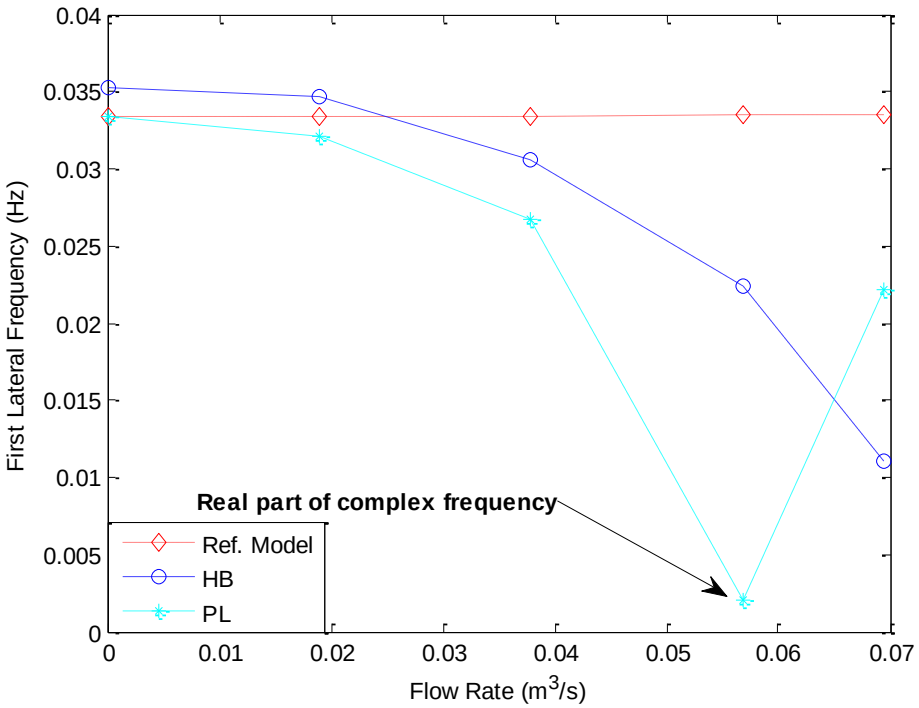

Figure 4.9. Lateral Frequencies as Increasing the Flow Rate using the Three Scenarios

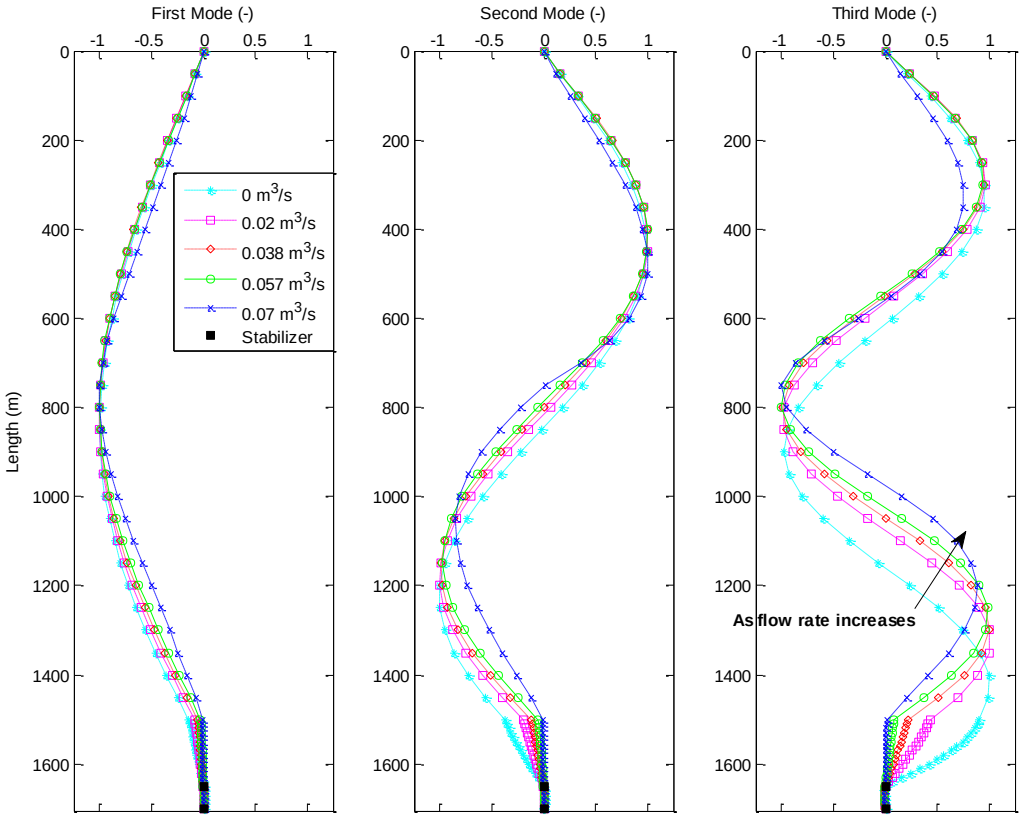

Figure 4.10. Effect of Flow Rate on Later Mode Shape using Herschel Bulkley Model

Comparing Figure 4.10 and Figure 4.8, it seems that increasing the fluid flow rate have similar impact on lateral mode shape as increasing the fluid density. The mode shape of the Power Law model follows the same trend as the Herschel Bulkley model except with higher deflection as fluid reaches 0.057 $m^3.s^{-1}$ (900 $gal.min^{-1}$).

The viscosity effect on natural frequencies is addressed by using the plastic viscosity as the viscosity measurement. The plastic viscosity is calculated based on viscometer reading as: (Fann, 2015)

$$\begin{aligned} \mu_p \ cp &= \theta_{600} - \theta_{300} \\ \mu_p \ Pa &= 10^{-3} \times \ \theta_{600} - \theta_{300} \end{aligned} \tag{107}$$

Figure 4.11 shows the effect of fluid viscosity on lateral frequencies of Herschel Bulkley and Power Law models.

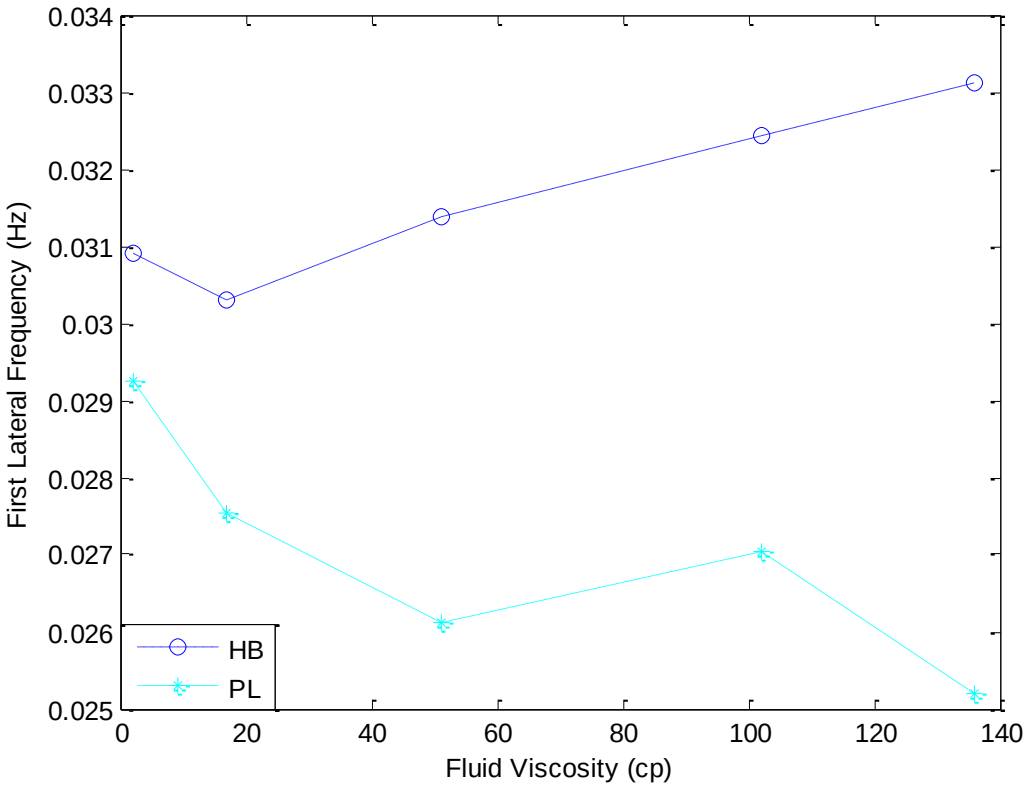

Figure 4.11. Lateral Frequency as a Function Fluid Viscosity using Herschel Bulkley and Power Law Fluid Models

When including the dynamic pressure, lateral frequency, using Herschel Bulkley fluid model, decreases with fluid plastic viscosity going from 2 -17 cp, however, going from 17 cp up to 136 cp lateral frequencies increases. For the Power Law model, lateral frequencies behaves differently while increasing the fluid viscosity, but an overall trends shows lateral frequencies decreases with increasing fluid viscosity (Figure 4.11). Fluid viscosity have an average effect on lateral frequency of approximately 11% using Herschel Bulkley model and 9% using the Power Law model when considering the first 10 natural frequencies.

The largest effect of viscosity on lateral mode shape was using Herschel Bulkley model (Figure 4.12). The first lateral model shape using the Power Law model follows the same trend as Herschel Bulkley model, however, lateral deflection amplitude as viscosity increases is lower.

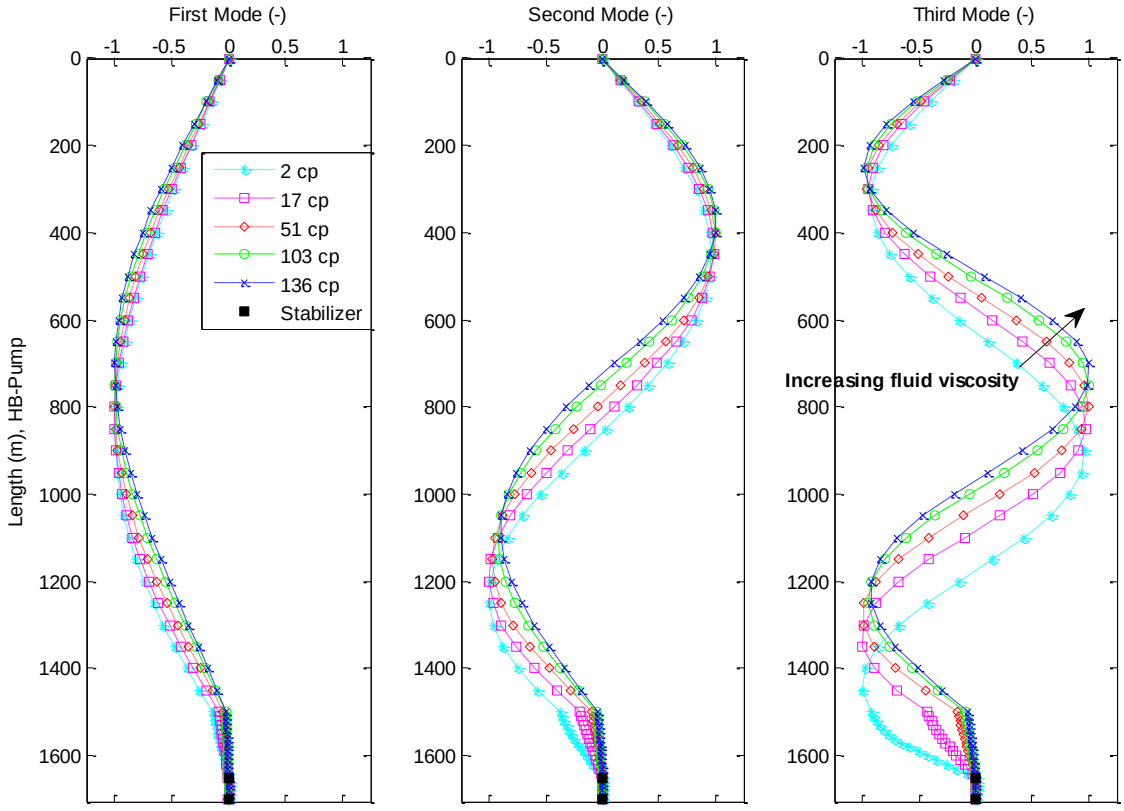

Figure 4.12. Herschel Bulkley Mode Shape as a Function of Fluid Viscosity

The influence of the annulus area (wellbore diameter) is investigated using the three scenarios by varying the wellbore diameter. Figure 4.13 shows the first lateral frequency obtained using the three cases as a function of the wellbore diameter.

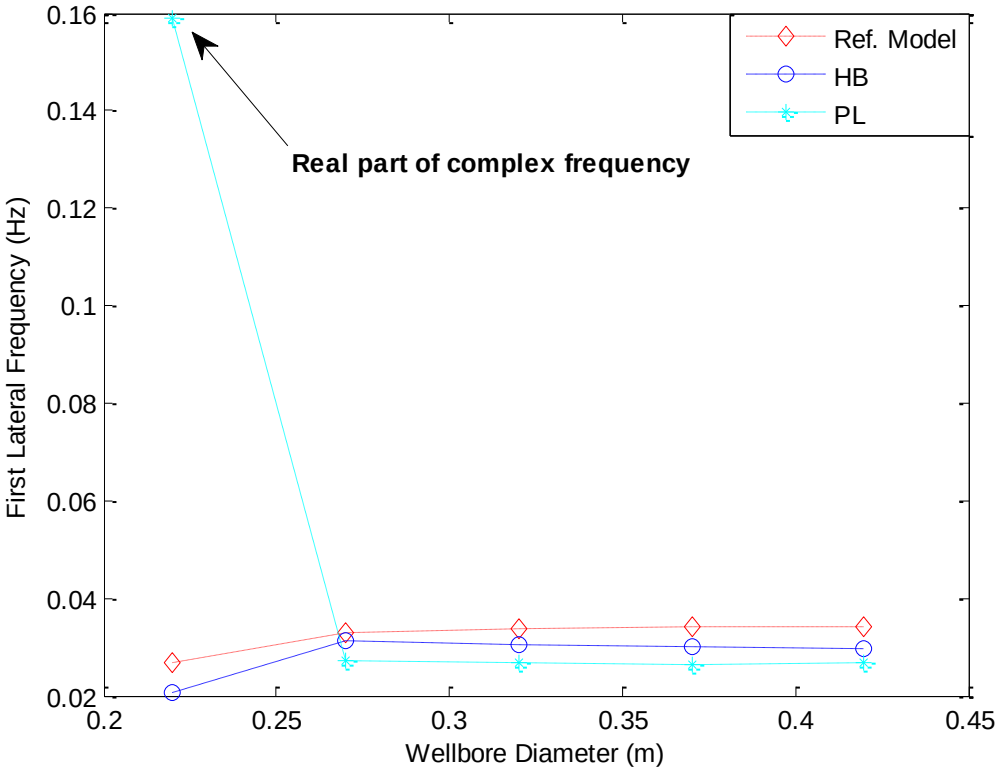

Figure 4.13. First Lateral Frequency of the Five Cases as a Function of Wellbore Diameter

As the ratio of wellbore diameter to outside diameter of the drill stem bottom hole assembly goes higher than 1.25 the influence of fluid on lateral vibration decreases (Figure 4.13). Up to 50% decrease in lateral frequency will occur when the clearance ratio is below 1.25. The highest change in later frequency due to change in wellbore diameter was notice with the use of Power Law model, the lateral frequency at the smallest wellbore diameter produced a complex frequency.

The effect of total flow area of the bit was investigated by varying the nozzle sizes to vary the total flow area at the bit. Figure 4.14 shows the lateral frequency as a function of total flow area for Herschel Bulkley and Power Law fluid models.

At the first point in Figure 4.14, both models had complex lateral frequency. Interestingly, when ignoring the first complex frequency of both models. The total flow area at the bit has the same effect on lateral frequency as the wellbore diameter effect (Figure 4.13), where when exceeding a specific flow area at the bit, the effect of fluid decreases dramatically. The average change in lateral frequency for the first ten modes, excluding the complex frequencies, is 17% using Herschel Bulkley model and 25% using the Power Law model.

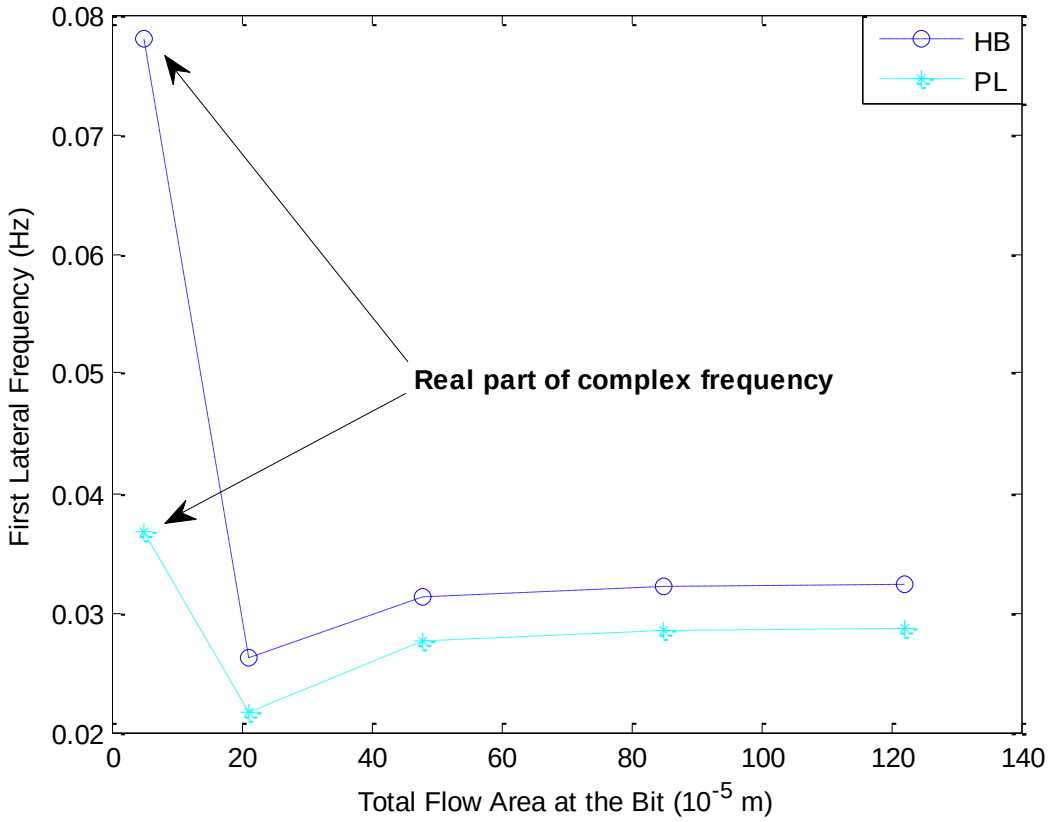

Figure 4.14. Effect of Bit Flow Area on Lateral Frequency

4.4. DISCUSSION

Including fluid structure interaction has no effect on drill stem axial and torsional vibrations of the drill stem, which agrees with the reference model (Ritto et al 2009a). However, lateral vibrations are influenced by the fluid interaction with the drill stem. The

amount of change in lateral vibrations depends strongly on how the fluid forces (mainly the fluid viscous forces) are treated (Figure 4.5). The maximum change in lateral frequencies when including the fluid forces presented in the reference model is 11% compared to the model with no fluid forces. The lateral mode shape of the drill stem completely changes its shape when including the fluid forces effect (Figure 4.6), however, only the deflection amplitude of the mode shape changes when using different fluid models.

When considering the drill stem hydraulics (dynamic pressure), lateral frequencies obtained using both Herschel Bulkley and Power Law fluid models differs from the reference model. This is due to the high differential pressure between the inside and outside flow of the drill stem caused by high frictional pressure loss at the drill bit.

Increasing the fluid density decreases lateral vibrations. Only 9% decrease in lateral vibration is noticed using the reference model formulation, while using the dynamic pressure significantly changes lateral frequencies (Figure 4.7). For the Power Law model, a decrease of 28% of lateral frequency is noticed as the fluid density increases and for the Herschel Bulkley model, a decrease of 24% is observed. The different in lateral frequencies between the Power Law and Herschel Bulkley models is due to the viscous frictional forces.

Ritto et al. (2009a) concluded that the fluid velocity does not have a significant effect on lateral vibrations, however using the dynamic pressure the lateral frequencies are greatly affected (Figure 4.9). The highest decrease on lateral frequencies were obtained using the Power Law fluid model with an average decrease of 25%, also the using the Power Law model at higher flow rate (900 gal/min) causes the drill stem to be unstable as can be notice from the complex frequencies at that flow rate.

For the Power Law model, lateral frequencies behave differently when increasing the fluid viscosity (Figure 4.11). The maximum total change in natural frequency was, using the Herschel Bulkley model, approximately 11% decrease for the first ten natural frequencies.

One of the most significant parameters in the fluid model affecting the drill stem lateral frequencies is the wellbore diameter; where up to 50% decrease in lateral frequencies could occur at a narrow gap. Interestingly, when the ratio of wellbore diameter

to outside diameter of the drill stem is higher than 1.25, no significant changes of lateral frequency will be noticed.

For small nozzle sizes (small flow area through the drill bit), the drill stem becomes unstable. The behavior of lateral frequency results from the nozzle size analysis follows the same behavior of lateral frequencies under varying wellbore diameter. Above a certain flow area through the bit, the effect of flow area on lateral frequencies vanishes.

4.5. SUMMARY

In this chapter, the effect of including the dynamic pressure using two fluid rheological models was addressed and compared to a reference model, which does not include the drilling dynamic pressure. Including fluid structure interaction to the drill stem vibration model have no effect on axial and torsional vibration, however, it does affect lateral frequencies. Under the condition used in the comparison, maximum change in lateral frequencies was observed with the use of the Power Law fluid model (11% changes).

The dynamic pressure using both Herschel Bulkley and Power Law fluid models have a significant impact on lateral frequencies. High flow rate causes the drill stem to be unstable. Also, the wellbore diameter and total flow area at the bit changes the lateral frequencies of the drill stem. Wrong selection of total flow area at the bit (nozzle sizes) could cause the drill stem to be unstable.

5. SELECTING OPTIMUM DRILLING PARAMETERS TAKEN DRILL STEM VIBRATIONS INTO ACCOUNT

To avoid severe vibrations, different drill stem vibration models have been used in the previous chapters to predict and avoid resonance regions by selecting bottom hole assembly components and operating parameters such as weight on bit and RPM. The overall efficiency of the drilling operations is evaluated using either mechanical specific energy model or inverted rate of penetration (ROP) models (Dupriest and Koederitz, 2005; Warren, 1984; Nygaard et al. 2002). This chapter addresses the impact of drill stem vibrations on the overall drilling performance. The object of this chapter is to provide a method to improve drilling efficiency taking drill stem vibrations into account.

In this chapter, a set of data including vibration data is collected from a section of a well drilled in the North Sea to analyze the level of efficiency obtained during drilling the section. Based on the level of efficiency obtained for the drilled section, a new methodology to increase drilling performance while taking the drill stem vibration into account is presented.

5.1. INTRODUCTION

Drilling efficiency is often characterized by the drilling speed (rate of penetration), where the rate of penetration is measured in meters drilled per hour (m/hr). Several parameters contributes towards the overall rate of penetration such as; weight on bit, applied rotational speed, rock strength, drilling hydraulics, and bit wear (Rashidi et al. 2008). Drilling performance could be improved by increasing ROP through ROP models that describes the rate of penetration as a function of drilling and geological parameters. To quantify the drilling performance while drilling, mechanical specific energy is used as a trending tool (Dupriest and William, 2005).

Drill stem vibration have a significant role in selecting operational parameters. To avoid severe vibrations, drill stem vibration models are used to predict the resonance regions to be avoided, which are usually reported as a function of drilled depth. When operating the drill stem at the calculated critical speeds, damages to drill bit and bottom

hole assembly could occur due to the increase in the dynamic stress per cycle caused by the increase in vibration levels.

In this chapter, a methodology to increasing drilling efficiency is presented with the use of ROP model in conjunction with drill stem vibration modelling that provides an operating window (RPM, WOB) with the predicted ROP and location of critical speeds to be avoided. The drilling performance of a section of a well drilled in the North Sea is first analyzed. The collected data is then used to demonstrate and verify the proposed methodology.

5.2. METHODOLOGY

The drill stem model used in this chapter is based on the model developed using the Euler-Bernoulli's assumption (Chapter 2.2) including the dynamic pressure with the use of Herschel Bulkley fluid model (Chapter 4). The final equation of motion used to obtain the critical speeds is:

$$[M]x + [G]x + [K]x = f_g + f_f + f_r \tag{108}$$

Where the mass matrix $[M]$ includes the drill stem mass plus the fluid mass, $[G]$ is the gyroscopic matrix, $[K]$ is the stiffness matrix of the drill stem including geometric stiffness matrix and fluid added stiffness, and f_g, f_f, f_r are the gravity force, the fluid force and the reaction force at the bit (weight on bit) respectively. First, a static analysis is performed to solve for the initial deflection (u_s), to obtain the geometric stiffness:

$$u_s = [K + K_f]^{-1}(f_g + f_f + f_r) \tag{109}$$

The natural frequencies are obtained from the equation of motion (Equation 108) by converting the equation of motion to the state space form. The state space form is formulated by introducing a second order state vector written as:

$$q = [x\ x]^T \tag{110}$$

Substituting Equation 110 in Equation 108 yields:

$$\overline{[M]}q + \overline{[C]}q = \{0\} \tag{111}$$

Where:

$$\overline{[M]} = \begin{bmatrix} [M] & [0] \\ [0] & [I] \end{bmatrix} \tag{112}$$

$$\overline{[C]} = \begin{bmatrix} -[G] & [K] \\ [-I] & [0] \end{bmatrix} \tag{113}$$

Where, $[I]$ in Equation 112 and Equation 113 is the identity matrix. Assuming a solution of the form:

$$q\ t\ = \Phi\ t\ e^{\omega t} \tag{114}$$

Substituting Equitation 114 in Equation 111 yields:

$$\omega\overline{[M]}\ \Phi + \overline{[C]}\ \Phi = \{0\} \tag{115}$$

Equation 115 is the reduced Eigenvalue problem, which could be written in a more compact form as:

$$[A]\Phi = \omega\ \Phi \tag{116}$$

Where:

$$[A] = \begin{bmatrix} -\overline{[M]}^{-1}[-G] & -\overline{[M]}^{-1}[K] \\ [I] & [0] \end{bmatrix} \tag{117}$$

Where, ω in Equation 116 is the complex Eigenvalues vector that composes of a real and imaginary component. The imaginary component of the Eigenvalue corresponds to the drill stem natural frequencies, while the real part provides information regarding the system stability.

The effect of alternating geology on the drilling performance was taken into account using the unconfined compressive strength (UCS). The UCS was calculated using the acoustic velocities obtained from logs as (Hareland and Nygaard, 2007b):

$$UCS = \left(\frac{1}{k_1\ \Delta t_c - k_2}\right) + k_3 \tag{118}$$

Where UCS in Equation 118 reads MPa, k_1, k_2 and k_3 are constants depends on lithology and Δt_c is compressive travel time in $\mu\ sec/ft$.

The drilling performance parameter used in this analysis is the mechanical special energy (MSE). The MSE is a measure of input energy to output footage drilled. The mechanical specific energy is calculated from drilling data as (Teale, 1965; Dupriest and Koederitz, 2005):

$$MSE = 0.14504 \times \left[\frac{40{,}000\ WOB}{\pi\ D_b^2} + \frac{480{,}000}{D_b^2}\ \frac{N \times\ T}{ROP}\right] \tag{119}$$

Where, D_b is the bit diameter in meters, N is rotational speed in revelation per minute and T is the resultant torque in KN.m. A high mechanical specific energy value indicates inefficient drilling with high-energy waste. The mechanical specific energy provides a relative estimate of the drilling efficiency, where the accuracy of this estimates increases when combined with UCS by using the adjusted mechanical specific energy (Hammoutene, 2012). The MSE was adjusted with a factor of 0.2 to reflect non-quantifiable energy losses in the drilling system. Laboratory studies has shown this value to be in the range of 0.3 to 0.4 (Hammoutene, 2012). However for field studies the value is often assumed to be 0.35 (Dupriest and William, 2005) In essence, the ratio of the

adjusted mechanical specific energy to the unconfined rock strength $\left(\frac{MSE_{adj}}{UCS}\right)$ was set so the value was around one for the zone with most efficient drilling achieved for this section.

An inverted rate of penetration model that takes into account all parameters affecting the rate of penetration such as WOB, RPM, rock strength, drilling fluid weight, and flow rate was used. The inverted ROP model introduced by Warren (1987) and modified by Hareland and Nygaard (2007a) is adopted, where the inverted ROP is written as:

$$ROP = w_f \left[f\ hyd\ \left(\frac{a\ S^{\,2-bs}\ D_b^2}{RPM\ WOB^{\,2-bs}} \right) \right]^{-1} \tag{120}$$

Where w_f is a function taking the bit wear into account, $f\ hyd$ hydraulic function addressing the drilling fluid properties and flow rate, a is a bit constant, S is the rock strength, and bs is an experimental constant.

The section was drilled with a BHA which consisted of a standard PDC bit with 6 blades, mud motor, and downhole vibration measurements in 4 location within the BHA as indicated with red boxes in Figure 5.1. Table 5.1 provides detailed specification of the input parameters used in the model.

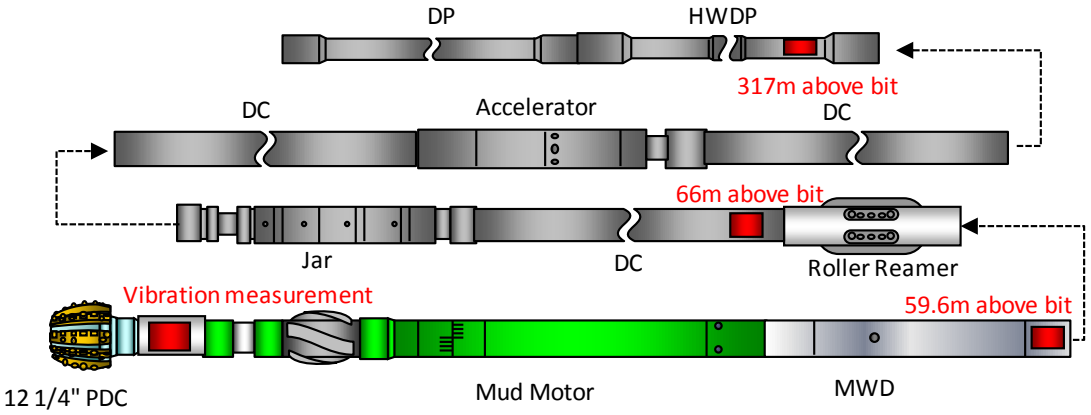

Figure 5.1. BHA Configurations of the 12 ¼" Section

Table 5.1. Model Input Parameters

Component	Length (m)	OD (m)	ID (m)
Drill pipe	-	0.127	0.109
Drill pipe element length	50	-	-
Drill collar	176	0.2032	0.07145
Drill collar element length	4	-	-
Heavy weight drill pipe	140	0.127	0.0762
Heavy weight drill pipe element length	10	-	-
Borehole	3360	0.3	-
Casing	1800	-	0.315
Stabilizers location from bit	20, 60	Fixed Boundary	
Properties			
ρ	7850	$Kg.m^{-3}$	
ρ_f	1650	$Kg.m^{-3}$	
C_f	0.0125	(-)	
Q_f	600	$gal.min^{-1}$	
E	2.1×10^{11}	Pa	
Drill bit nozzle sizes	5×18 4×14	1/32 inches	
υ	0.29	(-)	
Viscometer Readings			
3 RPM	6	°	
6 RPM	7	°	
100 RPM	20	°	
200 RPM	30	°	
300 RPM	40	°	
600 RPM	70	°	

5.3. RESULTS AND DISCUSSION

An exploratory well was drilled in the North Sea that consisting of five sections. Drilling the 12 ¼" section, a sudden decrease in ROP was observed after drilling the first 1000 m. After tripping out of the hole, the dull grading of the bit showed an average wear of 1 and a plugged nozzle. The 12 ¼" section was drilled with a PDC bit for an interval of 1500 m. The top interval (approximately from 800 m to 2900 m as indicated from sonic log in Figure 5.2) of the 12 ¼" section consisted of mostly claystone and light shales with

interbedded marls and sandstone, while the lower interval of the section consisted of mainly limestone and chalk. Figure 5.2 shows the operating parameters and ROP obtained for this section. The operational parameters shown in Figure 5.2 consists of WOB measured in tons, torque measured in KN.m, total RPM applied to the bit, sonic log, and measured ROP in m/hr.

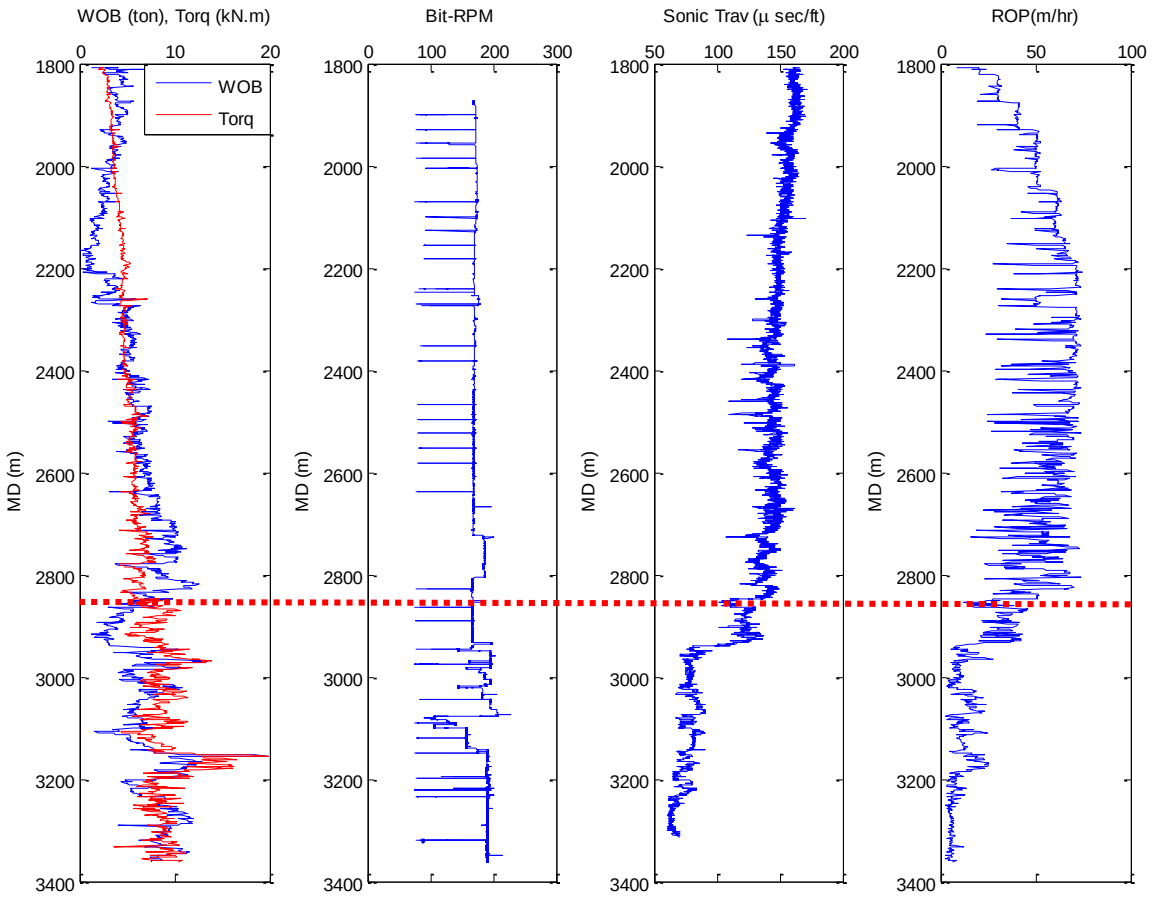

Figure 5.2. Operating Parameters, Sonic Log, and ROP for the 12 ¼" Section

The first 1000 m (above redline in Figure 5.2) was drilled with an average ROP of 50 m/hr, and then the ROP started decreasing.

Lateral vibration levels measured from the 4 positions within the BHA shows low to moderate levels for the first 1000 m, as indicated in Figure 5.3.

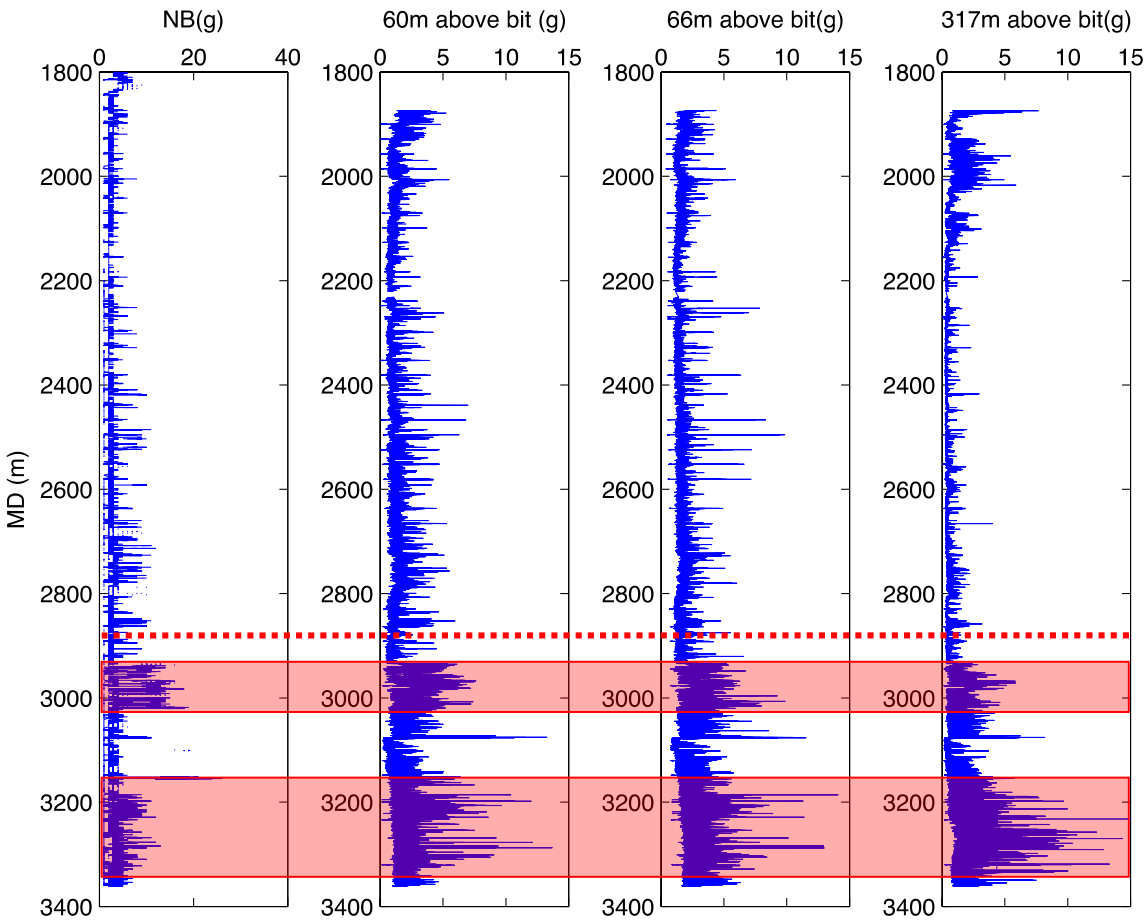

Figure 5.3. Measured Lateral Vibrations of the 12 ¼" Section

Lateral vibration beyond the first 1000 m started increasing specially near the bit. The first selected zone in Figure 5.3 shows an abnormal increase in lateral vibrations in zone 1, where the highest vibration was encountered near the bit and started decreasing as traveling up the drill stem. For zone 2 however, the maximum lateral vibrations, excluding near bit, where encountered at the top of the BHA (317m above the bit). It is believed that this behavior is connected to the torsional vibration.

The applied rotation at each sensor position and its corresponding measured downhole RPM can be seen in Figure 5.4.

Low stick-slip severity is noticed at the first 1000 m, where a good ROP in excess of 50 m/h was achieved, after the first 1000 m downhole RPM fluctuations started to

increase causing an increase in stick/slip severity (Figure 5.4). The highest stick/slip severity was encountered in zone 2, where at that interval the BHA was stalling.

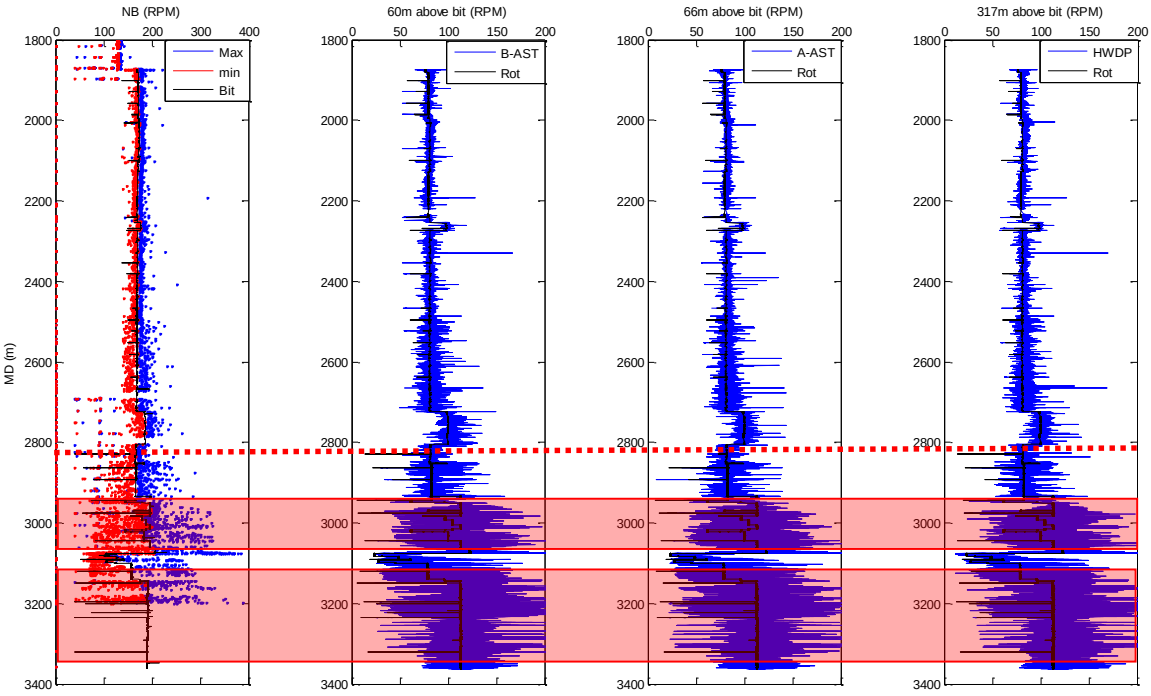

Figure 5.4. Applied and Measured Downhole RPM at 4 Position in the BHA

Using the measured well log data (sonic logs) the UCS was obtained and utilizing the operational parameters, the mechanical specific was calculated of the section. By relating the drilling performance parameter (MSE) to the environment/geological parameter (UCS), one can define the produced level of efficiency. Figure 5.5 shows the UCS, MSE and the ratio of the adjusted MSE to UCS for the drilled section.

The ratio of the adjusted MSE to UCS should stay around 1 when drilling efficiently (Figure 5.5). However, throughout the run one find this relationship to diverge greatly from this value, reaching levels of more than 6, indicating the drilling efficiency being around 15% of the optimal value. For most of the limestone section the MSE_{adj} to UCS ratio was found to be between 2 and 6, hence, the drilling efficiency was below 50% all throughout this critical section.

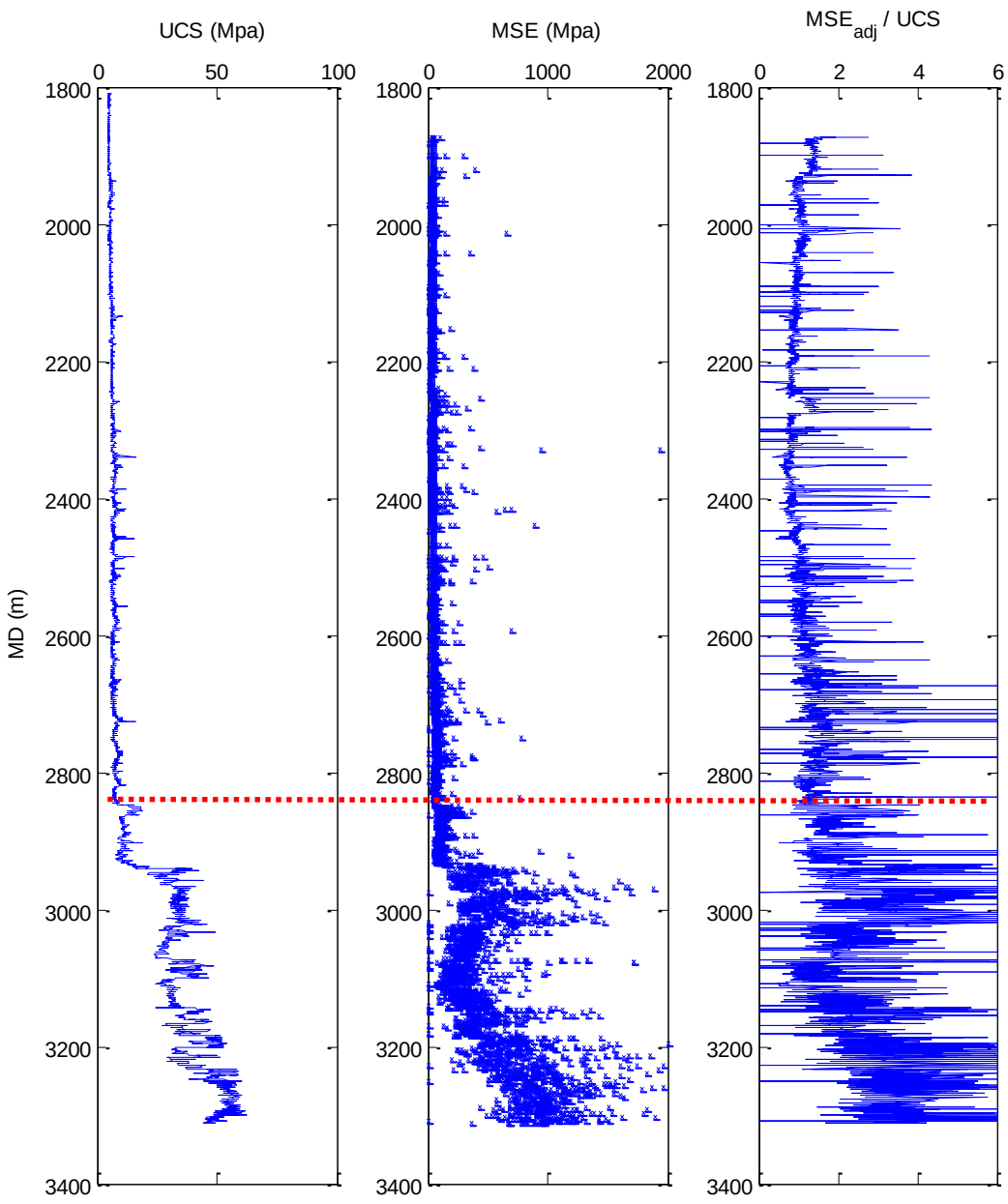

Figure 5.5. Optimum Drilling Efficiency Obtained from UCS and MSE

With the use of the vibration model presented above, the critical speed, using the applied WOB and RPM from the well logs, was calculated as a function of depth for axial, lateral, and torsional modes (Figure 5.6).

Figure 5.6 shows the calculated critical speeds for lateral, axial and torsional modes. Overall, the drill stem was operated away from critical speeds. A few zones was operated

at critical speeds as seen in Figure 5.6 as the applied RPM cross the critical speeds. The selected zones in Figure 5.6 show the locations where the drill stem was operated at those critical speeds. Those zones correspond well with the elevated drill stem vibrations measured below 2800 m.

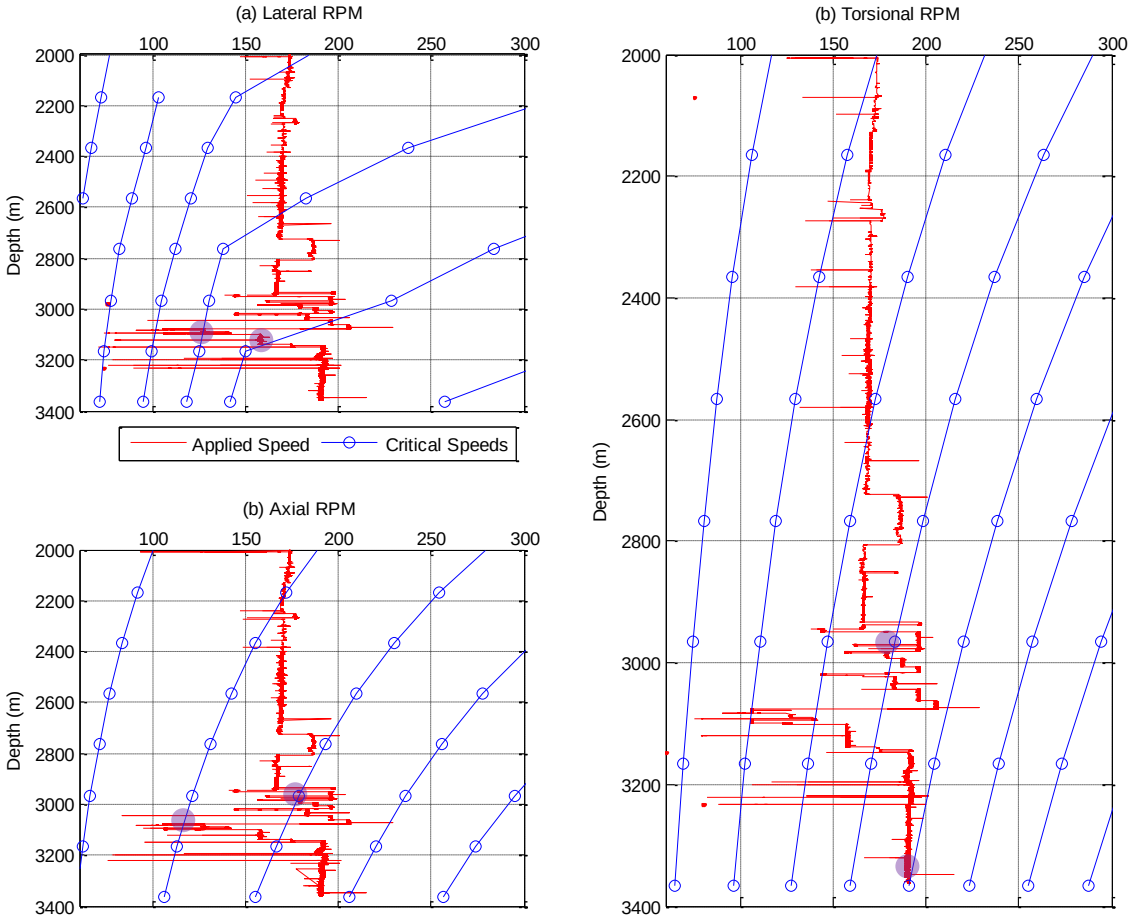

Figure 5.6. Critical Speeds and Applied Rotation as Function of Depth Based on WOB and RPM from Well Logs (a) Lateral (b) Axial (c) Torsional

The two selected zones with low rate of penetrations (Figure 5.3) are investigated with the use of the inverted ROP and vibration models to optimize the drilling within those two zones. Figure 5.7 shows RPM versus WOB with the predicted ROP and critical speeds for the three modes for the first zone located between 2900-3100 m, where the light blue

dashed lines represent the higher (secondary) lateral speeds, the solid red lines represent the axial critical speeds, and the dashed blue lines are torsional critical speeds.

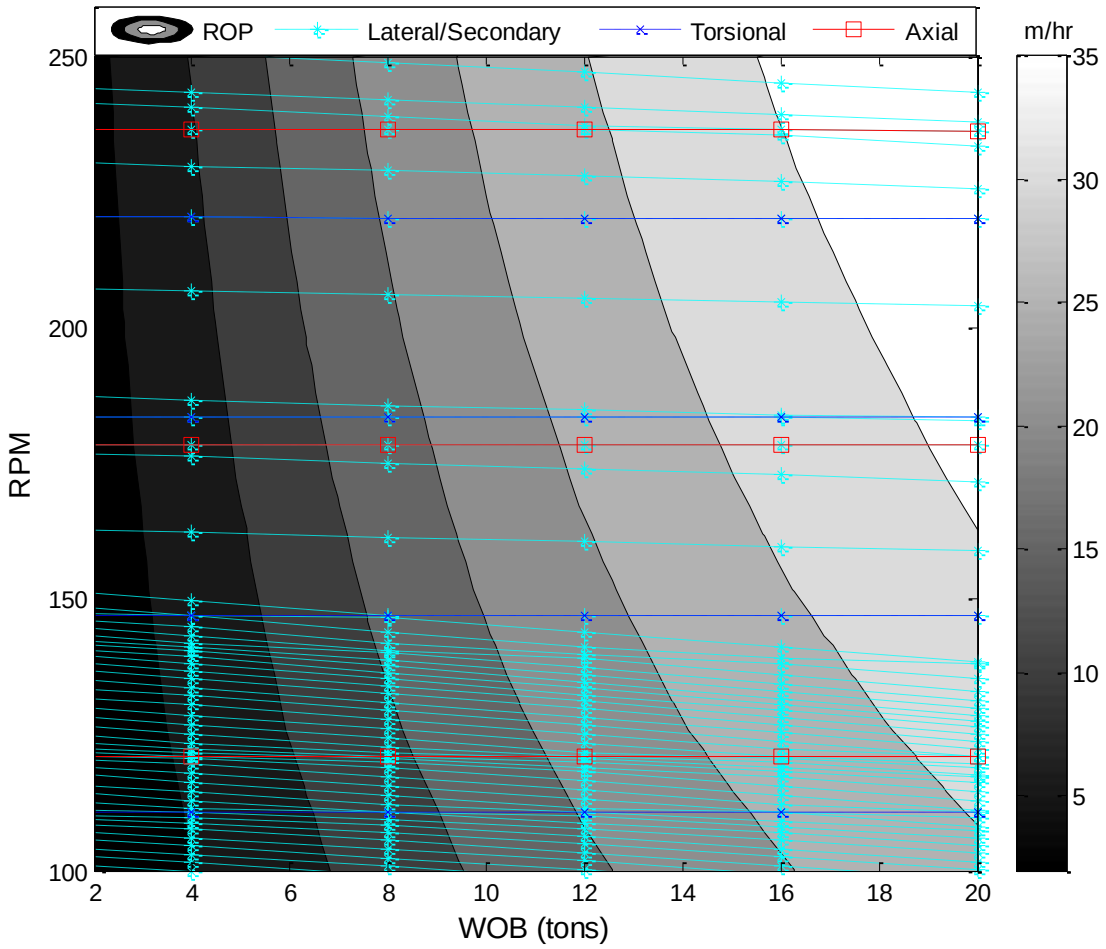

Figure 5.7. RPM Versus WOB with the Predicted ROP and Critical Speeds for the 1st Zone (2800-3100 m)

Due to the lateral vibrations are easily excited, concentrated numbers of lateral speeds are seen at low rotational speed. From Figure 5.7 the sweet spot of optimum drilling is located between 190 to 210 RPM and 6 to 18 tons. The average ROP of the first selected zone (2900-3100 m) is 8 m/hr with an average WOB and RPM of 7 tons and 160 RPM respectively. The optimum drilling window of this section shows an average ROP of 20 m/hr with 200 RPM and 10 tons WOB with avoiding harmful vibrations.

The procedure was repeated for the 2nd zone located between 3200-3360 m. Figure 5.8 shows the modeled operating window of the 2nd zone.

The sweet spot for optimum drilling efficiency for the 2nd zone is located between 172 to 198 RPM and 7 to 20 tons of WOB (Figure 5.8). For the second zone (3200-3360 m), the average ROP was 5 m/hr with an average WOB and RPM of 8 tons and 190 RPM respectively. Analysis of this section revealed an ROP of 15 m/hr could be achieved while avoiding vibrations when operating with WOB of 16 tons and 200 RPM.

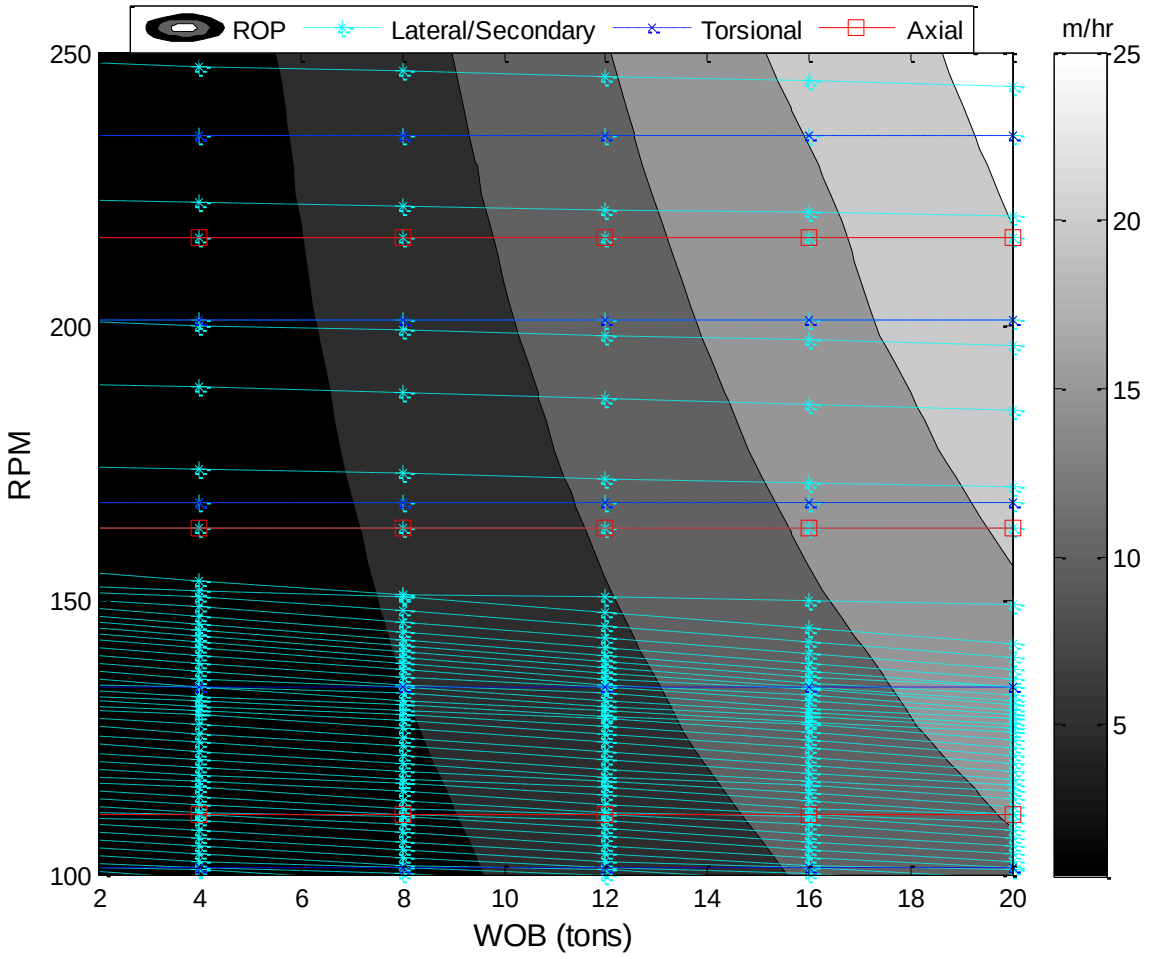

Figure 5.8. RPM Versus WOB with the Predicted ROP and Critical Speeds of the 2nd Zone (3200-3360 m)

5.4. SUMMARY

In this chapter, drill stem vibration analysis was introduced to enhance drilling performance by using drill stem vibration to the inverted ROP model. The drill stem vibration model correlates with the measured field data, as the applied rotational speed and weight on bit combination crosses the modeled critical speeds drill stem vibrations increases.

The proposed methodology of enhancing drilling performance by selecting a combination of weight on bit and applied RPM while avoiding harmful drill stem vibrations gives a guideline to increase the rate of penetration while maintaining low axial, torsional and lateral vibrations.

6. CONCLUSIONS AND FUTURE WORK

6.1. SUMMARY AND CONCLUSIONS

This dissertation discuss multiple parameters effect on drill stem vibrations, through modeling and field data verifications, and how to optimize drilling efficiency from a vibration point of view. A computational code built in Matlab® with the use of finite element formulation was created to be used for different drill stem configurations to increase drilling efficiency.

First, a parametric study was performed using two approaches, Euler-Bernoulli and Timoshenko beam theories, to select a model to be used in further investigations. The parametric study showed that torsional natural frequencies for the Euler-beam model are higher than the Timoshenko beam model by an average difference of 7.4% for the first ten modes. For the axial modes, no significant change was observed between the two models. The average difference of the lateral natural frequencies of the first ten modes using both models is 1.35% which translates to difference of 1 RPM. The maximum difference between the two models for all vibration modes at normal drilling conditions translates to 6 RPM when considering the first ten modes, thus at normal operating conditions the use of the nonlinear Euler-Bernoulli's assumptions can be justified.

The analysis showed that drill stem vibrations are sensitive to the change of the drill pipe length; axial, torsional, and lateral vibrations change behaviors at different drill pipe length. While increasing the length of drill collar increases both lateral and axial frequencies and decreases torsional frequencies. Increasing axial load reduces the lateral natural frequencies with a small effect on axial and torsional natural frequencies. The percentage difference in the first lateral natural frequency increases under higher axial load and shorter drill collar length. However, the percentage difference in the first torsional natural frequency does not change with the change of any parameter.

Bases on the previous conclusion, the Euler-Bernoulli beam model was modified to include two vibration mitigation tools incorporated in two wells and used to analyze vibration field data collected from three wells. The field data showed that torsional vibration increases at every sandy formation, causing lateral vibration and downhole RPM

fluctuations increases. Furthermore, as drill stem lateral vibration exceed 1.1 g, the rate of penetration decreased.

The drill stem vibration model was capable of predicting the behavior seen in the vibration measurements of the three wells. The model simulation and field data showed that axial and lateral vibrations are higher in the BHA compared to the drill pipe, while torsional vibrations are higher in the drill pipe compared the BHA.

Including drill stem vibration dampening tools reduces drill stem vibration and decreases stick-slip tendency, and based on the collected data and model simulations, the imbalance vibration sub had the lowest lateral vibrations. As it was observed from both the field data and the model, drill stem vibrations increase both with and without vibration dampening tools when operating at critical speeds.

Fluid structure interaction with the drill stem model had no effect on axial and torsional frequencies; however, it do affect lateral frequencies. At the conditions used in the parametric study, the maximum change in lateral frequencies was observed with the use of the Power Law fluid model.

The dynamic pressure using both Herschel Bulkley and Power Law fluid models have a significant impact on lateral frequencies. High flow rate causes the drill stem to be unstable. Also, the wellbore diameter and total flow area at the bit changes the lateral frequencies of the drill stem. Wrong selection of total flow area at the bit (nozzle sizes) could cause the drill stem to be unstable.

A methodology was presented to enhance drilling performance by combining inverted rate of penetration model with drill stem vibration model. The drill stem vibration model correlates with the measured field data, as the applied rotational speed and weight on bit combination crosses the modeled critical speeds drill stem vibrations increases. The proposed methodology of enhancing drilling performance by selecting a combination of weight on bit and applied RPM while avoiding harmful drill stem vibrations gives a guideline to increases the rate of penetration while maintaining low axial, torsional and lateral vibrations.

6.2. FUTURE WORK

The developed model is only applicable for vertical wells. As directional drilling is used more often lately, it would of an interest to modify the model to account for drill stem deviation.

The model presented in this thesis couples all three vibrational modes using non-linear finite strain relationships. The model was verified for each independent vibration mode but the three coupled vibrations were not verified simultaneously. It would therefore be valuable to perform an experimental validation of the model.

The available vibration measurements data is not uniformly sampled, thus a new technique to resample the vibration data is needed to extract information to directly compare drill stem dynamical data such as natural frequencies with the developed models.

The modeling and analysis of vibration dampening tools were addressed using a simplified approach and with limited data set, even though the field data and modeling effort gave similar results further development to of a more complex model of the tools and additional data would be beneficial for further verification of the results presented herein.

Another limitation of the developed model is the assumption made with the fluid model. The drilling fluid was assumed to be flowing axially with no rotation, however, the drilling fluid flows in swirling motions traveling down the drill stem. The developed fluid model is inconclusive, experimental studies is required to verify whether Herschel Bulkley or Power Law fluid models are more representative of the actual drill stem dynamics.

APPENDIX A
FINITE ELEMENT SHAPE FUNCTIONS

The shape functions used for Euler-Bernoulli's Model are:

$$\begin{aligned} N_u &= [1-\zeta \quad 0 \quad 0 \quad 0 \quad 0 \quad 0 \quad \zeta \quad 0 \quad 0 \quad 0 \quad 0 \quad 0] \\ N_{\theta_x} &= [0 \quad 0 \quad 0 \quad 0 \quad 0 \quad 1-\zeta \quad 0 \quad 0 \quad 0 \quad 0 \quad 0 \quad \zeta] \\ N_v &= [0 \quad N_{v1} \quad N_{v2} \quad 0 \quad 0 \quad 0 \quad 0 \quad N_{v3} \quad N_{v4} \quad 0 \quad 0 \quad 0] \\ N_w &= [0 \quad 0 \quad 0 \quad N_{v1} \quad N_{v2} \quad 0 \quad 0 \quad 0 \quad 0 \quad N_{v3} \quad N_{v4} \quad 0] \end{aligned} \tag{121}$$

Where:

$$\begin{aligned} N_{v1} &= 2\,\zeta^3 - 3\,\zeta^2 + 1, \quad & N_{v2} &= l_e\,\zeta \;\; 1-\zeta\;^2 \\ N_{v3} &= \zeta^2 \;\; 3-2\,\zeta\;, & N_{v4} &= l_e\,\zeta^2 \;\; \zeta - 1 \end{aligned} \tag{122}$$

Where ζ is dimensionless length ($\zeta = x/l_e$) and l_e is the element length.

The shape functions used for Timoshenko Model are:

$$\begin{aligned} N_u &= [1-\zeta \quad 0 \quad 0 \quad 0 \quad 0 \quad 0 \quad \zeta \quad 0 \quad 0 \quad 0 \quad 0 \quad 0] \\ N_{\theta_x} &= [0 \quad 0 \quad 0 \quad 0 \quad 0 \quad 1-\zeta \quad 0 \quad 0 \quad 0 \quad 0 \quad 0 \quad \zeta] \\ N_v &= [0 \quad N_{w1} \quad N_{w2} \quad 0 \quad 0 \quad 0 \quad 0 \quad N_{w3} \quad N_{w4} \quad 0 \quad 0 \quad 0] \\ N_w &= [0 \quad 0 \quad 0 \quad N_{w1} \quad N_{w2} \quad 0 \quad 0 \quad 0 \quad 0 \quad N_{w3} \quad N_{w4} \quad 0] \\ N_{\theta_y} &= [0 \quad 0 \quad 0 \quad N_{\theta_1} \quad N_{\theta_2} \quad 0 \quad 0 \quad 0 \quad 0 \quad N_{\theta_3} \quad N_{\theta_4} \quad 0] \\ N_{\theta_z} &= [0 \quad N_{\theta_1} \quad N_{\theta_2} \quad 0 \quad 0 \quad 0 \quad 0 \quad N_{\theta_3} \quad N_{\theta_4} \quad 0 \quad 0 \quad 0] \end{aligned} \tag{123}$$

Where:

$$\begin{aligned} N_{w1} &= \frac{l_e\,\left(\zeta^2-\zeta^3+1/2\;\phi\;(\zeta-\zeta^2)\right)}{1+\phi} & N_{w2} &= \tfrac{1}{2}\;\frac{l_e\,\zeta\;(-2+4\;\zeta-2\;\zeta^2+\phi\;\zeta-\phi)}{1+\phi} \\ N_{w3} &= \frac{3\;\zeta^2-2\;\zeta^3+\phi\;\zeta}{1+\phi} & N_{w4} &= -\tfrac{1}{2}\;\frac{l_e\,\zeta\;(-2\;\zeta+2\;\zeta^2-\phi+\phi\;\zeta)}{1+\phi} \\ N_{\theta_1} &= \frac{6\;\zeta-6\;\zeta^2}{1+\phi\;l_e} & N_{\theta_2} &= -\frac{-1+4\;\zeta-3\;\zeta^2-\phi+\phi\;\zeta}{1+\phi} \\ N_{\theta_3} &= 6\;\frac{\zeta\;-1+\zeta}{1+\phi\;l_e} & N_{\theta_4} &= \frac{\zeta\;-2+3\;\zeta+\phi}{1+\phi} \end{aligned} \tag{124}$$

$$\phi = \frac{12EI}{k_s\;GAl_e^{\;2}}$$

Where, E is the Young Modulus, I is the momonet of inertia, k_s is the shear constent, G is the shear Modulus and A is the cross sectional area.

APPENDIX B

ANALYTICAL DERIVATION OF THE UNCOUPLED AXIAL MODEL

The displacement field of uncoupled longitudinal rod is written as:

$$u = u(x,t), \qquad v = 0, \qquad w = 0 \tag{125}$$

Where, u is the axial displacement, v and w are the lateral displacements. The strain energy is defined as:

$$\epsilon_{xx} = E\frac{\partial u}{\partial x}, \qquad \epsilon_{yy} = \epsilon_{zz} = \epsilon_{xy} = \epsilon_{yz} = \epsilon_{zx} = 0 \tag{126}$$

Where, E is the Young Modulus and ϵ_{ij} is the strain. Thus, the total strain energy is:

$$U = \frac{1}{2}\int_0^L EA\left(\frac{\partial u\ x,t}{\partial x}\right)^2 dx \tag{127}$$

The kinetic energy is expressed as:

$$T = \frac{1}{2}\int_0^L \rho A\left(\frac{\partial u\ x,t}{\partial t}\right)^2 dx \tag{128}$$

Where ρ is the linear density per unit length. Using the generalized Hamilton's principle stating:

$$\delta\int_{t_1}^{t_2} U - T + W\ dt = 0 \tag{129}$$

Setting the virtual work (W) equal to zeros and subsisting Equation 127 and Equation 128 in Equation 129 and integrating by parts yields the equation of motion of the uncoupled axial motion as:

$$\rho A\left(\frac{\partial^2 u\ x,t}{\partial t^2}\right) = EA\frac{\partial^2 u\ x,t}{\partial x^2} \tag{130}$$

And the boundary conditions are:

$$EA\frac{\partial u\ x,t}{\partial x}\Big|_{x=0}^{x=L} = 0 \tag{131}$$

The solution of the equation of motion (Equation 130) is obtained by separating variables (separating the spatial term from the temporal term) as:

$$U\ x,t\ = U\ x\ T\ t \tag{132}$$

Substituting Equation 132 in Equation 130 yield:

$$U'' + \beta^2 U = 0 \tag{133}$$

Where:

$$\beta^2 = \frac{\omega^2}{c^2} \qquad\qquad c = \sqrt{\frac{E}{\rho}}$$

Where ω is the natural frequency. Equation 133 has a solution of the form of:

$$U\ x\ = A\ cos\ \beta x\ + B\ sin\ \beta x \tag{134}$$

A And B are constants obtained by applying the boundary conditions.

APPENDIX C

ANALYTICAL DERIVATION OF THE UNCOUPLED TORSIONAL MODEL

The displacement field of uncoupled torsional model of a shaft is written as:

$$u = 0, \qquad v = -z\ \theta\ x,t\ , \qquad w = y\ \theta\ x,t \tag{135}$$

Where, u is the axial displacement, v and w are the lateral displacements and θ is the torsional displacement. The strain in the shaft is defined as:

$$\begin{aligned} \epsilon_{xy} &= \frac{\partial u}{\partial y} + \frac{\partial v}{\partial x} = -z\frac{\partial \theta}{\partial x} \\ \epsilon_{xz} &= \frac{\partial u}{\partial z} + \frac{\partial w}{\partial x} = y\frac{\partial \theta}{\partial x} \\ \epsilon_{xx} &= \epsilon_{yy} = \epsilon_{zz} = \epsilon_{yz} = 0 \end{aligned} \tag{136}$$

The corresponding stress is:

$$\begin{aligned} \sigma_{xy} &= -G\ z\frac{\partial \theta}{\partial x} \\ \sigma_{xz} &= G\ y\frac{\partial \theta}{\partial x} \\ \sigma_{xx} &= \sigma_{yy} = \sigma_{zz} = \sigma_{yz} = 0 \end{aligned} \tag{137}$$

Where G is the shear modulus. The total strain energy is obtained with the use of Equation 136 and Equation 137:

$$\begin{aligned} S &= \frac{1}{2} \iiint_V \left[\sigma_{xx}\epsilon_{xx} + \sigma_{yy}\epsilon_{yy} + \sigma_{zz}\epsilon_{zz} + \sigma_{xy}\epsilon_{xy} + \sigma_{xz}\epsilon_{xz} + \sigma_{yz}\epsilon_{yz}\right] dV \\ S &= \frac{1}{2}\int_0^l G\ I_p \left(\frac{\partial^2 \theta}{\partial x^2}\right)^2 dx \end{aligned} \tag{138}$$

Where I_p is the polar moment of inertia. The kinetic energy is torsional shaft is:

$$T = \int_0^l \rho I_p \left(\frac{\partial^2 \theta}{\partial t^2}\right)^2 dx \tag{139}$$

Using the Hamilton's principle, the equation of motion and the essential boundary condition are:

$$\begin{gathered} \rho I_p \frac{\partial^2 \theta}{\partial t^2} = G\ I_p \frac{\partial^2 \theta}{\partial x^2} \\ G I_p \frac{\partial \theta}{\partial x}\Big|_0^l = 0 \end{gathered} \tag{140}$$

Setting $c = \sqrt{G/\rho}$, the equation of motion (Equation 140) is rewritten as:

$$c^2 \frac{\partial^2 \theta\ x,t}{\partial x^2} = \frac{\partial^2 \theta\ x,t}{\partial t^2} \tag{141}$$

Assuming a separable solution of the form of:

$$\theta\ x,t\ = \Theta\ x\ T\ t \tag{142}$$

Substituting Equation 142 in to the equation of motion (Equation 141) yields:

$$\frac{\partial^2 \Theta}{\partial x^2} + \beta^2 \Theta = 0 \tag{143}$$

Where $\beta^2 = \frac{\omega^2}{c^2}$

The solution the spatial domain of the equation of motion (Equation 143) is:

$$\Theta\ x\ = A\ cos\ \beta x\ + B\ sin\ \beta x \tag{144}$$

The constants A and B are obtained by applying the boundary conditions.

APPENDIX D
ANALYTICAL DERIVATION OF THE UNCOUPLED LATERAL MODEL

The stain energy of Euler-Bernoulli's beam theory can be written as:

$$S = \frac{1}{2} \int_0^l EI \left(\frac{\partial^2 w}{\partial x^2} \right) dx \tag{145}$$

The kinetic energy is defined as:

$$T = \frac{1}{2} \int_0^l \rho A \left(\frac{\partial w}{\partial t} \right)^2 dx \tag{146}$$

Applying Hamilton's principle yields the equation of motion for lateral motion and the essential boundary conditions:

$$\begin{gathered} \frac{\partial^2}{\partial x^2} \left(EI \frac{\partial^2 w}{\partial x^2} \right) + \rho A \frac{\partial^2 w}{\partial t^2} = 0 \\ EI \frac{\partial^2 w}{\partial x^2} \Big|_0^l = 0 \\ \frac{\partial}{\partial x} \left(EI \frac{\partial^2 w}{\partial x^2} \right) \Big|_0^l = 0 \end{gathered} \tag{147}$$

Simplifying the equation of motion by letting $c = \sqrt{EI/\rho A}$ and assuming constant rigidity yields:

$$c^2 \frac{\partial^4 w}{\partial x^4} + \frac{\partial^2 w}{\partial t^2} = 0 \tag{148}$$

After separating the spatial and temporal domains, the spatial equation of motion can be written as:

$$\frac{\partial^4 W}{\partial x^4} - \beta^4 W = 0 \tag{149}$$

Where $\beta^4 = \omega^2/c^2$

Equation 149 has a solution of the form of:

$$W\ x\ = C_1 sinh\ \beta x\ + C_2 cosh\ \beta x\ + C_3 sin\ \beta x\ + C_4 cos\ \beta x \tag{150}$$

Where C_1, C_2, C_3 and C_4 are constants obtained by applying the boundary conditions.

APPENDIX E
DRILLING AND VIBRATION DATA

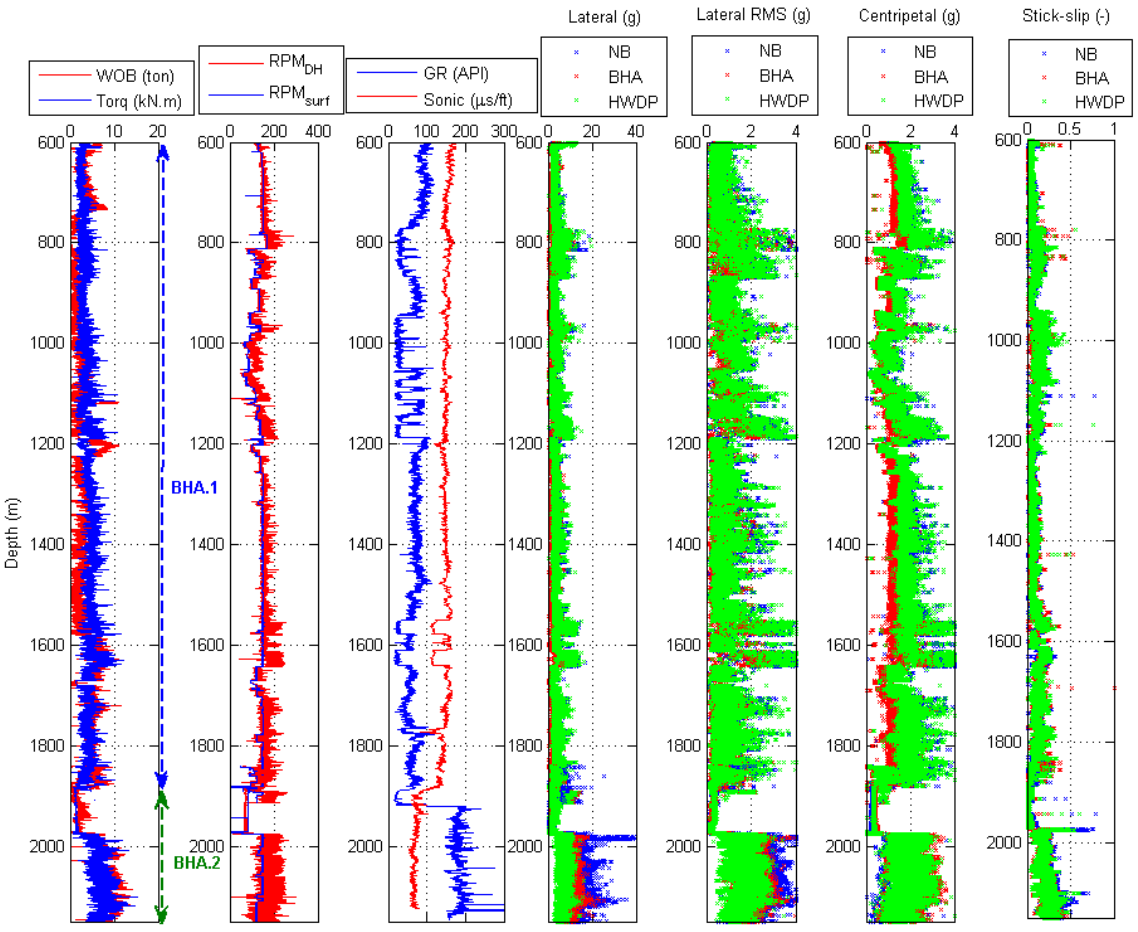

Figure E.1. Well A operating parameters and measured vibration data

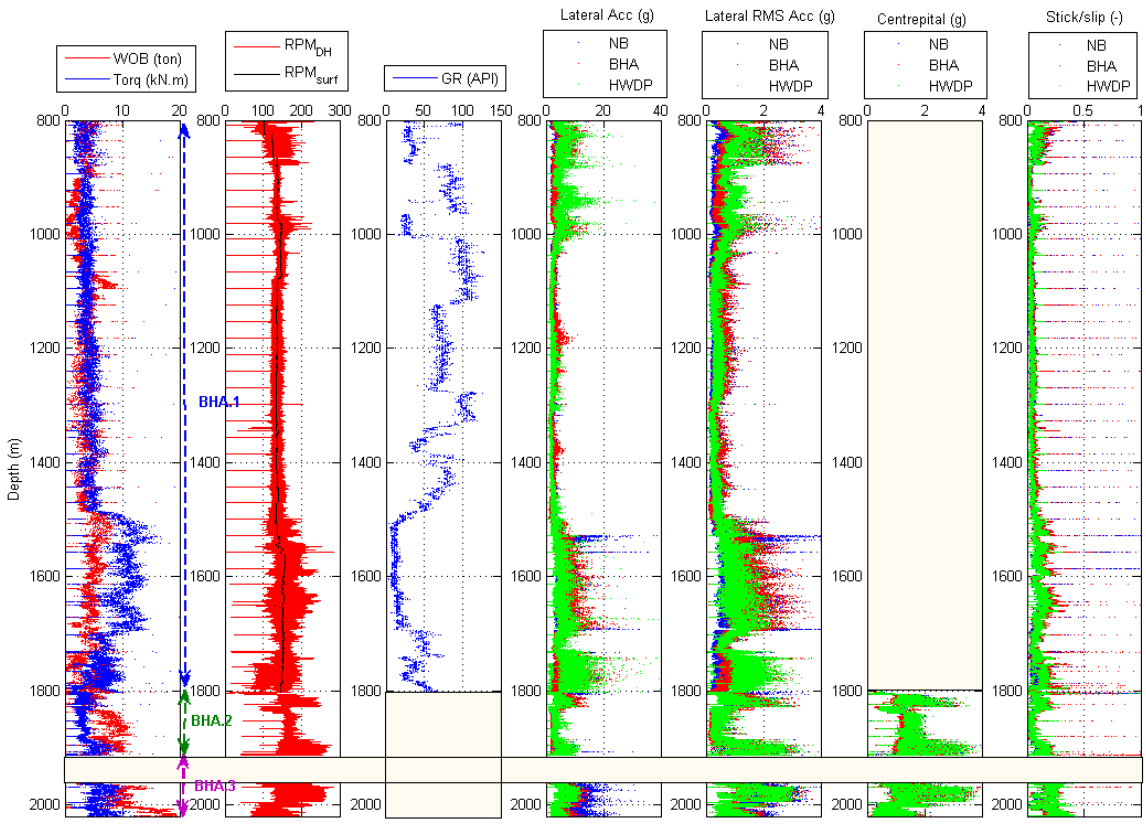

Figure E.2. Well B operating parameters and measured vibration data

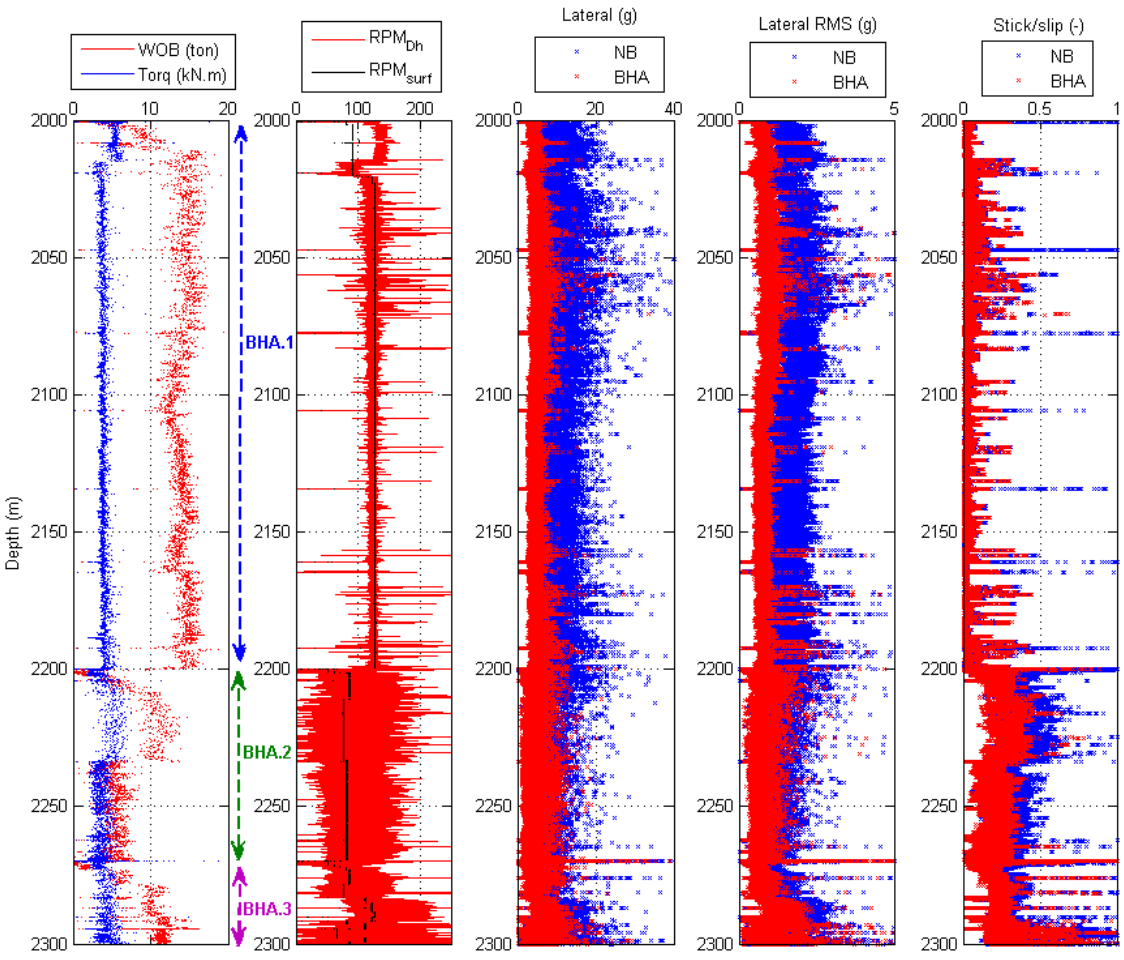

Figure E.3. Well C operating parameters and measured vibration data

APPENDIX F

COMPUTATIONAL SUMMARY OF THE DEVELOPED ALGORITHMS

The finite element formulation developed throughout the dissertation were coded into Matlab®, while the analytical formulation used in Chapter 2 were solved in MapleSoft™. Throughout the dissertations, the Matlab® algorithm included the effect of two vibration reduction subs, which was addressed in Chapter 3, and fluid models, developed in chapter 4 using both Euler-Bernoulli and Timoshenko beam theories. Figure F.1 shows a flow chart of the developed algorithm used in Matlab®.

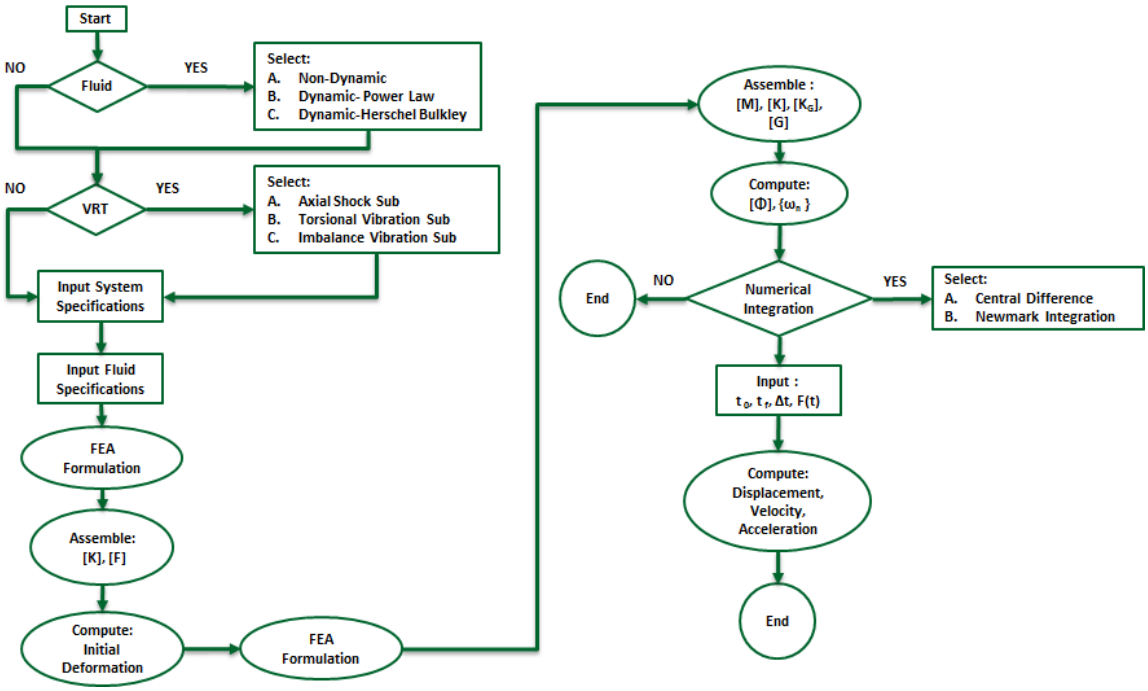

Figure F.1. Flow Chart of Matlab® Code Developed Throughout the Dissertation

Before entering the input parameters, a selection has to be made regarding how to treat fluid flow in the wellbore. The developed code have the ability to either exclude or include fluid forces using a non-dynamic fluid model, dynamic using Power Law Model, or dynamic using Herschel Bulkley model, where different input parameters are required for the each fluid model. Next step is to select if a vibration reduction tool is included in the BHA and the type and location of the tool. The option includes three different vibration reduction designs, named axial shock sub, torsional vibration sub, and imbalance vibration

sub. The FEA formulation step in Figure F.1 calculates each element stiffness, mass, fluid stiffness, fluid mass, gyroscopic matrices and element force vector than assemble them into global system matrix. In the initial deformation step, a static analysis is performance to obtain the initial deformation of the drill stem to be used to obtain the geometric stiffness matrix in the following step.

Samples of the developed Matlab® codes are listed below, where the samples codes includes the input parameter file, sub file of Power Law fluid model , and sub file of Herschel Bulkley fluid model.

Input File Script:

```
%------------------------- Input Data File --------------------------%
%--------------------------------------------------------------------%
%           Mohammed Al Dushaishi 2015   Missouri S&T                %
%--------------------------------------------------------------------%
%--------------------------------------------------------------------
-%
clear all; clc;
OPT1=0;  % 1=Delete ux, 2=Delete thetaX, Other: FUll matrix
OPT2=2;  % 0= No fluid, 1=Linear Fluid Model, 2=Dynamic using Power law,
         % 3=Dynamic using HB
OPT3=0;  % 0=No time simulation, 1= CD, 2=Range and Kutt
OPT4=0;  % 1= Make Movie of trajectory of motion
OPT5=0;  % 0= NO axial Shock sub, 1=Include axial shock sub,
         % 2=Include AST, 3=include vstab
OPT6=0;  % 0= No fluid rotation, 1=with Fluid rotation
OPT7=1;  % 0=Original Formulation, 1= Modified Formulation
OPT8=1;  % 0= Only pressure drop across the element, 1= include Ppump
%--------------------  System Specifications  -----------------------%

% Drill pipe information:
Ldp=1500;                               % Drill pipe length (m)
IDdp=0.1087;                           % Drill pipe inside diameter (m)
ODdp=0.127;                             % Drill pipe outside diameter (m)
rhodp=7850;                             % Drill pipe density (kg/m^3)
DPelL=50;                               % Drill pipe Element length(m)
%--------------------------------------------------------------------%
                No_BHA_Components=1;  % Number of BHA Components
%--------------------------------------------------------------------%
% BHA Component 1 "Below drill pipe":
Ldc1 =200;                              % BHA Component 1 length (m)
IDdc1=0.054;                          % BHA Component 1 inside diameter (m)
ODdc1=0.216;                         % BHA Component 1 outside diameter (m)
rho1=7850;                              % BHA Component 1 density (kg/m^3)
DCelL1=10;                              % BHA Component 1 Element length(m)
% BHA Component 2 "Below Component 1"
Ldc2 =10;                               % BHA Component 2 length (m)
```

```
IDdc2=0.07137;                          % BHA Component 2 inside diameter (m)
ODdc2=0.17145;                         % BHA Component 2 outside diameter (m)
rho2=3618;                                % BHA Component 2 density (kg/m^3)
DCelL2=2;                                % BHA Component 2 Element length(m)
% BHA Component 3 "Below Component 2"
Ldc3 =10;                                 % BHA Component 3 length (m)
IDdc3=0.06985;                          % BHA Component 3 inside diameter (m)
ODdc3=0.1651;                          % BHA Component 3 outside diameter (m)
rho3=7695;                                % BHA Component 3 density (kg/m^3)
DCelL3=2;                                % BHA Component 3 Element length(m)
% BHA Component 4 "Below Component 3"
Ldc4 =85;                                 % BHA Component 4 length (m)
IDdc4=0.07137;                          % BHA Component 4 inside diameter (m)
ODdc4=0.17145;                         % BHA Component 4 outside diameter (m)
rho4=7618;                                % BHA Component 4 density (kg/m^3)
DCelL4=5;                                % BHA Component 4 Element length(m)
% BHA Component 5 "Below Component 4"
Ldc5 =20;                                 % BHA Component 5 length (m)
IDdc5=0.07137;                          % BHA Component 5 inside diameter (m)
ODdc5=0.17145;                         % BHA Component 5 outside diameter (m)
rho5=7850;                                % BHA Component 5 density (kg/m^3)
DCelL5=4;                                % BHA Component 5 Element length(m)
% BHA Component 6 "Below Component 5"
Ldc6 =15;                                 % BHA Component 6 length (m)
IDdc6=0.07137;                          % BHA Component 6 inside diameter (m)
ODdc6=0.17145;                         % BHA Component 6 outside diameter (m)
rho6=8466;                                % BHA Component 6 density (kg/m^3)
DCelL6=3;                                % BHA Component 6 Element length(m)
% BHA Component 7 "Below Component 6"
Ldc7 =14;                                 % BHA Component 7 length (m)
IDdc7=0.12;                             % BHA Component 7 inside diameter (m)
ODdc7=0.17145;                         % BHA Component 7 outside diameter (m)
rho7=1500;                                % BHA Component 7 density (kg/m^3)
DCelL7=2;                                % BHA Component 7 Element length(m)
% BHA Component 8 "Below Component 7"
Ldc8 =3;                                  % BHA Component 8 length (m)
IDdc8=0.07137;                          % BHA Component 8 inside diameter (m)
ODdc8=0.17145;                         % BHA Component 8 outside diameter (m)
rho8=2931;                                % BHA Component 8 density (kg/m^3)
DCelL8=0.3;                              % BHA Component 8 Element length(m)
%%%%%%%%%%%%%%%%%%%%%%%%%%%%%%%%%%%%%%%%%%%%%%%%%%%%%%%%%%%%%%%%%%%%%%%%%%%%

E1=2.1*10^11;                             %  Elastic Modules (Pa)
WOB=-150*10^3;                          % Applied axial force (N) 14tons 165
Rot_speed=2*pi/60*100;                  % rad/sec
pos=0.29;                                 % Poisson's ration (-)
G1=E1/(2*(1+pos));                      % Shear Modules
ks=6/7;                                   % Shear constant (-)
g=9.81;                                   % Gravitational forces (m/s^2)
% location of stabilizers (boundaries location):
STB1= Ldp+150;                 % stabilizer location (Ref. surface) (m)
STB2= Ldp+150;                 % stabilizer location (Ref. surface) (m)
% Axial Shock sub Location and stiffness
```

```
Axial_sub_L=Ldp+100; % (m) from surface
ksub=4.205*10^6; % shock sub stiffness (N/m)
% AST Vibration reduction tool
AST_Loc=Ldp+100;% (m) from surface
kAST=4.205*10^6; % AST stiffness (N/rad)
% V-stab
V_stab_lo=Ldp+100; % location of V-stab (m)
Mun=1500; % amount of unbalance mass (Kg)
Vun=0.03; % distance from G n V-direction (m)
Wun=0.01; % distance from G n W-direction (m)
%----------------------- fluid input data----------------------------%
Db=0.3; % wellbore diameter (m)
IDCS=0.445;%0.313614;%0.322961; %Casing ID (m)
DCS=800; % casing shoe depth (m)

rhof1=1297.6; % fluid density (kg/m^3)
Cf=0.0125; % fluid viscous damping coefficient (-)
Ppump=0; % pump pressure

% Dynamic Pressure%%
Q=6.30901964*10^(-5)*600; %m^3/s
Turb=2100; % Reynolds number for laminar/turbulent flow determination (-
)
% dial readings (deg)
R3=8; R6=10; R100=32; R200=46; R300=58; R600=92;

% Nozel sizes
Nozz1 = 18/(32*39.37); % (m) Nozzle sizes
Nozz2 = 18/(32*39.37);  Nozz3 = 10/(32*39.37);     Nozz4 =0/(32*39.37);
Nozz5 = 0/(32*39.37);   Nozz6 = 0/(32*39.37);      Nozz7 = 0/(32*39.37);
Nozz8 = 0/(32*39.37);   Cd=0.95; %discharge coeff (-)

% Boundary conditions
%ue=[u1  v1  thetaZ1  w1  thetaY1  thetaX1   u2  v2   thetaZ2   w2   thetaY2
thetaX2]
bcdof1 =[1 2 3 4 5 6 STB1Dof-4 STB1Dof-2 sdof-4 sdof-2];
%----------------------------- END ---------------------------------%
```

Power Law Fluid Model Script:

```
function
[PDynamicIN,PDynamicOUT,Vin,Vout,Pf_in,Pf_out]=DynamicPressure(R600,R30
0,le,Q,Ai,IDsys,rhof,...
Ab,Ao,Hole,ODsys,Cd,At,lengthvector,g,Ldp,Ldc,DCelL,DPelL,OPT8)

%Dynamic Pressure Function is used to calculated the inside and outside
%
% pressure across the drill stem using the Power Law fluid Model        %


Turb=2100; %Reynolds number for laminar/turbulent flow determination(-)
```

```
%--------------------- Modified Fluid forces -------------------------%

n=3.32*log(R600/R300); % consistency index(-)
Kvi=5.11*R600/1022^n*1/0.01*1/10^3; % (pa.s^n)

%                        Pressure Inside the DS                         %
%-------------------------------------------------------------------------%
% Calculating pressure drop across the DS
for jj=1:1:length(le)
Vin(jj)=Q/Ai(jj); % fluid velocity at each segment (m/s)
muin(jj)=Kvi*(Vin(jj)/IDsys(jj))^(n-1)*(3*n+1/(4*n))^n; % eff. viscosity
(pa.s)
Rein(jj)=rhof(jj)*Vin(jj)*IDsys(jj)/muin(jj); % Reynolds (-)
if (Rein(jj)>Turb)            % If Turbulent Flow
    a=(log(n)+3.93)/50;     % constant to calculate friction (-)
    b=(1.75-log(n))/7;      % constant to calculate friction (-)
    Fricin(jj)=a/(Rein(jj)^b); %Friction factor

else if (Rein(jj)<Turb)       % If Laminar Flow
        Fricin(jj)=24/Rein(jj);
    end
end
     % Pressure drop across the DS (pa)
     DeltaPin(jj)=Fricin(jj)*Vin(jj)^2*rhof(jj)/IDsys(jj)*le(jj);
end

%                        Pressure in the Annulus                        %
%-------------------------------------------------------------------------%
% Calculating pressure drop across the DS
for jj=1:1:length(le)
Vout(jj)=Q/(Ab(jj)-Ao(jj)); % fluid velocity at each segment (m/s)
muout(jj)=Kvi*(Vout(jj)/(Hole(jj)-ODsys(jj)))^(n-1)*(3*n+1/(4*n))^n;   %
eff. viscosity (pa.s)
Reout(jj)=rhof(jj)*Vout(jj)*(Hole(jj)-ODsys(jj))/muout(jj);  %  Reynolds
(-)
if (Reout(jj)>Turb)            % If Turbulent Flow
    a=(log(n)+3.93)/50;     % constant to calculate friction (-)
    b=(1.75-log(n))/7;      % constant to calculate friction (-)
    Fricout(jj)=a/(Reout(jj)^b); %Friction factor

else if (Reout(jj)<Turb)       % If Laminar Flow
        Fricout(jj)=24/Reout(jj);
    end
end
     % Pressure drop across the DS (pa)
     DeltaPout(jj)=Fricout(jj)*Vout(jj)^2*rhof(jj)/(Hole(jj)-
ODsys(jj))*le(jj);
end
%-------------------------------------------------------------------------%

% Pressure drop across the nozzles
Pnozz=rhof(1)*Q^2/(2*Cd^2*At^2); % (pa)
```

```
% Pump pressure
PDyn=sum(DeltaPin+DeltaPout)+Pnozz; % (pa)

% Adding pump pressure to the system
DeltaPtot=[PDyn DeltaPin];

% Calculating the actual pressure drop at each element inside the DS
DPelin=zeros(1,length(le)+1);
DPelin(1)=PDyn;
for tt=1:length(le)
    DPelin(tt+1)=DPelin(tt)-DeltaPtot(tt+1);
end

% Calculating the actual pressure drop at each element in the annulus
DPelout=zeros(1,length(le)+1);
DPelout(length(le)+1)=DPelin(length(le)+1)-Pnozz;
for tt=length(le):-1:1
    DPelout(tt)=DPelout(tt+1)-DeltaPout(tt);
end

% The actual Hydrostatic Pressure (pa)
Phyd=rhof(1)*g*lengthvector(1:end);
% Total dynamic pressure inside and outside (pa)
PDynamicIN=Phyd+DPelin;
PDynamicOUT=Phyd+DPelout;

% Utube length representation
PDynamicU=[PDynamicIN PDynamicOUT(length(le+1):-1:1)];
DeltaPU=[DPelin DPelout(length(le):-1:1)];
Ulength=[lengthvector, Ldp+Ldc+DCelL:DCelL:Ldp+Ldc+Ldc,...
    Ldp+Ldc+Ldc+DPelL:DPelL:Ldp+Ldc+Ldc+Ldp];

if OPT8==0
Pf_in=DeltaPin;
Pf_out=DeltaPout;
else
    Pf_in=DPelin(2:end);
    Pf_out=DPelout(2:end);
End
%---------------------------- END ----------------------------------%
```

Herschel Bulkley Fluid Model Script:

```
function
[PDynamicIN,PDynamicOUT,Vin,Vout,Pf_in,Pf_out]=DynamicPressure_HB(IDsys
,...
    ODsys, Hole, le, Q, rhof, R3, R6, R100, R200, R300, R600, g,...
    Cd,At, lengthvector, Ldp, Ldc,DPelL,DCelL,OPT8)

% H-B fluid model for pressure drops
% Mohammed Al Dushaishi
%8/26/2015
```

```
%Convert from m to ft
ID=3.280839895*IDsys;
OD=3.280839895*ODsys;
Holef=3.280839895*Hole;
le_ft=3.280839895*le;
% convert flow rate from m^3/s to ft^3/s
Q_f=35.314667*Q; % Q in ft^3/s
rhof_f=0.062428*rhof; %rhof in lb/ft^3


%------------- obtain H-B fluid model parameters ---------------------%

R=[R3; R6; R100; R200; R300; R600]; % placing viscometer readying in
matrix
% converting viscometer readying to field units
Rf=1.067*R; % lbf/100ft^2
% converting viscometer speed from RPM to Hz
SR=1.703*[3; 6; 100; 200; 300; 600]; %1/sec=Hz
%The geometric mean of the shear rate:
M_SR=sqrt(min(SR)*max(SR)); %
%shear stress value the corresponding to the geometric mean shear rate
tau_s=interp1(SR,Rf,M_SR); %
%yield stress
tau0=(tau_s^2-max(Rf)*min(Rf))/(2*tau_s-min(Rf)-max(Rf));
%obtain n and k graphically
LHS=-tau0+Rf;
cf=polyfit(log10(SR),log10(LHS),1);
n=cf(1,1); % Flow Behavior index
kv=10^(cf(1,2)); % Consistence index
%-------------------------------------------------------------------------%
%                          Pressure Inside the DS                         %
%-------------------------------------------------------------------------%
% Calculating pressure drop across the DS
for jj=1:1:length(le_ft)
Vinf(jj)=Q_f/(pi/4*ID(jj)^2);% fluid velocity at each segment (m/s)
C_cin(jj)=1-
(1/(2*n+1))*tau0/(tau0+kv*((3*n+1)*Q_f/(n*pi*(ID(jj)/2)^3))^n);
N_Rein(jj)=2*(3*n+1)/n*...
    ((rhof_f(jj)*Vinf(jj)^(2-
n)*(ID(jj)/2)^n)/(tau0*(ID(jj)/(2*Vinf(jj)))^n...
    +kv*((3*n+1)/(n*C_cin(jj)))^n));
C1=((log10(n)+3.93)/50);
C2=((1.75-log10(n))/7);
N_Re_cin=((4*(3*n+1))/(n*C1))^(1/(1-C2));

if (N_Rein(jj)>N_Re_cin)           % If Turbulent Flow
    f1(jj)=C1*(C_cin(jj)*N_Rein(jj))^(-C2);
    Dp_DL(jj)=f1(jj)*Q_f^2*rhof_f(jj)/(1421.22*ID(jj)^5);

else if (N_Rein(jj)<N_Re_cin)      % If Laminar Flow
      Dp_DL(jj)=4*kv/(14400*ID(jj))*...
```

```
          (tau0/kv+(((3*n+1)/(n*C_cin(jj)))*(8*Q_f/(pi*ID(jj)^3)))^n);
%psi/ft
    end
end
     % Pressure drop across the DS (psi)
     DeltaPin_psi(jj)=Dp_DL(jj)*le_ft(jj);
end
DeltaPin=DeltaPin_psi*6894.744825; %convert to (pa)
%%%%%%%%%%%%%%%%%%%%%%%%%%%%%%%%%%%%%%%%%%%%%%%%%%%%%%%%%%%%%%%%%%%%%%%%%%%%
%                          Pressure in the Annulus                          %
%-----------------------------------------------------------------------%
% Calculating pressure drop across the DS
for jj=1:1:length(le_ft)
Voutf(jj)=Q_f/(pi/4*(Holef(jj)^2-OD(jj)^2));%  fluid  velocity  at  each
segment (ft/s)
C_cout(jj)=1-(1/(n+1))*...
    tau0/(tau0+kv*((2*n+1)*2*Q_f/(n*pi*(Holef(jj)/2-OD(jj)/2)*...
    (((Holef(jj)/2)^2-(OD(jj)/2)^2))))^n);
N_Reout(jj)=4*(2*n+1)/n*((rhof_f(jj)*Voutf(jj)^(2-n)*...
    ((Holef(jj)-OD(jj))/2)^n)/(tau0*((Holef(jj)-
OD(jj))/(2*Voutf(jj)))^n+...
    kv*(2*(2*n+1)/(n*C_cout(jj)))^n));
N_Re_cout=((8*(2*n+1))/(n*C1))^(1/(1-C2));

if (N_Reout(jj)>N_Re_cout)           % If Turbulent Flow
    f2(jj)=C1*(C_cout(jj)*N_Reout(jj))^(-C2);
    Dp_DLOut(jj)=f2(jj)*Q_f^2*rhof_f(jj)/...
        (1421.22*(Holef(jj)-OD(jj))*(Holef(jj)^2-OD(jj)^2)); %psi/ft

else if (N_Reout(jj)<N_Re_cout)      % If Laminar Flow
         Dp_DLOut(jj)=4*kv/(14400*(Holef(jj)-OD(jj)))*...
             (tau0/kv+((16*(2*n+1)/(n*C_cout(jj)*(Holef(jj)-
OD(jj))))*...
             (Q_f/(pi*(Holef(jj)^2-OD(jj)^2))))^n); %psi/ft
    end
end
     % Pressure drop across the DS (psi)
     DeltaPout_psi(jj)=Dp_DLOut(jj)*le_ft(jj);
end
 DeltaPout=DeltaPout_psi*6894.744825; %convert to (pa)
%-----------------------------------------------------------------------%
% Pressure drop across the nozzles
Pnozz=rhof(1)*Q^2/(2*Cd^2*At^2); % (pa)

% Pump pressure
PDyn=sum(DeltaPin+DeltaPout)+Pnozz; % (pa)

% Adding pump pressure to the system
DeltaPtot=[PDyn DeltaPin];

% Calculating the actual pressure drop at each element inside the DS
DPelin=zeros(1,length(le)+1);
DPelin(1)=PDyn;
```

```
for tt=1:length(le)
    DPelin(tt+1)=DPelin(tt)-DeltaPtot(tt+1);
end

% Calculating the actual pressure drop at each element in the annulus
DPelout=zeros(1,length(le)+1);
DPelout(length(le)+1)=DPelin(length(le)+1)-Pnozz;
for tt=length(le):-1:1
    DPelout(tt)=DPelout(tt+1)-DeltaPout(tt);
end

% The actual Hydrostatic Pressure (pa)
Phyd=rhof(1)*g*lengthvector(1:end);
% Total dynamic pressure inside and outside (pa)
PDynamicIN=Phyd+DPelin;
PDynamicOUT=Phyd+DPelout;

 % Utube length representation
PDynamicU=[PDynamicIN PDynamicOUT(length(le+1):-1:1)];
DeltaPU=[DPelin DPelout(length(le):-1:1)];
Ulength=[lengthvector, Ldp+Ldc+DCelL:DCelL:Ldp+Ldc+Ldc,...
    Ldp+Ldc+Ldc+DPelL:DPelL:Ldp+Ldc+Ldc+Ldp];

Vin=0.3048*Vinf;
Vout=0.3048*Voutf;


if OPT8==0
Pf_in=DeltaPin;
Pf_out=DeltaPout;
else
    Pf_in=DPelin(2:end);
    Pf_out=DPelout(2:end);
End
%----------------------------- END ----------------------------------%
```

A Sample of the analytical solution devolved in MapleSoft™ is listed below. The sample of the Maple algorithm solve for axial frequencies for a drill stem including drill pipe, drill collar, and one stabilizer.

Frequency and Mode shape of Two Spans Rod
Mohammed Al Dushaishi 10-24-2014

The objective is to obtain the Frequency and Mode shape of a Twos pan rod which is shown in Figure.1. Where separate coordinates are assumed for each span.

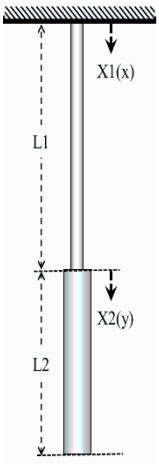

Figure Two spans beam

The Boundary Conditions are Fixed-Pinned-Pinned conditions and they are:

X1(0)=0 , X1(L1)= X2(0) , E1*A1*X1'(L1)=E2*A2*X2'(0) , E2*A2*X2'(L2)=0

```
> restart:
  with(plots):
  with(Student[Calculus1]):
  with(LinearAlgebra):
  interface(rtablesize=20):
  read "multiroot.mpl";
```

Geometric input

```
>  ID1:=0.095:
   OD1:=0.127:
   ID2:=0.0762:
   OD2:=0.22886:
   E:=2.1*10^11:
   rho:=7850:
>  AR1:=evalf(Pi/4*(OD1^2-ID1^2));
   AR2:= evalf(Pi/4*(OD2^2-ID2^2));
```

$$AR1 := 0.005579468554$$

$$AR2 := 0.03657635344 \quad (1)$$

Number of modes to include:

```
>            n:=10;
```

$$n := 10 \quad (2)$$

Length of each span:

```
>    L1:=1600; L2:=200;
```

$$L1 := 1600$$

$$L2 := 200 \quad (3)$$

The Normal Mode of the first span

```
> X1:= unapply(A1*sin(beta*x)+A2*cos(beta*x), x, A1, A2, beta);
```

$$X1 := (x, A1, A2, \beta) \rightarrow A1 \sin(\beta x) + A2 \cos(\beta x) \quad (4)$$

First derivative of the first span mode equation:

```
> dX1:=unapply(diff(X1(x, A1, A2, beta),x),x, A1, A2, beta);
```

$$dX1 := (x, A1, A2, \beta) \rightarrow A1 \cos(\beta x)\, \beta - A2 \sin(\beta x)\, \beta \quad (5)$$

The Normal Mode of the second span

```
> X2:= unapply(B1*sin(beta*y)+B2*cos(beta*y), y, B1, B2, beta);
```

$$X2 := (y, B1, B2, \beta) \rightarrow B1 \sin(\beta y) + B2 \cos(\beta y) \quad (6)$$

First derivative of the second span mode equation:

```
> dX2:= unapply(diff(X2(y, B1, B2, beta),y),y, B1, B2, beta);
```

$$dX2 := (y, B1, B2, \beta) \rightarrow B1 \cos(\beta y)\, \beta - B2 \sin(\beta y)\, \beta \quad (7)$$

Applying Boundary conditions:

```
> eqns:=simplify([X1(0,A1, A2, beta)=0, X1(L1,A1, A2, beta)=X2(0,B1,
  B2, beta), AR1*dX1(L1,A1, A2, beta)/beta=AR2*dX2(0, B1, B2,
  beta)/beta, X2(L2, B1, B2, beta)=0]);
```

$$eqns := [A2 = 0,\ A1 \sin(1600\,\beta) + A2 \cos(1600\,\beta) = B2,\ 0.005579468554\, A1 \cos(1600.\,\beta) - 0.005579468554\, A2 \sin(1600.\,\beta) = 0.03657635344\, B1,\ B1 \sin(200\,\beta) + B2 \cos(200\,\beta) = 0] \quad (8)$$

```
> SYS:=GenerateMatrix(eqns, [A1, A2, B1, B2])[1];
```

$$SYS := \begin{bmatrix} 0 & 1 & 0 & 0 \\ \sin(1600\,\beta) & \cos(1600\,\beta) & 0 & -1 \\ 0.005579468554 \cos(1600.\,\beta) & -0.005579468554 \sin(1600.\,\beta) & -0.03657635344 & 0 \\ 0 & 0 & \sin(200\,\beta) & \cos(200\,\beta) \end{bmatrix} \quad (9)$$

Characteristic equation to obtain the natural beta's:

```
> detSYS:= unapply((Determinant(SYS)), beta):
> plot(detSYS(beta),beta=0..20,view=[0..0.1, -0.03..0.03], color=blue,
  thickness=1, labels=[typeset(beta),"Characteristic Equation"],
  labeldirections = [horizontal, vertical], title = "Plot of the
  Characteristic Equation (Eigen function)", titlefont = [Times, bold,
  12], labelfont = [Times, italic, 12], numpoints=1000);
```

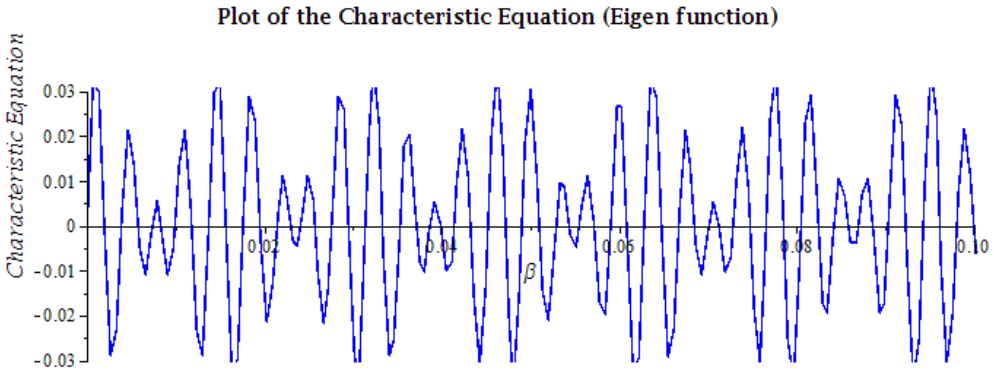

Finding the roots of the characteristic equation

```
>   omega:= mr(detSYS,0.00001, 1,3000,15,0);
```

Number of roots found: , 573

ω := [0.00192491280251173, 0.00383572420949006, 0.00569106729666368, 0.00727788245612060, 0.00843008081182836, 0.010016895971285
0.0118722390584589, 0.0137830504654372, 0.0157079632679490, 0.0176328760704607, 0.0195436874774390, 0.0213990305646126,
0.0229858457240696, 0.0241380440797773, 0.0257248592392343, 0.0275802023264079, 0.0294910137333862, 0.0314159265358979,
0.0333408393384097, 0.0352516507453880, 0.0371069938325616, 0.0386938089920185, 0.0398460073477263, 0.0414328225071832,
0.0432881655943568, 0.0451989770013352, 0.0471238898038469, 0.0490488026063586, 0.0509596140133370, 0.0528149571005106,
0.0544017722599675, 0.0555539706156753, 0.0571407857751322, 0.0589961288623058, 0.0609069402692841, 0.0628318530717959,
0.0647567658743076, 0.0666675772812859, 0.0685229203684595, 0.0701097355279165, 0.0712619338836242, 0.0728487490430812,
0.0747040921302548, 0.0766149035372331, 0.0785398163397448, 0.0804647291422566, 0.0823755405492349, 0.0842308836364085, ...
0.998031766692613, 0.999618581852070]

(10)

The First few roots

```
> lambda:=omega[1..n]:
```

Natural frequencies: (Hz)

```
> Frq:=evalf(seq(lambda[i]*sqrt(E/(rho))/(2*Pi),i=1..n));
```

Frq := 1.584550233, 3.157492475, 4.684774291, 5.991009214, 6.939476163, 8.245711087, 9.772992904, 11.34593515, 12.93048538, 14.51503561

(11)

Mode Shape

Applying Boundary conditions and setting A1=1 for normalization, than placing constants in matrix form:

```
> BCs:=simplify([A1=1, X1(L1,A1, A2, beta)=X2(0,B1, B2, beta),
  dX1(L1,A1, A2, beta)/beta*AR1=dX2(0, B1, B2, beta)/beta*AR2, X2(L2,
  B1, B2, beta)=0]):
  BCsM:=GenerateMatrix(BCs, [A1, A2, B1, B2]);
```

$$BCsM := \begin{bmatrix} 1 & 0 & 0 & 0 \\ \sin(1600\,\beta) & \cos(1600\,\beta) & 0 & -1 \\ 0.005579468554\cos(1600.\,\beta) & -0.005579468554\sin(1600.\,\beta) & -0.03657635344 & 0 \\ 0 & 0 & \sin(200\,\beta) & \cos(200\,\beta) \end{bmatrix}, \begin{bmatrix} 1 \\ 0 \\ 0 \\ 0 \end{bmatrix}$$

(12)

Solve for the constants A[i] and B[i] using linear solve:

```
> Const:=LinearSolve(BCsM);
```

$$Const := \begin{bmatrix} 1. \\ \dfrac{2.53612207\,10^{8}\sin(200.\,\beta)\cos(1600.\,\beta)+1.662561520\,10^{9}\sin(1600.\,\beta)\cos(200.\,\beta)}{-1.662561520\,10^{9}\cos(200.\,\beta)\cos(1600.\,\beta)+2.53612207\,10^{8}\sin(200.\,\beta)\sin(1600.\,\beta)} \\ -\dfrac{2.53612207\,10^{8}\cos(200.\,\beta)\left(\cos(1600.\,\beta)^{2}+\sin(1600.\,\beta)^{2}\right)}{-1.662561520\,10^{9}\cos(200.\,\beta)\cos(1600.\,\beta)+2.53612207\,10^{8}\sin(200.\,\beta)\sin(1600.\,\beta)} \\ \dfrac{2.53612207\,10^{8}\sin(200.\,\beta)\left(\cos(1600.\,\beta)^{2}+\sin(1600.\,\beta)^{2}\right)}{-1.662561520\,10^{9}\cos(200.\,\beta)\cos(1600.\,\beta)+2.53612207\,10^{8}\sin(200.\,\beta)\sin(1600.\,\beta)} \end{bmatrix} \quad (13)$$

Extract the constants values from Const matrix and set them as a function of the roots:

```
> AA1:=Const(1):
  AA2:=Const(2):
  BB1:=Const(3):
  BB2:=Const(4):
```

Re-writing the second span in term of one axis for plotting:

```
> X2N:=unapply(B1*sin(beta*(x-Li))+B2*cos(beta*(x-
  Li)),x,B1,B2,beta,Li);
```

$$X2N := (x, B1, B2, \beta, \mathrm{Li}) \rightarrow B1\sin(\beta\,(x-\mathrm{Li}))+B2\cos(\beta\,(x-\mathrm{Li})) \quad (14)$$

sub the constant's into the solution of the equation of motion for each span:

```
> X1f:=unapply(X1(x, AA1,AA2, beta),beta, x):
  X2f:=unapply(X2N(x, BB1,BB2,beta,L1),beta, x):
```

Using Piecewise function to plot Mode shape of the entire beam:

```
>       Mode1:=piecewise(x<=L1,X1f(lambda[1],x),
        x<=(L1+L2),X2f(lambda[1],x));
```

$$Mode1 := \begin{cases} 1.\sin(0.00192491280251173\,x)-9.845764863\,10^{-10}\cos(0.00192491 \\ -0.1522524833\sin(0.00192491280251173\,x-3.079860485)+0.06169296827\cos(0.001 \end{cases} \quad (15)$$

```
>       Mode2:= piecewise(x<=L1, X1f(lambda[2],x),
        x<=(L1+L2),X2f(lambda[2],x));
```

$$Mode2 := \begin{cases} 1.\sin(0.00383572420949006\,x)+1.239930206\,10^{-9}\cos(0.00383572420949006\,x) \\ 0.1509195435\sin(0.00383572420949006\,x-6.137158734)-0.1455081524\cos(0.00383572420949006\,x-6.1 \end{cases} \quad (16)$$

```
>       Mode3:= piecewise(x<=L1, X1f(lambda[3],x),
        x<=(L1+L2),X2f(lambda[3],x));
```

$$Mode3 := \begin{cases} 1.\sin(0.00569106729666368\,x)-1.362356499\,10^{-10}\cos(0.00569106729666368\,x) \\ -0.1448438166\sin(0.00569106729666368\,x-9.105707675)+0.3136839072\cos(0.00569106729666368\,x-9.105707675) \end{cases} \quad (17)$$

```
>       Mode4:= piecewise(x<=L1, X1f(lambda[4],x),
        x<=(L1+L2),X2f(lambda[4],x));
```

$$Mode4 := \begin{cases} 1.\sin(0.00727788245612060\,x) + 9.486728189\,10^{-10}\cos(0.00727788245612060\,x) & x \le 1600 \\ 0.09220007239\sin(0.00727788245612060\,x - 11.64461193) - 0.7966658349\cos(0.00727788245612060\,x - 11.64461193) & x \le 1800 \end{cases} \quad (18)$$

```
> plot([Mode1,Mode2,Mode3],x=0..L1+L2,color=[red,blue,black],thickn
ess=2, labels=[x (m),"Mode shape"], labeldirections =
[horizontal, vertical], title = "Mode shape", titlefont = [Times,
bold, 12], labelfont = [Times, italic, 12],legend=["Mode 1","Mode
2","Mode 3"],axis=[gridlines=10]);
```

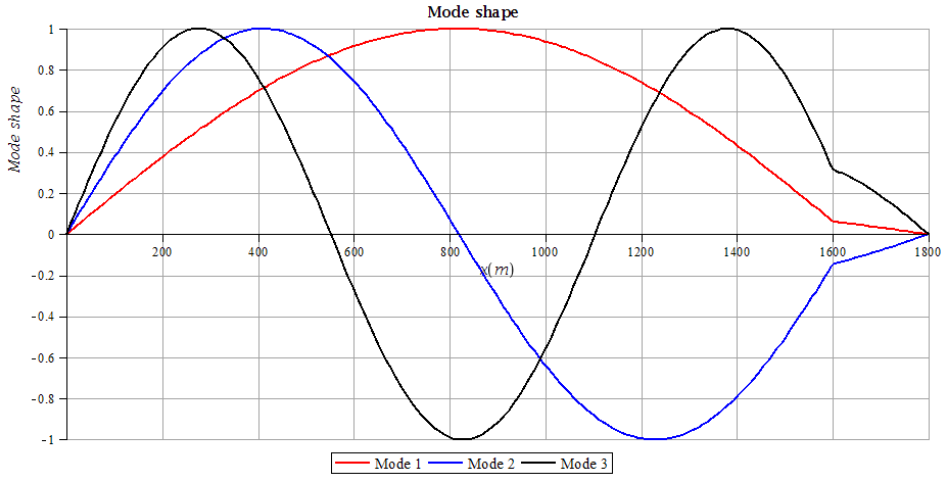

BIBLIOGRAPHY

Ahmadian, H., Nazari, S., and Jalali, H. 2007. Drillstring vibration modeling including coupling effects. International Journal of Industrial Engineering and Production Research, 18(4), 59-66.

Ahmed, R, and Miska, S. 2008. Experimental Study and Modeling of Yield Power-Law Fluid Flow in Annuli with Drillpipe Rotation. ADC/SPE Drilling Conference, 4-6 March, Orlando, Florida, USA: SPE-112604-MS.

Arevalo, Y., and Fernandes, F. 2012. Quantification of Drillstring Integrity Failure Risk Using Real-Time Vibration Measurements. Presented at SPE Asia Pacific Oil and Gas Conference and Exhibition, 20-22 September, Jakarta, Indonesia: SPE-147747.

Aslaksen, H., Annand, M., Duncan, R., Fjaere, A., Paex, L., and Tran, U. 2006. Integrated FEA Modeling Offers System Approach to Drillstring Optimization. Presented at IADC/SPE Drilling Conference, 21-23 February, Miami, Florida. SPE-99018.

Bailey, J. J., and Finnite, I. 1960. Analytical study of drill-string vibration. Journal of Engineering for Industry, 82(2), 122-128.

Bourgoyne, A. T., Chenevert, M. E., Millheim, K. K., and Young, F. S. 2003. Applied Drilling Engineering. SPE Textbook Series. Richardson, Tx, USA.

Bouziane, C., Bates, P., May, N., Nicholl, D., Burnett, T., Minardi, A., and Angeletii, P. 2012. Harmonic Vibration Disruption Improves Drilling Performance in Challenging Applications. Presented at SPE Asia Pacific Oil and Gas Conference and Exhibition, 22-24 October, Perth, Australia: SPE-159242.

Budley, B. 2015. Bp. Retrieved September 22, 2015, from http://www.bp.com/content/dam/bp/pdf/Energy-economics/statistical-review-2015/bp-statistical-review-of-world-energy-2015-full-report.pdf

Burgess, T., McDaniel, G., and Das, P. 1987. Improving BHA Tool Reliability with Drillstring Vibration Models: Field Experience and Limitations. Presented at SPE/IADC Drilling Conference, 15-18 March, New Orleans, Louisiana: SPE-16109.

Chen, S., and Geradin, M. 1994. An improve transfer matrix technique as applied to BHA lateral vibration analysis. Journal of Sound and Vibration, 185(1), 93–106.

Christoforou, A. P., and Yigit, A. S. 1997. Dynamic modeling of rotating drillstrings with borehole interactions. Journal of Sound and Vibration, 206(2), 243–260.

Cobern, M., Perry, C., Barbely, J., Burgess, D., & Wassell, M. (2007). Drilling tests of an active vibration damper. SPE/IADC Drilling Conference 20-22 February, Amsterdam, Netherlands: SPE-105400-MS.

Dunayevsky, V., Abbassian, F., and Judzis, A. 1993. Dynamic stability of drillstrings under fluctuating weight on bit. SPE Drilling and Completion, 8(2), 84-92.

Dupriest, F. E., and Koederitz, W. L. 2005. Maximizing Drill Rates with Real-Time Surveillance of Mechanical Specific Energy. SPE/IADC Drilling Conference, 23-25 February, Amsterdam, Netherlands: SPE-92194-MS.

Fann Instrument, c. 2015. Model 35 Viscometer Instruction Manual. Houston TX.

Gaines, A., Morrison, R., and Herrington, D. 2013. Step change drilling technology modifies drill string dynamics and results in reduced drilling vibrations. Presented at SPE Annual Technical Conference and Exhibition, 30 September-2 October, New Orleans, Louisiana: SPE-166445-MS.

Ghasemloonia, A., Rideout, D., and Butt, S. 2012. Coupled transverse vibration modeling of drillstring subjected to torque and spatially varying axial load. Journal of Mechanical Engineering Science, 227(5), 946-960.

Ghasemloonia, A., Rideout, D., and Butt, S. 2013. Vibration analysis of a drillstring in vibration-assisted rotary drilling: Finite element modeling with analytical validation. Journal of Energy Resources Technology, 135(3), 032902-032902.

Ghasemloonia, A., Rideout, D., Butt, S., and Hajnayeb, A. 2014. Elastodynamic and finite element vibration analysis of a drillstring with a downhole vibration generator tool and a shock sub. Proceedings of the Institution of Mechanical Engineers, Part C: Journal of Mechanical Engineering Science, 229(8), 1361-1384.

Hammoutene, C. 2012. FEA Modeled MSE/UCS Values Optimize PDC Design for Entire Hole Section. North Africa Technical Conference and Exhibition, 20-22 February, Cairo, Egypt: SPE-149372-MS.

Hareland, G., and Nygaard, R. 2007a. Calculating unconfined rock strength from drilling data. 1st Canada-U.S. Rock Mechanics Symposium, May 27-31, Vancouver, British Columbia, Canada: ARMA-07-214.

Hareland, G., and Nygaard, R. 2007b. Applications of rock strength in drilling evaluation. SPE Latin American and Caribbean Petroleum Engineering Conference, April 15-18, Buenos Aires, Argentina: Society of Petroleum Engineers.

Heisig, G., and Neubert, M. 2000. Lateral drillstring vibrations in extended-reach wells. Presented at IADC/SPE Drilling Conference 23-25 February, New Orleans, Louisiana: SPE-59235-MS.

Hutchinson, M., Burgess, D., Thompson, F., and Kopfstein, A. 2013. Self-Adapting Bottom Hole Assembly Vibration Suppression. Presented at SPE Annual Technical Conference and Exhibition, 30 September-2 October, New Orleans, Louisiana: SPE-166071.

Jafari, A. A., Kazemi, R., and Mahyari, M. F. 2012. The Effect of Drilling Mud and Weight Bit on Stability and Vibration of a Drill String. Journal of Vibration and Acoustics, 134(1), 11-14.

Jansen, J. D. 1991. Non-linear rotor dynamics as applied to oilwell drillstring vibrations. Journal of Sound and Vibration, 147(1), 115-135.

Kelessidis, V.C., Maglione, R., Tsamantaki, C., and Aspirtakis, Y. 2006. Optimal determination of rheological parameters for Herschel–Bulkley drilling fluids and impact on pressure drop, velocity profiles and penetration rates during drilling. Journal of Petroleum Science and Engineering, 53(3–4), 203-224.

Kwon, Y., and Bang, H. 2000. The finite element method using Matlab (2nd ED). Florida: CRC Press.

Leine, R., van Campen, D., and Keultjes, W. 2002. Stick-slip whirl interaction in drillstring dynamics. Journal of Vibration and Acoustic, 124(2), 287-296.

Liao, C., Balachandran, B., Karkoub, M., and Abdel-Magid, Y. 2011. Drill-string dynamics: Reduced-order models and experimental studies. Journal of Sound and Vibration, 133(4), 041008.

Majkut, L. 2009. Free and forced vibrations of timoshenko beams described by single difference equation. Journal of Theoretical and applied mechanics, 47(1), 193-210.

McCarthy, J., Forster, I., Burnett, T., and Kabbara, A. 2011. Careful Planning and Application of an Asymmetric Vibration Damping Tool Dramatically Improves Underrating While Drilling Performance in Deepwater Drilling. Presented at Offshore Technology Conference, 4-6 October, Rio de Janeiro, Brazil: OTC-22439.

Melakhessou, H., Berlioz, A., and Ferraris, G. 2003. A Nonlinear Well- Drillstring Interaction Model. Journal of vibration and acoustics, 125(1), 46-52.

Merlo, M., Maglione, R., and Piatti, C. 1995. An Innovative Model For Drilling Fluid Hydraulics. Presented at SPE Asia Pacific Oil and Gas Conference, 20-22 March, Kuala Lumpur, Malaysia: SPE-29259-MS.

Minitab 17 Statistical Software. 2010. [Computer software]. State College, PA: Minitab, Inc. (www.minitab.com)

Mitchell, R., and Miska, S. 2011. Fundamentals of Drilling Engineering. SPE Textbook Series VOL 12. Richardson, Tx, USA.

Modarres-Sadeghi, Y., Paidoussis, M. P., and Semler, C. 2006. A nonlinear model for an extensible slender flexible cylinder subjected to axial flow. Journal of Fluids and structures, 21(5-7), 609-627.

National Oilwell Varco 2011b. V-Stab® Vibration Damping Tool. http://www.nov.com/Downhole/Advanced_Drilling_Solutions/V-Stab.aspx accessed 23 December 2011.

Navarro-Lopez, E., and Cortes, D. 2007. Avoiding harmful oscillations in a drillstring through dynamical analysis. Journal of Sound and Vibration, 307(1-2), 152–171.

Nygaard, R., Hareland, G., Budiningsih, Y., Terjesen, H. E., and Stene, F. 2002. Eight Years Experience with a Drilling Optimization Simulator in the North Sea. Presented at SPE/IADC Asian Conference, Jakarta, Indonesia, 9-11 September: SPE-77247.

Ochoa, M. V. 2006. Analysis of drilling fluid rheology and tool joint effect to reduce errors in hydraulics calculations. PhD thesis, Texas A&M University.

Paidoussis, M. P. 1975. Stability of flexible slender cylinders in pulsatile axial flow. Journal of Sound and Vibration, 42(1), 1-11.

Paidoussis, M. P., and Besancon, P. 1981. Dynamics of arrays of cylinders with internal and external axial flow. Journal of Sound and Vibration, 76(3), 361-379.

Paidoussis, M. P., Luu, T. P., and Prabhakar, S. 2008. Dynamics of a long tubular cantilever conveying fluid downwards, which then flows upwards around the cantilever as a confined annular flow. Journal of Fluids and Structures, 24(1), 111-128.

Payne, M. 1992. Drilling bottom-hole assembly dynamics. PhD Thesis, Rice University.

Piovan, M., and Sampaio, R. 2006. Nonlinear model for coupled vibrations of drill-strings. Mecanica Computacional, XXV, 1751-1765.

Rao, S. 2004. Mechanical Vibrations, 5th Ed. Person Education Inc, Upper Saddle River, NJ.

Rashidi, B., Hareland, G. and Nygaard. R. 2008. Real-Time Bit Wear Prediction by Combining Rock Energy and Drilling Strength Concepts. Presented at International Petroleum Exhibition and Conference, Abu Dhabi, UAE, 3-6 November: SPE-117109.

Richard, T., Germay, C., and Detournay, E. 2007. A simplified model to explore the root cause of stick-slip vibrations in drilling systems with drag bits. Journal of Sound and Vibration, 305(3), 432–456.

Rinaldi, S., and Paidoussis, M. P. 2012. Theory and experiments on the dynamics of a free-clamped cylinder in confined axial air-flow. Journal of Fluids and Structures, 28, 167–179.

Ritto, T. G., Sampaio, R., and Soize, C. 2009a. Drill-string nonlinear dynamics accounting for the drilling fluid. Brazil: ABCM. 30º CILAMCE-Iberian-Latin-American Congress on Computational Methods in Engineering.

Ritto, T., Soize, C., and Sampaio, R. 2009b. Nonlinear dynamics of a drill-string with uncertain model of the bit-rock interaction. International Journal of Non-Linear Mechanics, 44(8), 865-876.

Sahebkar, S., Ghazavi, M., Khadem, S., and Ghayesh, M. 2011. Nonlinear vibration analysis of an axially moving drillstring system with time dependent axial load and axial velocity in inclined well. Mechanism and Machine Theory, 46(5), 743-760.

Salnes, K., Clemmensen, C., and Reimers, N. 2009. Drilling difficult formations efficiently with the use of an antistall tool. SPE Drilling & Completion, 24(4), 531-536.

Schen, A., Snell, A., and Stanes, B. 2005. Optimization of Bit Drilling Performance Using a New Small Vibration Logging Tool. Presented at SPE/IADC Drilling Conference, 23-25 February, Amsterdam, Netherlands: SPE-92336.

Spanos, P., Chevallier, A., and Politis, N. 2002. Nonlinear stochastic drill-string vibrations. Journal of Vibration and Acoustics, 124(4), 512-518.

Teale, R. 1965. The Concept of Specific Energy in Rock Drilling. International Journal of Rock Mechanics and Mining Science, 2(1), 711-725.

Tomax. Anti-Stall Technology. 2010. http://www.tomax.no accessed 23 December 2011.

Trindade, M., Wolter, S., and Sampaio, R. 2005. Karhunen-loève decomposition of coupled axial/bending vibrations of beams subject to impacts. Journal of Sound and Vibration, 279(35), 1015–1036.

Versan, M., and Tolga, A. 2005. Effect of Polymers on the Rheological properties of KCl/Polymer Type Drilling Fluid. Energy Sources, 27(5), 405-415.

Warren, T. M, and Oster, J. H. 1998. Shock Sub Performance Tests. Presented at IADC/SPE Drilling Conference, 3-6 March, Dallas, Texas: SPE-39323-MS.

Warren, T. M. 1984. Penetration Rate Performance of Roller Cone Bits. Presented at the 59th Annual Technical Conference and Exhibition, Houston, Texas. 16-19 September: SPE-13259.

Warren, T. M. 1987. Penetration–rate performance of roller cone bits. SPE Drilling Engineering, 2(1), 9-18.

Yigit, A., and Christoforou, A. 1998. Coupled torsional and bending vibration of drillstrings subject to impact with friction. Journal of Sound and Vibration, 215(1), 167–181.

VITA

Mohammed Fayez Al Dushaishi was born on October 24th, 1987 in Saudi Arabia. He went to high school in Saudi Arabia and finished high school in 2005. He received his Mechanical Engineering Bachelor's degree from Missouri University of Science and Technology in 2010. In August 2010, he started his master degree in Petroleum Engineering at Missouri University of Science and Technology. He earned his Master degree in Petroleum Engineering on the 28th of March of 2012. In December 2015, he received his PhD degree in Petroleum Engineering.